FIREBall, CHaS, and the diffuse universe

Erika Tobiason Hamden

Submitted in partial fulfillment of the
requirements for the degree
of Doctor of Philosophy
in the Graduate School of Arts and Sciences

COLUMBIA UNIVERSITY

2014

ABSTRACT

FIREBall, CHαS, and the diffuse universe

Erika Tobiason Hamden

The diffuse universe, consisting of baryons that have not yet collapsed into structures such as stars, galaxies, etc., has not been well studied. While the intergalactic and circumgalactic mediums (IGM & CGM) may contain a majority of the baryons in the universe, this low density gas is difficult to observe. Yet it is likely a key driver of the evolution of galaxies and star formation through cosmic time. The IGM provides a reservoir of gas that can be used for star formation, if it is able to accrete onto a galaxy. The CGM bridges the IGM and the galaxy itself, as a region of both inflows from the IGM and outflows from galactic star formation and feedback. The diffuse interstellar medium (ISM) gas and dust in the galaxy itself may also be affected by the CGM of the galaxy. Careful observations of the ISM of our own Galaxy may provide evidence of interaction with the CGM. These three regions of low density, the IGM, CGM, and ISM, are arbitrary divisions of a continuous flow of low density material into and out of galaxies.

My thesis focuses on observations of this low density material using existing telescopes as well as on the development of technology and instruments that will increase the sensitivity of future missions. I used data from the Galaxy Evolution Explorer (GALEX) to create an all sky map of the diffuse Galactic far ultraviolet (FUV) background, probing the ISM of our own galaxy and comparing to other Galactic all sky maps. The FUV background is

primarily due to dust scattered starlight from bright stars in the Galactic plane, and the changing intensity across the sky can be used to characterize dust scattering asymmetry and albedo. We measure a consistent low level non-scattered isotropic component to the diffuse FUV, which may be due in small part to an extragalactic component. There are also several regions of unusually high FUV intensity given other Galactic quantities. Such regions may be the location of interactions between Galactic super-bubbles and the CGM. Other ways of probing the CGM including direct detection via emission lines. I built a proto-type of the Circumgalactic Hα Spectrograph (CHαS), a wide-field, low-cost, narrow-band integral field unit (IFU) that is designed to observe Hα emission from the CGM of nearby, low-z galaxies. This proto-type has had two recent science runs, with preliminary data on several nearby galaxies. Additional probes of the CGM are emission lines in the rest ultra-violet. These include OVI, Lyα, CIV, SiIII, CIII, CII, FeII, and MgII. Such lines are accessible for low redshift galaxies in the space UV, historically a difficult wavelength range in which to work due in part to low efficiency of the available detectors. I have worked with NASA's Jet Propulsion Laboratory to develop advanced anti-reflection (AR) coatings for use on thinned, delta-doped charge coupled device (CCD) detectors. These detectors have achieved world record quantum efficiency (QE) at UV wavelengths (>50% between 130 nm and 300nm), with the potential for even greater QE with a more complex coating. One of these AR coated detectors will be used on the Faint Intergalactic Redshifted Emission Balloon (FIREBall-2), a balloon-born UV spectrograph designed to observe the CGM at 205 nm via redshifted Lyα (at z=0.7), CIV (at z=0.3), and OVI (at z=1.0). FIREBall-2 will launch in the fall of 2015.

Contents

List of Figures

List of Tables

ACKNOWLEDGMENTS

Thank you all!

This thesis is the result of many years of work, and owes its existence to so many people who helped me along the way.

Firstly, I must thank my advisor David Schiminovich, who has, above all other things, given me great advice. I am fortunate in having had an advisor who can provide help on nearly any subject, who has so many good projects to work on, has patiently edited out all of my extraneous adjectives, and who loves food as much as I do. I hope that one day I will be as good a scientist and advisor as he is.

My great thanks to Shouleh Nikzad, who was kind enough to welcome me into her group at JPL so many years ago, and kept me around all this time. I can't express how exciting it was to arrive on my first day at JPL, and thanks to Shouleh, it has continued to be exciting. She has provided advice, support, comments, encouragement, and been a role model for me, and I look forward to continuing our relationship in the years to come.

My thanks to Kathryn Johnson, who served as my first year project advisor. She provided a view into a theoretical path not taken, and I appreciated her advice and help through the years.

Many thanks to my undergraduate thesis advisers, Pat Slane and Andy Szentgyorgyi, at the Center for Astrophysics. Without their patient guidance in my first research experiences, who knows what I would be doing today.

Thanks also go to the great scientists at JPL, who have been a delight to work with.

My work is just a small part of the overall project and could not have happened without Alex Carver, Sam Chang, Tim Goodsall, Frank Greer, John Hennessy, Michael Hoenk, April Jewell, and of course, Todd Jones.

I must also thank the FIREBall Team at Caltech, especially Chris Martin, for serving on my defense committee, being the boss of us all, and providing the vision behind some many great projects. Thanks also to Cherie Capri, Nicole Lingner, Mateusz Matuszewski, and Patrick Morrissey.

Thanks are also due to Mark Seibert, whose enthusiasm for the diffuse UV background is second to none.

I must thank so many people at Columbia University, who made my experience a joy. Thanks to Mary Putman and Frits Paerels for serving on my thesis committee and providing years of guidance. Thanks to Lia Corrales, Yuan Li, and Josh Schroeder, for your support in this last year. Thanks to Sam Gordon for becoming an expert in so many subjects so that I didn't have to. I will miss having you around! Thanks to Hwei-Ru Ong, Ben Tam, David Stenning, and Richard Joyce for their work in the lab. Thanks to my office mates, Steven Mohammed and Christine Simpson for putting up with my standing desk and land grabs. Thanks to David Hendel for being a fantastic roommate and office-mate. Who else could I have spent 23 hours a day with me and not gotten annoyed at? Thanks to Millie Garcia, Ayoune Payne, Trudy Reyes, and Francisco Feliciano for their help with everything else and making sure I got paid.

Thanks to all of my great friends, who have supported me even when they had no idea what I did during the day except that it involved space. Thanks Danielle Mazandi, Aaron

Chadbourne, Leslie Wulff, Rucha Vankudre, Laura Amar-Dolan, Lynne Chang, Kyle Parfry, Tim Morton, Jon Blazek, Vera Gluscevic, Sam Shulman, Lisha Perez, and so many more. My universe is a little brighter thanks to each of you.

Thanks especially to my amazing family, who encouraged my enthusiasm for science and learning from the day I first learned about the Big Bang. I so appreciate their happiness for my successes and their pride in my accomplishments. I hope I will continue to make you proud in all that I do.

Finally, thanks to Cameron Hummels, who is the greatest.

2014, New York City

Chapter 1

Introduction

Our ability to ask questions about the universe is always a few steps ahead of our capacity to observe it. Progress is made through a cycle of new technology yielding new scientific results which create new questions that require yet new instruments to answer. This loop replays itself over years and decades and can be seen in sub-fields as diverse as exo-planet detection, gravitational wave observations, and galaxy formation and evolution. The fundamental tension between what we want to understand and the instruments and observations necessary to gain that understanding is what drives my work.

A rough census of the energy contents of the universe leads to a division into two parts (Fukugita & Peebles 2004). The largest by energy is the dark sector, containing dark matter and dark energy and together totaling 95.4% of the energy budget. The remaining 4.6% (less a tiny amount of thermal and binding energies) is primarily baryonic matter. Out of these baryons, a careful census can account for only a fraction of the total. The remainder (30-40% Cen & Ostriker 1999; Davé et al. 2001), is likely contained in the intergalactic and

circumgalactic mediums (CGM,IGM), which consist of low density gas that has not been well studied. A better understanding of the components of the CGM and IGM is important both from a cosmological perspective, in tracing and understanding all components of the universe, as well as from a standpoint of galactic evolution, in understanding how galaxies grow and evolve through star formation rates. Closer to home, the low density interstellar medium of our own galaxy can provide an important test of the interactions between a galaxy and its IGM.

This thesis is an examination of the low density universe using data obtained with existing telescopes as well as a discussion of technology and instruments in development which will provide a clearer view of the universe in the future.

1.1 The Intergalactic & Circumgalactic Mediums

The IGM can roughly be understood as material outside of galaxies that has not condensed into structures such as stars, planets, black holes, etc. While definitions vary, here we characterize the IGM as not gravitationally bound to any one galaxy and with two components. The first consists of low density gas $\delta < 1000$ at low temperatures (T$<10^5$ K). This gas is the remnant of hierarchical structure formation and is the gas detected via Lyman-α absorption features in the Lyman-α forest. The second component is the Warm Hot Intergalactic Medium (WHIM), with temperatures ranging from 10^5 to 10^7 K (Davé et al. 2001). The WHIM contains more observable atomic species than the cold IGM, with ionized O, C, N, and Mg (Bregman 2007) among other metals, a result of feedback from galaxies.

The CGM consists of gas that bridges the cosmic scales of the CGM and the smaller

scales of a galaxy. Typically this gas is gravitationally bound to the galaxy and acts as an intermediary between the low density CGM and the high density galaxy. The CGM is a dynamic place with both inflowing and outflowing gas, the result of galactic outflows, gravitationally heated in-falling CGM gas, and potentially cold flows of CGM gas. The CGM is a key component to understanding how individual galaxies grow and evolve. Evidence from limited observations of the gas content of galaxies and from computer simulations of galaxy evolution points to the flow of gas into and out of galaxies as an important part of setting the star formation rate and other characteristics of a galaxy (Kereš et al. 2005, 2009; Hopkins et al. 2011).

Observational advancements in the last decade have driven our understanding of the history of star formation and its effect on galaxy growth. Recent surveys have probed the pace at which galaxies produce new stars through cosmic time (Schiminovich et al. 2005; Hopkins & Beacom 2006; Salim et al. 2007; Bouwens et al. 2009; Reddy & Steidel 2009; Magnelli et al. 2009, and many others). The rate of star formation shows significant evolution since the Big Bang: from low rates in the early universe, increasing to ten times the current value when the universe was a few billion years old, and then declining ever since. With a clear picture of the multi-dimensional CGM around galaxies (including position information, but also velocity, temperature, density, and metallicity data), we can begin to untangle the complex relationship between a galaxy's history, environment, and morphology.

1.1.1 Lyman-α Forest and the IGM

The first evidence of the existence for large scale, diffuse structures in the universe was found by Lynds (1971), who noticed significant absorption features in the spectrum of a distant quasar. These absorption features, termed the Lyman-α forest, are the result of small amounts of neutral hydrogen gas (δ = 1-10) in an otherwise ionized medium, interspersed between the observer and the background quasar. The forest and, at high enough redshifts, Gunn-Peterson Trough (Gunn & Peterson 1965; Becker et al. 2001) indicate the presence of significant amounts of matter in regions of space without obviously bright galaxies. These observations further point to the presence of an extragalactic ultraviolet background (EUVB), which has ionized most of the IGM. Measurements of the Gunn-Peterson trough indicate the EUVB began to significantly alter the ionization of the IGM at z$\sim$6, although the exact nature of how the universe was re-ionized is still unclear (White et al. 2003; Fan et al. 2006).

1.1.2 Expected emission from the IGM & CGM

Emission from the IGM is the result of a number of different cooling pathways. The primary cooling method of diffuse IGM gas is via line emission (estimated to be $\sim$70% of the energy emitted at z=0), with nearly 80% of the total cooling energy emitted in the rest UV (100-3000 Å) (van de Voort & Schaye 2013; Bertone et al. 2013). These calculations assume a metallicity of $\sim$0.1 solar, with the caveat that increased metallicity also increases the number of available cooling channels. The atomic transitions with the most energy (Ly-α, OIII, CII, CIII, SiII, SiIII, FeII and SIII) are almost exclusively found at rest UV wavelengths. Ground based telescopes, including recent and upcoming instruments such as the Keck Cosmic Web

Imager (KCWI), can observe these transitions in high z galaxies, where they are redshifted into the visible part of the spectrum. For nearby, low-z galaxies, these lines are generally only accessibly in space or at balloon altitudes.

As an alternative to UV emission lines, one can also target Hα (Balmer-α, at 6563 Å) emission, which is formed from the recombination of ionized hydrogen. In the CGM, Hα emission comes from at least two sources: photo-ionization or collisional ionization. Photo-ionized gas typically traces recent star formation and hot young stars, but may also be caused by the extragalactic UV background (EUVB). Collisionally ionized gas will trace shocks and may provide a tracer of hot outflows from galactic supernovae. Both sources of Hα emission can provide important details about the CGM of a galaxy.

1.1.3 Outflows & Cold Flows

In the classical picture of galaxy formation, material in-falling from the IGM will shock heat to the virial temperature at around the virial radius of a galaxy. In this case, the gas will form a thermally supported halo and cooling times may be significant. More recently, simulations have indicated that there may be another mode for in-falling IGM gas to accrete onto a galaxy (Kereš et al. 2005, 2009). This alternative method is known as cold-mode accretion, where cold flows of IGM gas are not shock heated and instead are funneled along dark matter filaments into the galaxy. Cold mode accretion can provide a large mass of gas for immediate star formation, increasing star formation efficiency of a galaxy. More recent simulations indicate that warm-ionized gas may be an important component of galactic gas accretion (Joung et al. 2012). Actual evidence for cold flows is limited, although recently

built instruments such as the Palomar Cosmic Web Imager (CWI) and others may detect them in the coming years (Martin et al. 2014).

In addition to cold flows, the CGM of a galaxy will likely contain hot outflows from galactic feedback. Supernovae winds, AGN feedback, and other violent processes will eject gas from the galactic disk out into the CGM. If the galaxy is small enough, or the event energetic enough, some of this gas will escape the galaxy to pollute the IGM (Hopkins et al. 2012). Numerical simulations of galaxy growth are mixed regarding if cold flows are quenched by strong feedback or not (Hummels et al. 2013; Shen et al. 2013), and at what redshift the suppression of cold flows may occur. These questions are further obscured by the numerical considerations and feedback prescription methods that different numerical codes utilize. Given the abundance of processes that shape the CGM and thus shape the galaxy, detailed observations of CGM gas to compare with simulations are vital to understanding galaxy growth.

1.1.4 Absorption measurements of the CGM

The low surface brightness of both IGM and CGM gas has limited attempts to observe it– gas emissivity scales as the square of density which is quite low in these regions (over-density $\sim$1000). Alternative methods to detect this gas employ absorption line studies, where the signal scales directly as density and is thus easier to detect. Previous observational programs to probe the CGM have relied on 1-D "pencil beam" observations of the outskirts of galaxies in lieu of then impossible direct detections (Hennawi et al. 2006; Ribaudo et al. 2011; Steidel et al. 2011; Thom et al. 2012; Tumlinson et al. 2013).

These "pencil beam" methods use distant bright objects, typically background quasars, but a few studies use supernovae or GRBs as probes of their host galaxies (Le Floc'h et al. 2006; Chen 2012). The spectra of these bright background objects can show evidence for absorption signatures from the intervening IGM or CGM gas of a foreground galaxy. The most common emission lines detected are Lyman-α, MgII, and additional highly ionized metals. Abundances, temperatures, and the optical depth of the absorbing gas can be determined and matched to nearby galaxies by the redshift of the absorption lines. Information from many quasar sightlines can be combined to statistically infer the properties of the CGM around galaxies as a function of impact parameter and ionization species detected.

A host of studies exploit background quasars to detect absorption lines from the CGM. These include the COS-Halos survey (Tumlinson et al. 2013), which attempts to probe 44 L^* galaxies for HI, and other absorption lines, at redshifts between 0.15-0.35 using background quasars with impact parameters up to 150 kpc. Another similarly structured study is the Keck Baryonic Structure Survey (Rudie et al. 2012), which exhaustively searches for galaxies around very bright quasars. Other studies use pairs of two coincident quasars, using the background quasar to probe the CGM of the foreground quasar (Hennawi et al. 2006).

These measurements combine observations of galaxies with similar characteristics to compare detected absorption lines and widths over a range of impact parameters. There is excellent evidence for absorption from a wide range of species and temperatures- H I, tracing cool gas, and OVII, probing hot gas (T$\sim 10^6$K) (Prochaska et al. 2011; Chen et al. 2010, 2001; Tumlinson et al. 2011; Yao et al. 2008). More recent work has found evidence for low ionization state MgII, Si, and C (Werk et al. 2013), indicating that cool components

($T<10^5$K) are fairly common in L^* galaxies. Generally detections of these metals indicate a decreasing column density with distance from the host galaxy (Hummels et al. 2013), although there is significant scatter.

These methods are limited by a reliance on serendipitous and random sightlines which only illuminate a single beam through the CGM of a galaxy, the 1-D "pencil beam" of information through a galaxy halo. With only one or two sightlines per galaxy there is no straightforward way to distinguish between the presence of gas in filaments, a random collection of unconnected gas clumps, or a smooth distribution of gas filling the galactic halo. Statistical combinations of many different galaxies also obscure the connection between the CGM and physical properties of individual galaxies that may be significant. Observations of the HI distributions of galaxies show a range of interesting behaviors, including warps, tidal tails, anti-rotating gas disks, etc. (van der Kruit & Freeman 2011). The nuances of these behaviors are lost with observations restricted to a handful of sightlines or to many galaxies statistically stacked. Additionally, because the rest wavelengths of most significant emission/absorption lines are in the far ultraviolet (FUV), very nearby galaxies cannot be easily observed, despite being larger on the sky and having many quasars behind them.

1.1.5 Direct detection of CGM emission

An alternative to using quasar and other sightlines is to instead observe the IGM and CGM in emission. Direct observations of the CGM would yield currently missing attributes of CGM gas. There are a number of potential ways beyond quasar sightlines to observe the CGM, including using an integral field unit, ultra-narrow band imaging, and statistical stacking.

Only with the first method does one maintain both position and velocity information for individual galaxies.

Observations using an integral field unit (IFU) can cover broad swaths of the CGM around an individual galaxy. An IFU can provide not just x and y information but also velocity measurements, enabling detection of emission lines, temperature diagnostics, inflow/outflow information, and reducing the sky background uncertainty. Instead of relying on background objects which severely restrict the region probed, direct observations can be performed on an unbiased galaxy sample which evenly covers physical space.

1.2 The Interstellar Medium

The Galactic Interstellar Medium (ISM) is interesting for a number of reasons. The Galactic ISM encompasses a range of amazingly complex processes and phases- from cold, dense molecular gas to hot HII regions to coronal gas. These regions co-exist at a range of temperatures, densities, and metallicities, both determined by and in turn determining the star formation of the Galaxy (McKee & Ostriker 1977; Draine 2011). Observations of the ISM can yield important information about the dust, gas, and metal content of the Galaxy, as well as Galactic magnetic fields (Clark et al. 2014). Our knowledge of the local ISM can then be applied to extra-galactic observations. Precise measurements of Galactic foregrounds are crucial for cosmological observations, while the effects of Galactic absorption must be mitigated in many other astronomical applications. Finally, the ISM, as a destination of the material inflowing from the IGM and CGM, probes our own Galactic CGM and environment.

The emission from the ISM in the far UV is an especially important component for ob-

servations of the diffuse CGM and IGM. The expected emission from the CGM is significantly below that of the sky background in the FUV. The expected sky line/band background in the FUV is quite low (<10000 photons s^{-1} cm^{-2} sr^{-1}) but still can be significant when observing targets with intensities <100 photons s^{-1} cm^{-2} sr^{-1} (Milliard et al. 2010). Thus a thorough understanding of the components of the sky background is a key part of CGM observations. These foregrounds come from zodiacal light, airglow, and the Galaxy itself. My thesis work investigating the FUV component of the diffuse Galactic background is scientifically interesting on its own, but is also useful in removing that background for deeper observations. The primary component of the diffuse Galactic FUV background is dust scattered starlight from UV bright stars in the galactic plane (Hamden et al. 2013). In the context of CGM observations, this continuum emission acts as an additional source of sky background. Our understanding of its origin, nature, and variability (spatial as well as spectral) is essential for correctly removing all backgrounds from CGM spectra.

1.3 Instruments

A substantial concern of my thesis was both the development and use of instruments to observe the diffuse material described in Sections 1.1 and 1.2. In the case of the Galactic ISM, data from an existing telescope was re-purposed to provide a view of the diffuse Galactic FUV background for the whole sky. For observations of the CGM and IGM, I worked on telescopes and instruments which spanned a range of sizes, complexities, wavelengths, and costs. This includes developing mission enabling technology for future missions not yet funded, components for a mission with an imminent launch, and a smaller instrument which

could be designed, built, and integrated end-to-end at Columbia with a low budget. Here I briefly describe qualities of the instruments and contrast their performances and specialties.

1.3.1 GALEX

The Galaxy Evolution Explorer (GALEX), a 0.5 meter modified Ritchey-Chrétien telescope, operated for 10 years after its launch in 2003 (Martin & GALEX Science Team 2003; Martin et al. 2005). In our work on the diffuse FUV background, we use data from the all sky survey (AIS), covering more than 25,000 square degrees on the sky with typical exposure time of 100 seconds, reaching a limiting point-source magnitude (m_{AB}) of 19.9 (5 σ AB; Morrissey et al. 2007). Each pointing center was chosen to minimize the gaps between adjacent fields. While GALEX avoided bright stars in the Galactic plane and other regions, there is good coverage at higher latitudes. We use images from the GALEX data release general release 6 (GR6), which contains a total of 34,551 individual AIS pointings. GR6 contains nearly all the AIS FUV data taken during the GALEX mission.

GALEX was well suited to our study of the diffuse Galactic FUV background for a number of reasons. GALEX has a large field over view, over 1 degree in diameter, and operated for 10 years, giving it time to conduct a survey of nearly the whole sky. GALEX had high spatial resolution in the FUV, so small details, dust clouds, shock fronts, etc., in the ISM are visible in detail. Because the primary objective of the GALEX mission was observing the evolution and structure of galaxies on an all sky scale, there is a comprehensive point and extended source catalogue in the GALEX archives. With this catalogue, bright galactic stars and background galaxies are easily masked to reveal only the diffuse Galactic

light. GALEX avoided the brightest sources, due to the count rate limits of the MCPs, and focused on dimmer regions of the galaxy away from the Galactic plane.

1.3.2 FIREBall & ISTOS

The Faint Intergalactic Red Shifted Emission Balloon (FIREBall-2) is a balloon-borne UV spectrograph funded jointly by NASA and CNES. FIREBall-2 uses a one meter primary mirror to feed a multi-object spectrograph optimized for narrow-band observations centered around 205 nm. The primary science goal of FIREBall-2 is to observe the diffuse gas around galaxies, known as the circumgalactic medium (CGM), via redshifted line emission. The main targets are emission from Lyman-α (121.56 nm) at a redshift of z=0.7, CIV at z=0.3, and OVI at z=1.0.

A previous version of the mission, FIREBall-1 was launched on two occasions, in 2007 and 2009, from Fort Sumner, New Mexico (Tuttle et al. 2008; Milliard et al. 2010). FIREBall-1 was a fiber-fed spectrograph which used an Offner design and a GALEX-spare near-UV microchannel plate (MCP) (Doliber et al. 2000; Tuttle et al. 2010). FIREBall-1, while a technical and engineering success, recorded data consistent with no detected signal at the 20,000 line unit (LU, 1 photon s^1 cm^2 sr^1) level. This result indicated a need to lower the detection limits for FIREBall-2 and drove the changes made to the current spectrograph and the replacement of the MCP detector. The spectrograph of FIREBall-2 has since been redesigned extensively. A field correcter will be placed before the spectrograph optics to increase the field of view. The fiber bundle IFU has been replaced with a slit mask, increasing throughput and number of targets per field. The spectrograph itself will consist of

two identical f/2.5 Schmidt telescopes acting as collimator and camera, with an improved grating. A number of other, smaller changes have followed from these large modifications. A rotational stage has been included to select masks for different fields and we redesigned the guider system, associated optics, and calibration system. Most crucially, the MCP detector has been replaced with a UV optimized, electron-multiplying, delta-doped detector. This thesis describes in detail the development, deposition, and testing of anti-reflection coatings for these detectors. Work on the FIREBall-2 spectrograph, in particular the Mask-Guider system, is also described here.

A proposed space telescope, the Imaging Spectroscopic Telescope for Origins Surveys (ISTOS), will build on the technology developed for FIREBall and shares many of the same goals. ISTOS will access a wider wavelength range in the space UV and utilize a field slicer in place of the multi-object spectrograph. The detector technology described in this thesis is a mission enabling component of the ISTOS project, and many of the remaining questions regarding flight qualification of these devices will be answered in preparation for and during the FIREBall flight. These questions include the ability to cool the detector, reaching sufficiently low dark current levels, the amount of clock induced charge (CIC), the charge transfer efficiency (CTE), the overall QE, and other sources of noise. A successful FIREBall run will increase the technology readiness level (TRL) of these devices and pave the way for their use in space.

1.3.3 CHαS

Ground-based studies looking for emission are relatively new, yet will likely be crucial in fully understanding the behavior and makeup of the CGM. Lyman α, at 1216Å, is predicted to be the brightest emission line from any CGM signal, with Balmer α, or Hα, at 6563Å the brightest rest-frame visible line. Studies looking for emission from the CGM via Lyα must go to higher redshifts, when the signal is shifted into wavelengths visible to existing spectrographs. But emission at Hα can be visible at low redshift without having to go to space or higher z. This provides an advantage in terms of cost and telescope time. Bright Hα emission has been detected close to the disks of nearby spiral galaxies, known as extended Hα disks (Madsen et al. 2001; Christlein et al. 2010), and emission from outlying HII regions appears to scale with the star formation rate of the galaxy (Werk et al. 2010). The presence of extended UV disks or nearby companions appears to correlate with these HII regions.

Hα studies of the CGM around low-z galaxies will be highly complementary to an eventual space-UV search of CGM emission via UV emission lines. The Circumgalactic Hα Spectrograph (CHαS), is an example of an instrument designed for just such a program. CHαS is a monochromatic, low-cost, nebular spectrograph designed to be a facility instrument for the 2.4 m Hiltner and 1.3 m McGraw-Hill telescopes at MDM Observatory on Kitt Peak. A narrow-band filter (width of $\sim$ 30 Å) feeds a fast spectrograph with a dioptric Petzval collimator and camera, and a mechanically ruled grating. CHαS uses a micro-lens array as a field slicer and to speed up the telescope beam from f/7.5 to f/1.87.

CHαS has been designed specifically to detect both the presence of Hα emission in the outskirts of a galaxy and the dynamics of any emitting gas. This 3D picture is achieved

using an integral field unit to capture both 2D spatial information and spectral information for a wide field, but over a narrow wavelength range.

1.3.4 Performance and Design

GALEX, FIREBall, and CHαS at first glance have significant differences from one another. The GALEX mission has already been completed and our work re-purposed existing data. CHαS is still in proto-type stage, and Prof. Schiminovich awaits notification from the NSF regarding the proposal to build CHαS. FIREBall is in an intermediate state, having been launched twice. Preparations are underway for a third launch with the newly redesigned spectrograph.

GALEX differs significantly in that it was an imaging telescope, operating in only two channels. At the time that GALEX was under development, MCPs offered the best quantum efficiency (QE) and noise characteristics out of the technology available for flight. These detectors are unable to handle high count rates, and so GALEX avoided bright stars and the Galactic plane until the very end of its lifetime. GALEX was an incredibly successful mission, one which significantly advanced our understanding of the evolution of galaxies and star formation rates through cosmic time (Schiminovich et al. 2005). As discussed above, GALEX's large field of view and all sky coverage make it good for observations of the diffuse FUV background. Precise measurements of the Galactic component of the FUV background will be useful in removing sky background from future observations.

FIREBall is in many ways an extension of the work that began with GALEX. FIREBall overlaps some of the same NUV wavelengths as GALEX and seeks to explain the reasons

behind the galaxy evolution that GALEX detected. This requires both increased sensitivity and spectroscopic capabilities, first to detect emission from warm gas in the CGM that is significantly dimmer than the central galaxy, and second to provide spectral information on that gas. A multi-object spectrograph will provide many targets per field ($\sim$50) and a high contrast between the target emission lines and the sky background. FIREBall-2 has been designed with these specifications in mind, and in particular has focused on increasing sensitivity beyond that of FIREBall-1. The choice of a slit-mask instead of using a fiber IFU both increases the number of targets and increases the overall throughput. The selection of targets, focusing primarily on Lyα at redshift 0.7, focuses on the brightest emission line to maximize the chances of detecting emission. In attempting to increase sensitivity beyond GALEX, NASA's Jet Propulsion Laboratory (JPL) has been developing silicon based detectors for use at UV wavelengths. The GALEX MCP detector technology was also used on FIREBall-1, but is being replaced with a delta-doped electron multiplying CCD (EMCCD). FIREBall will serve as a test bed of both the UV optimization of these detectors as well as the use of EMCCDs for photon-counting observations. In this way, FIREBall also serves as a test bed for a potential future UV space mission.

Finally, CHαS points to the importance of continuing observations on the ground at the same time as working on future space technology. The multi-wavelength nature of the CGM/IGM means that there are a number of ways to probe the gas, provided one has flexibility in methods and observing time. By moving to Hα, one can still probe galaxy evolution on the ground in a less expensive format. CHαS also occupies a unique parameter space of very high grasp ($A_{eff} \times \Omega \sim 100$ m^2 arcmin^2) with medium resolution (R$\sim$5000),

while also making use of under-subscribed optical telescopes. To make the most of observing time, CHαS looks at nearby galaxies that efficiently fill the field of view. Working on a prototype of CHαS also provided a unique perspective on the end-to-end process of instrument building, integration, and data pipeline construction.

Table 1.1 shows performance parameters of the three main instruments discussed in this thesis. One important difference that is clear from the Table is the relative difficulty of observations of the CGM/IGM compared to observing continuum emission from the ISM. GALEX is able to detect dust scattered starlight with short exposure times of 100 seconds, while FIREBall-2 requires exposure times over x30 as long for an observation of the CGM. This difference is due both to the faintness of expected CGM emission (10^3 LU, photon cm^{-2} s^{-1} sr^{-1}) compared to dust scattered Galactic starlight ($\sim$hundreds of CU, cm^{-2} sec^{-1} sr^{-1} Å^{-1}), and the effect of taking spectra instead of imaging. The faintness of the CGM relative to background is one reason that the FIREBall-2 team has pushed so hard at developing technology to increase instrument sensitivity. The faintness of the CGM is also the primary reason that these important observations are only now being conducted.

[1]Assuming standard NII filter
[2]AIS typically exposure time. GALEX max exposure time $\sim$30000 for Deep Imaging Survey (DIS)
[3]Facility STA detector
[4]Peak
[5]Mean effective area

Quantity	**GALEX**	**CHαS**	**FIREBall-2**	**Unit**
Location	Space	Ground	Balloon	
Type	Imager	IFU	MOS	
Telescope Aperture	0.5	2.32	1.0	m
Channels	2	1	1	
Wavelength Range	FUV (1344-1786) NUV (1771-2831)	6571-6601[1]	2000-2100	Å
Field of View	72 dia	12x15	11x35	arcmin^2
Spectral Resolution ($\Delta\lambda$)	440,1060	1.2	1	Å
Angular Resolution	4.2,5.3	2.5-5	4	arcsec
Field Slicer	n/a	microlens array	slit-mask	
Standard exposure time	100	600	1000	seconds
Exposure time per field	100[2]	36000-360000	3600	seconds
Detector Type	MCP	MDM 4k CCD[3]	EMCCD	
System Throughput	.016, .028[4]	0.18	0.05-0.1	
Effective Area	25, 44[5]	6824	392	cm^2

Table 1.1 Table showing performance parameters of the three main instruments discussed in this thesis. These parameters include wavelength range, type of instrument, resolution, etc.

Chapter 2

The diffuse Galactic far-ultraviolet sky[1]

2.1 Introduction

Dust scattering of starlight by UV bright stars in our own Milky Way is now known to explain the majority of the diffuse far ultraviolet (FUV, ∼1300-1800 Å) background. However, interest in the diffuse FUV background began not with a focus on Galactic dust, but with a search for a cosmologically significant signal from the intergalactic medium (IGM) in order to quantify the total amount of mass and energy in the universe. Kurt & Sunyaev (1970) theorized that high energy photons emitted from dense hydrogen and helium in the IGM could be red shifted into the FUV, detectable as a diffuse isotropic continuum background. A hot Galactic halo had also been proposed by Spitzer (1956) as a source of diffuse FUV

[1]This chapter is a slightly edited version of a previously published paper which appeared in *The Astrophysical Journal*. The full citation for this article is "The Diffuse Galactic Far Ultraviolet Sky". E. T. Hamden, D. Schiminovich, and M. Seibert. *ApJ*, 799:180H, Dec. 2013.

line emission. It is now well understood that these components do exist, although with lower surface brightness than initially theorized.

Among the early observations of the diffuse background were measurements by Morgan et al. (1976), Paresce et al. (1980), Jakobsen et al. (1984), Fix et al. (1989), Hurwitz et al. (1991), Perault et al. (1991), Murthy et al. (1999). While still incomplete in sky coverage, these observations hinted at a correlation between diffuse FUV intensity and Galactic neutral hydrogen column density. This pointed to a Galactic source for the FUV, specifically scattering of UV star light by dust grains. The Galactic origin of the diffuse FUV was more clearly determined with observations showing the correlation between diffuse FUV intensity and the infrared background at 100 μm as measured by IRAS (Jakobsen et al. 1987; Perault et al. 1991; Sasseen & Deharveng 1996). These results were further confirmed and expanded upon by recent missions with better sky coverage and angular resolution. Schiminovich et al. (2001) observed one quarter of the sky in FUV with the NUVIEWS rocket, comparing it to N_{HI} and 100 μm column, and finding a linear relationship at high latitudes. Spectroscopic UV observations of parts of the diffuse sky have also been made by FIMS/SPEAR (Edelstein et al. 2006) and FUSE (Moos et al. 2000). Seon et al. (2011a) use FIMS/SPEAR data and find correlations between FUV and 100 μm, N_{HI}, and Hα. Murthy et al. (2010) use low resolution GALEX all sky data, with bright objects removed, and also find a strong correlation between FUV and 100 μm emission.

While the correlation between diffuse FUV and dust column is now broadly accepted, deviations from this correlation are significant (Seon et al. 2011a; Murthy et al. 2010; Schiminovich et al. 2001). Murthy & Sahnow (2004) found a weak correlation between FUV in-

tensity and 100 μm using FUSE data, potentially due to differences in the local radiation field at low latitudes. On physical scales corresponding to molecular clouds, there can be significant deviations in the relationship between FUV and dust. Observations in Aquila with FIMS/SPEAR (Park et al. 2012) found FUV intensity correlates well with dust column for low extinction sightlines, while there is no correlation in regions with higher dust column. Similarly, in the Draco Cloud, Sujatha et al. (2010) found substantial variations in the relationship between diffuse FUV intensity and 100 μm intensity using GALEX data. The UV/IR ratio varied by a factor of 10 across the cloud. Such divergent behaviors indicate that dust column is not the sole predictor of diffuse FUV intensity.

In the low density ISM, light from UV-bright stars (mostly near the plane of the Galaxy) is scattered off of dust grains, resulting in a low level diffuse FUV brightness which is correlated with dust content. Above a certain threshold density, regions of the ISM may not reflect as much, as thicker clumps of dust attenuate FUV radiation. Witt et al. (2008) and Seon et al. (2011a) find that this shielding begins at 100 μm > 8 MJy/sr, but at a range of FUV values. Additionally, deviations from the FUV-dust correlation may indicate regions of especially high FUV radiation from nearby stars, a region of dust with unusual scattering properties, or even regions where molecular hydrogen is able to form and fluoresce.

Here we present a nearly all sky survey of the diffuse Galactic FUV background and compare the FUV intensity to 100 μm emission, N_{HI} observations, and Hα intensity maps. We employ a masking and mosaicing technique to remove FUV bright sources from all-sky survey images and create a composite map of the GALEX diffuse FUV sky. This map provides unprecedented, wide and deep coverage compared to results from previous missions.

We use this all sky data to investigate the precise nature of the relationship between FUV and tracers of cold Galactic dust and gas across the sky, focusing on how the relationship changes with both Galactic latitude and proximity to various Galactic plane associations. The minimum FUV in these relations is also examined to determine if it reveals a significant isotropic extragalactic component, an un-modelled Galactic component, or another source. The scatter in the relationships, both on large scales and within a single cloud, provide insight into the physical properties of the dust, including scattering asymmetry and albedo. A clear picture of the FUV behavior and what drives it can also allow for the modeling and removal of the Galactic UV foreground.

In Section 2.2 we describe the data products used and any further analysis. In Section 2.2.1 we describe the image mosaicing procedure and initial analysis of the GALEX data set in detail. In Section 2.3 we describe all sky trends and spatial distributions. We discuss in particular the relationship between diffuse FUV and 100 μm emission (Section 2.3.4) and Hα intensity (Section 2.3.5). In Section 2.4 we discuss the implications of our results.

2.2 Data

The Galaxy Evolution Explorer (GALEX), a 0.5 meter modified Ritchey-Chrétien telescope, operated for 10 years after its launch in 2003 (Martin & GALEX Science Team 2003; Martin et al. 2005). GALEX observes in two UV channels (FUV (1344-1786 Å) and NUV (1771-2831 Å)) and has an angular resolution of 4.2 arcseconds (FWHM) in the FUV and 5.3 arcseconds (FWHM) in the NUV. In this paper, we use data from the all sky survey (AIS), covering more than 25,000 square degrees on the sky with typical exposure time of 100

seconds, reaching a limiting point-source magnitude (m_{AB}) of 19.9 (5 σ AB; Morrissey et al. 2007). Each pointing center was chosen to minimize the gaps between adjacent fields. While GALEX avoided bright stars in the Galactic plane and other regions, there is good coverage at higher latitudes. We use images from the GALEX data release GR6, which contains a total of 34,551 individual AIS pointings. GR6 contains nearly all the AIS FUV data taken during the GALEX mission.

Maps of the whole sky at 100 μm were taken from Schlegel et al. (1998). This map of the sky and the corresponding E(B-V) dust extinction maps were made by combining COBE/DIRBE data with IRAS/ISSA maps in such a way as to accurately measure 100 μm emission (without a zero-point offset), which was then also used to derive a column density of dust. This technique is able to estimate the dust at all but the lowest Galactic latitudes and densest clouds to 10% precision. N_{HI} data of the whole sky was taken from NASA's LAMBDA data service. The all sky neutral hydrogen column density information is an interpolation of two maps, Hartmann & Burton (1997) and Dickey & Lockman (1990). The Hartmann & Burton (1997) map is a velocity integrated (-450 km/s $< V_{lsr} <$ +400 km/s) N_{HI} brightness temperature map sampled every 0.5° and converted to N_{HI}. The Dickey & Lockman (1990) map is a composite of several surveys averaged into 1 degree bins in Galactic coordinates with emission from -250 km/s $< V_{lsr} <$ +250 km/s. Hα data is taken from Finkbeiner (2003) and has a 6' (FWHM) resolution. It is a composite of the Virginia Tech Spectral line Survey (VTSS) in the northern hemisphere (Dennison et al. 1998) and the Southern Hα sky survey atlas (SHASSA) in the southern hemisphere (Dennison et al. 1998). The Wisconsin Hα Mapper (WHAM) (Reynolds et al. 2002) provides a stable zero

point at a 1 degree scale.

2.2.1 Image Mosaicing

In order to observe the diffuse background intensity, we create high resolution FUV images with known point and resolved sources removed. To create these mosaics, we use the GALEX data products described in Morrissey et al. (2007) along with the Montage software package (Berriman et al. 2003; Laity et al. 2005).

In our analysis we use four main maps to generate FUV background images: *cnt* (counts per pixel), *rrhr* (relative response or effective exposure time per pixel), *sky* (estimated sky background), and *mask* (detected objects). The sky background file is created by the GALEX pipeline and is an estimate of the smoothed background after resolved and point sources are removed from each image (Morrissey et al. 2007). The *mask* file provides the locations of pixels that contain UV-detected objects, which are removed for background estimation. The flagged pixels in this pipeline mask file—also called a segmentation file by the Sextractor object-detection software used to perform photometry on GALEX images—only contains contiguous pixels from an object that are well detected above background, and may not include extended faint light (or optical ghosts, etc.) associated with an object.

Our mosaicing procedure involves several steps. First we remove resolved sources from each file to be mosaiced, using the *mask* and *cnt* files. The *mask* file is smoothed using a boxcar of width 10 x 10 pixels to place an extra 15″ border around the objects being masked. This is done to more effectively block light from bright stars and galaxies, which can extend beyond the unsmoothed masked area. Even with this extra border a fraction of the light

from an object will remain unmasked. Encircled energy curves for the GALEX FUV PSF indicate that 5% of the light extends beyond 20 arcseconds radius (Morrissey et al. 2007), our typical minimum masked radius. Bright objects will usually have an even larger extent in the object mask, thereby reducing this fraction. This unmasked light is discussed later in the context of excess FUV emission.

For display purposes, the flagged areas on the smoothed *mask* are then excised from the *cnt* files and are replaced with the corresponding section of the *sky* file, which was generated by the pipeline as an estimation of the background in that region. Given the AIS source density, this background replacement has only a small impact on the overall noise in the images. The *sky* file is in units of counts per second, so we multiply the *sky* file by the corresponding regions of the *rrhr* file to maintain the correct units of counts. This can be described by:

$$\begin{aligned} cnt_{masked,i,j} =& mask_{i,j} * sky_{i,j} * rrhr_{i,j} \\ &+ (1 - mask_{i,j}) * cnt_{i,j} \end{aligned} \tag{2.1}$$

where $\text{mask}_{i,j} = 1$ for detected objects. Figure 2.1 shows two different GALEX images before and after this procedure.

The next step was to create a set of GALEX FUV mosaics centered on 12,288 equally spaced points covering the whole sky. Each mosaiced image contains all GALEX AIS fields within a 3 degree radius from the center of the pointing, with some overlap between neighboring images. Using Montage, the *rrhr* and masked *cnt* files are reprojected so all images to be mosaiced lie in the same plane. The overall size of the *cnt* file is also trimmed to remove

the edges. Reprojected files are then mosaiced into large *rrhr* and *cnt* files. The final step is to divide the mosaiced *cnt* file by the mosaiced *rrhr* file, creating a finished mosaic with units of counts per second.

$$I_{cnts/sec} = \frac{cnt_{masked,mosaiced}}{rrhr_{mosaiced}} \tag{2.2}$$

The image units of cnts/sec are then converted to photons $\mathrm{cm}^{-2}\ \mathrm{sec}^{-1}\ \mathrm{sr}^{-1}\ \mathrm{\AA}^{-1}$, hereafter referred to as continuum units (CU). The resulting mosaic is then compared to the all sky maps described above.

GALEX FUV data was not available for a fraction of these points, due to the avoidance of the Galactic plane and other bright objects. The sensitivity of the GALEX detector limited the max count rate for FUV AIS observations to 5000 cnts/s (Morrissey et al. 2007). Of the 12,288 points, 10,019 had GALEX AIS fields within the 3 degree radius, using a total of 28,938 individual GALEX fields. Figure 2.2 shows the percentage of the sky covered by our maps for a given Galactic latitude. The lowest latitude regions ($|\mathrm{b}| < 25^{\circ}$) have coverage below 75%. There is a slight asymmetry between north and south hemispheres in this plot, due to the location of the Orion OB association below the Galactic plane.

Our final step was to create an all sky map, with each image described above sampled onto lower resolution pixels, each covering 11.79 arcmin^2. A total of 12,582,912 pixels cover the whole sky in a nested HEALPix ordering (Górski et al. 2005).

Assuming Poisson errors, with signal to noise equal to the square root of the signal, we find a typical AIS image (with 100 second exposure) will yield a signal to noise of ~ 16 per HEALPix pixel. Regions of the sky with more than one GALEX AIS pointing, overlapping

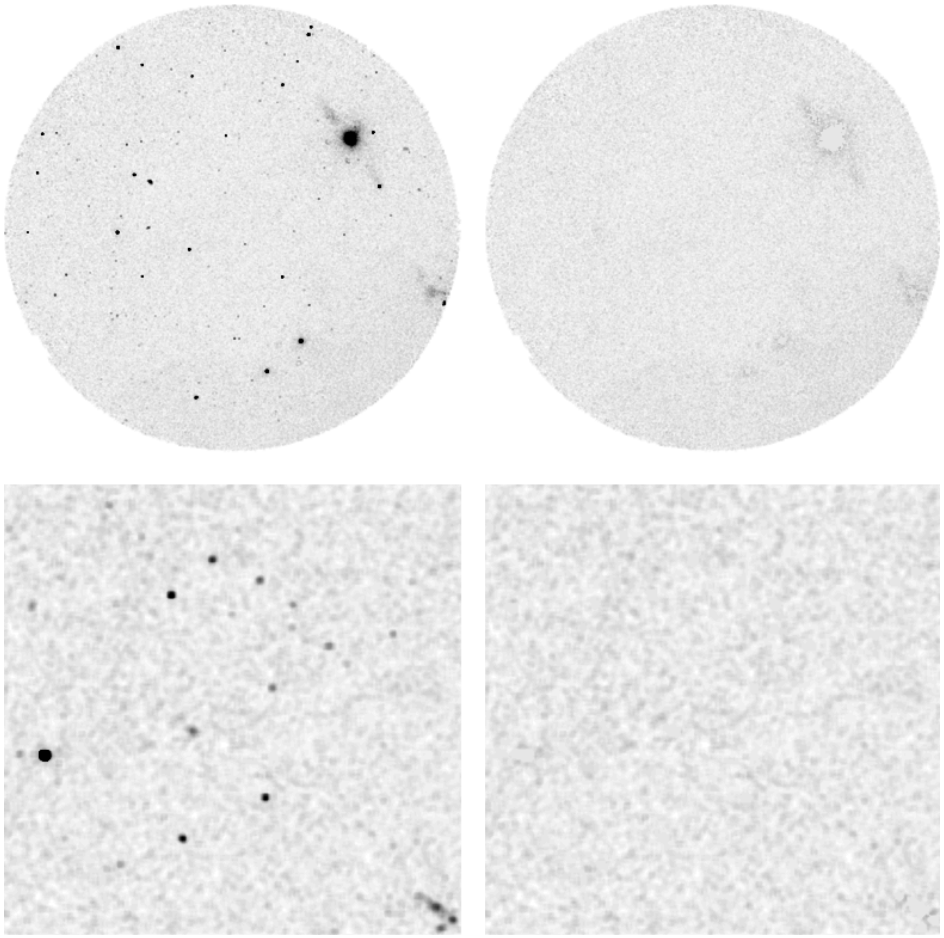

Figure 2.1 Examples of GALEX image masking. **Top Left:** Image of an unmasked GALEX field with a particularly bright A0 star (V=9.48, FUV=12.75, saturated) on the right of the field. **Top Right:** Image of same field after masking. Regions covered by the mask have been replaced by the estimated sky background from the *sky* images (Morrissey et al. 2007). Some reflections from bright stars remain after masking. **Bottom Left:** Close up image of an unmasked GALEX field with dimmer point sources. **Bottom Right:** Image of same field after masking, leaving behind a smooth background.

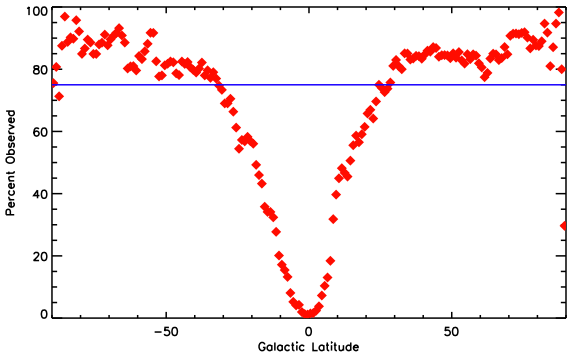

Figure 2.2 Percentage of coverage of GALEX FUV AIS data for a given Galactic latitude in bins of 1°. Light blue line indicates 75% coverage to guide the eye. Regions near the Galactic plane have much lower coverage than higher latitudes. The average coverage above |b|=25° is 81%.

edges of pointings, and averaging over larger areas will yield greater signal to noise values. The all sky map is shown in Figure 2.3. The map contains 65% of the sky, as compared to 25% from Schiminovich et al. (2001), 75% from Murthy et al. (2010), and 80% from Seon et al. (2011a).

2.3 The Diffuse FUV Sky

Here we present the GALEX diffuse FUV all sky map. Figure 2.3 shows the composite map in log scale. At high latitudes, FUV intensity is low, reaching a lower limit of a few hundred CU. At lower latitudes closer to the Galactic plane, the intensity increases to several thousand CU. The growing intensity towards the plane follows a rough cosecant trend with latitude as discussed further below. The highest intensities are found at the edges of known OB associations near dense molecular clouds: Ophiuchus (l=255°, b=18°), the Tau-Per-Aur Complex (l=170°, b=-15°), and the Orion A & B complex (l=200-220°, b=-17°) (Dame et al. 2001).

Seon et al. (2011a) and Schiminovich et al. (2001) both note a "significant depression" in the FUV maps at latitudes above b>20° between l=20° to l=60°. Overall, we find the intensity at mid to high latitudes here is mostly consistent with intensity at similar latitude regions in other parts of the sky. Regions of the sky with unusually high intensity (> 5000 CU) can be linked to the OB associations mentioned above and are related to the uneven distribution of FUV bright stars. Figure 2.4 shows the positions of bright stars ($\mathrm{Flux}_{1565\text{Å}} > 1 \times 10^{-12}$ erg cm^{-2} s^{-1} Å^{-1}) from the TD-1 survey of nearby stars (Perryman et al. (1997), van Leeuwen (2008)). Ophiuchus, the Orion complex, and other areas of high FUV emission have an excess of bright stars.

2.3.1 Galactic Trends

FUV intensity vs. Galactic latitude and longitude are shown in Figure 2.5. The left panel shows diffuse FUV intensity vs. Galactic longitude. Overall, we find this matches well with the diffuse FUV intensity from SPEAR/FIMS described in Seon et al. (2011a). The right panel shows FUV intensity vs. Galactic latitude. FUV intensity increases with decreasing absolute value of the latitude, and appears to be relatively symmetric between northern and southern Galactic hemispheres. The avoidance by GALEX of UV bright regions will bias the latitude-averaged intensity at the lowest latitudes (|b| < 20), evident when compared to Seon et al. (2011a) which reaches values of 10,000 CU in the plane.

Certain Galactic quantities, including column densities and absorption, have been known to follow a cosecant shape with latitude, derived by Parenago (1940) to model Galactic reddening. This model has been expanded and refined, but the basic principle remains

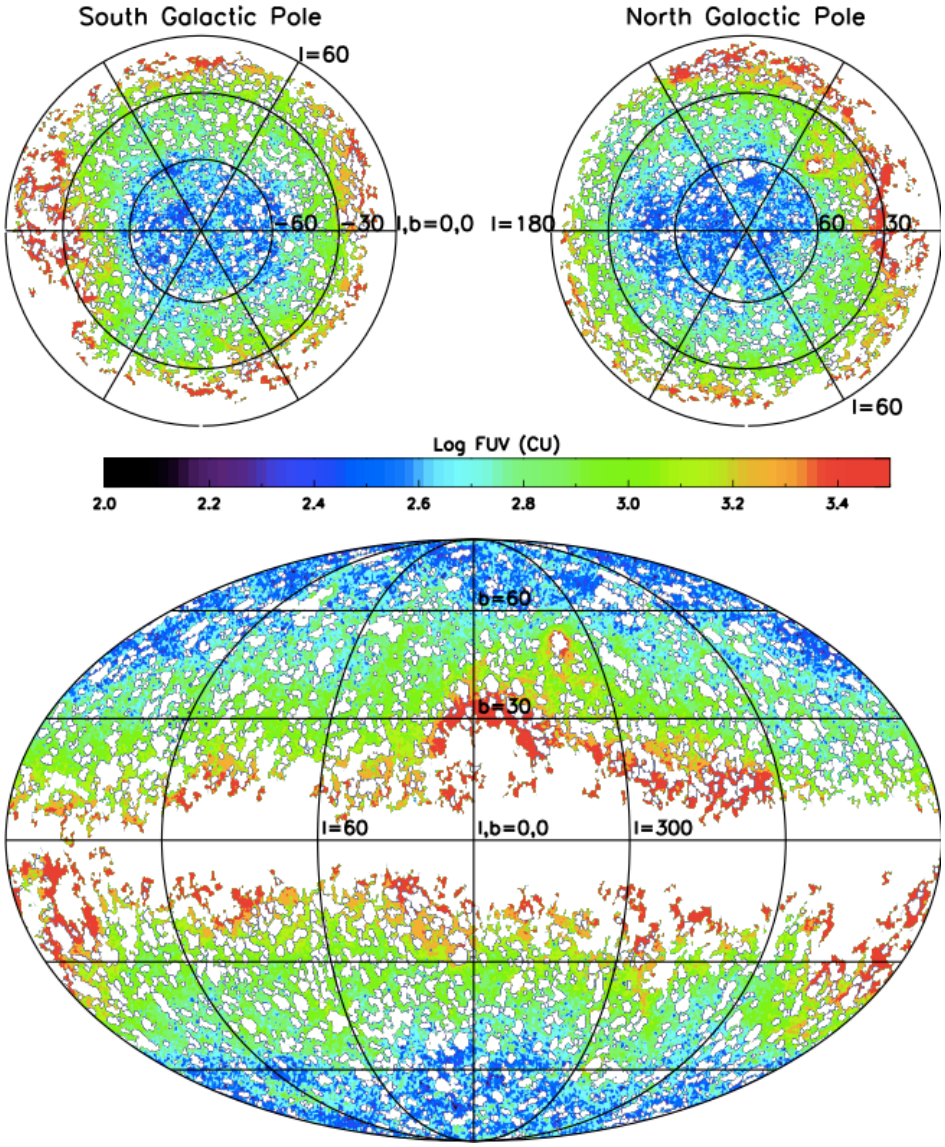

Figure 2.3 Log of diffuse FUV intensity (CU) across the sky. The lowest FUV intensity (a few hundred CU) is at the highest latitudes, while the highest FUV intensity (a few thousand CU) is found nearest to the Galactic plane. The highest intensity observed is at the edges of known OB associations, near dense molecular clouds. Overall intensity is best fit as a modified cosecant with latitude, as is discussed in Section 2.3.1.

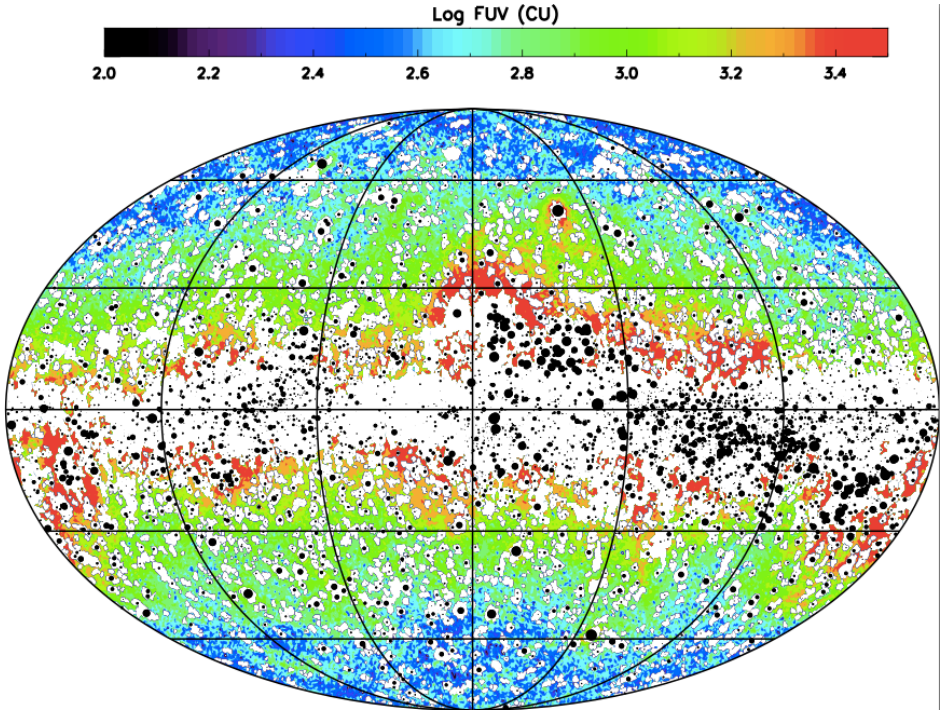

Figure 2.4 Log of diffuse FUV intensity (CU) across the sky, with locations of TD-1 bright stars overplotted. The diameter of the points is proportional to the log of the FUV flux. The coordinates are as in Figure 2.3

the same. Following Milne & Aller (1980) and Sturch (1966), Galactic extinction can be modeled as:

$$C = \int_{r=0}^{d} k_o \xi(z) dr = k_o \csc|b| \times \int_0^z \xi(z) dz \tag{2.3}$$

where k_o is reddening in the plane, z is height above the plane, and $\xi(z)$ is a function that describes how reddening changes with z. Using simple trigonometry, we replace a radial distance with $z = \sin|b| \times r$. The resulting cosecant dependence is shown in the right hand side of Eq 2.3. Several functions have been suggested for $\xi(z)$, including exponential with a scale height (Milne & Aller 1980), although the exact form is not relevant here. If C traces

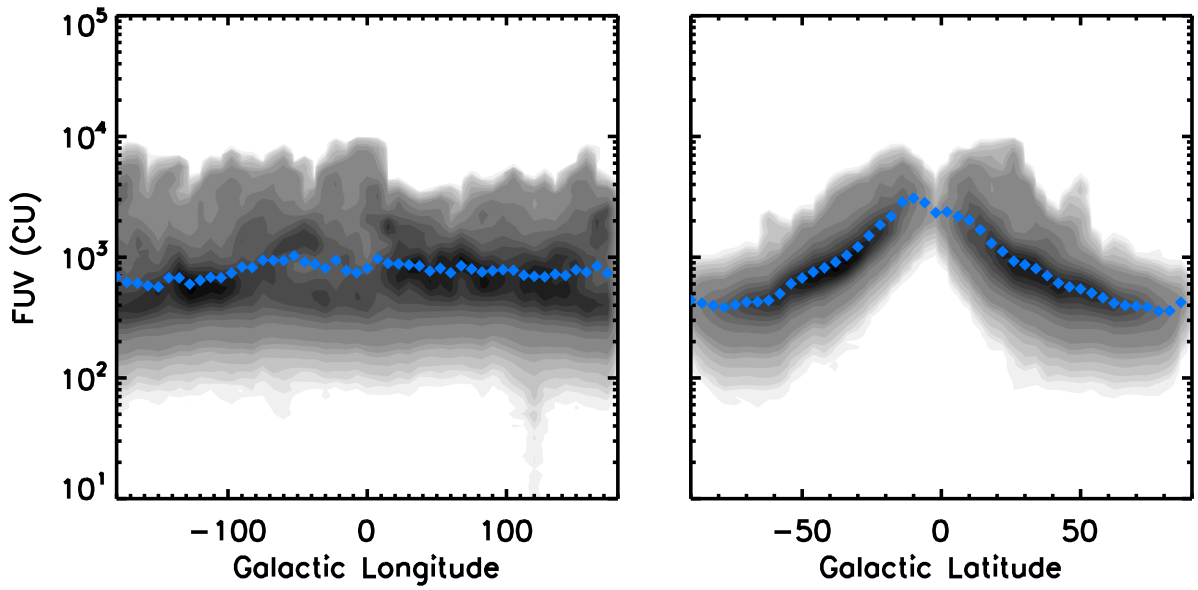

Figure 2.5 **Left:** Plot of FUV vs. Galactic longitude. Blue dots indicate median FUV intensity in 5° bins. Median FUV intensity (800-1000 CU) is relatively constant across longitudes. **Right:** Plot of FUV vs. Galactic latitude. Blue dots indicate median FUV intensity in 3° bins. The lowest latitudes have fewer points since GALEX has not observed the entire Galactic plane.

the amount of obscuring dust and the scattered FUV is proportional to the dust column, then one can relate the two by a scale factor, $k_{scatter}$.

$$I_{FUV} = k_{scatter} \times C \tag{2.4}$$

With a latitude dependent extinction model, we can reasonably expect a latitude dependent FUV intensity. This model has been fit by Perault et al. (1991) and others.

The cosecant dependence of FUV is shown in the left panel of Figure 2.6 which plots FUV sin|b| vs. sin|b|. Including all points, the median FUV sin|b| is 451 CU, slightly lower than the value from Seon et al. (2011a), of 525.4 CU. This difference we ascribe to unobserved high intensity regions as discussed previously. While the unobserved regions are

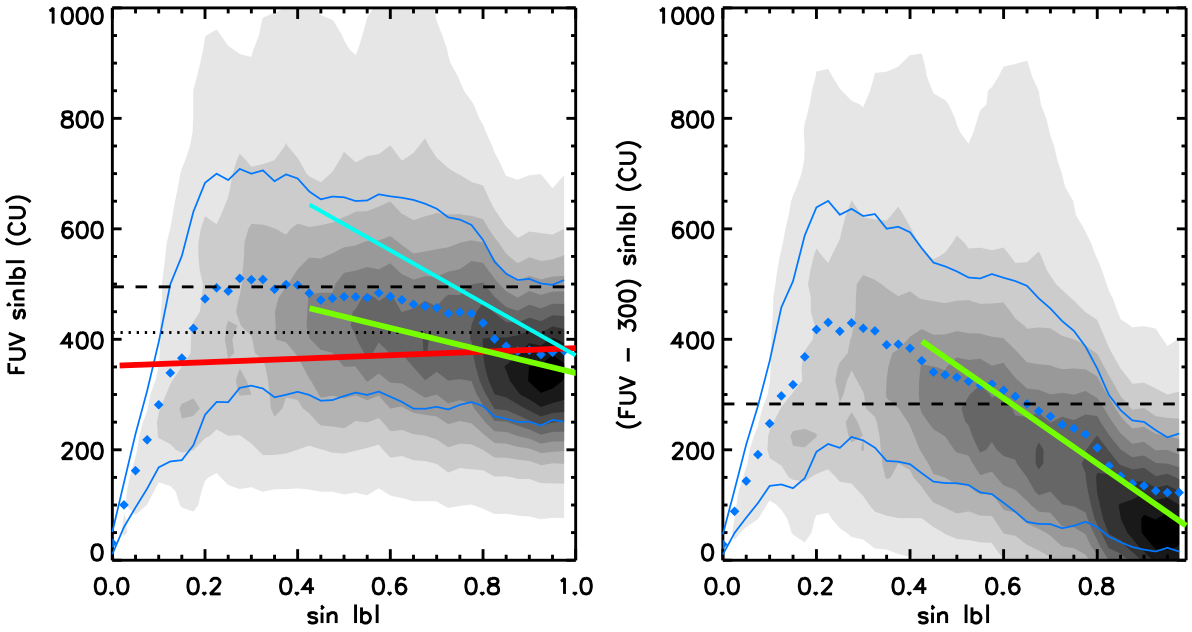

Figure 2.6 Plot of FUV sin|b| vs. sin|b|. **Left:** 2-d histogram of FUV sin|b| as a function of Galactic latitude. The black dashed line is the single parameter fit to FUV sin|b| at all points, 495 CU. The black dotted line is the single parameter fit from Seon et al. (2011a), 412 CU. The green and red lines are best fits for a function of the form I=A/sin|b| + B, with green fitting points above |b|=25° and red for all points. The cyan line is the two parameter fit from Seon et al. (2011a). **Right** 2-d histogram of the same data as the top plots, but with a 300 CU offset removed. The black dashed line is the median for all points, while the green line is a two parameter fit for |b| > 25°.

concentrated in the plane, high intensity areas at all latitudes are not included in our data. Thus an overall lower median for our all-sky data is to be expected. The deviation from a constant value with sin|b| at the lowest latitudes is probably due to the fact that the line of sight is no longer optically thin. At higher latitudes, the behavior is roughly flat, consistent with a cosecant form, with a slight decrease above sin|b|=0.8.

Fitting a function of the form of Equation 2.4 corresponds to a horizontal line on this plot. If we assume FUV=A/sin|b|, we find A=495. This is the dashed line in the plot, compared to 412.3±10.3 (dotted line) from Seon et al. (2011a). This is not a good fit to

our data at any latitude. Adding an additional constant term and fitting a function of the form I = A/sin $|b|$ + D, we find that the values for A and D vary significantly depending on which latitudes are included. The red line shows the fit for all points with |b| > 5 [A=352, D=32]. This fit fails to adequately capture the behavior at all latitudes. Instead, we fit for points with |b| > 25, which is shown as the green line in the left panel of Figure 2.6 [A=543, D=-204]. Seon et al. (2011a) find values of 847±96 and -457±100, for A and D respectively, shown in cyan. These differences are again likely due to GALEX avoidance of bright objects. At sin $|b|$ =1.0, the value of the FUV intensity will reduce to A+D, yielding a value for a minimum FUV intensity. For both fits, this number is a few hundred CU.

The two parameter fit, while relatively good for higher latitudes, raises the question about the physical interpretation of the value for D. The value of A should indicate the scale factor from extinction or dust column to scattering, while a positive value for D could be interpreted as an isotropic component which is unrelated to the scattering traced by the cosecant fit. If the isotropic component is already removed, or if D is negative, then there is no physical motivation for including this term. Further discussion of and modification to the cosecant fit is found in Section 2.4.

We show the result of removing an offset in the right plot in Figure 2.6. We use 300 CU as a low level intensity that is not related to Galactic components. Further discussion of this component is found in Sections 2.3.2 and 2.4. As noted above, a single parameter cosecant distribution will be horizontal. Instead, the actual data decrease with increasing sin|b|, indicating that the cosecant model doesn't provide a reasonable fit when a physically motivated isotropic offset is removed. The straight dashed line fit of the median (I_{FUV}-

300) sin|b| = 283 does not match the data at any latitude range. A single parameter fit yields A=312, similar to the median. Forcing a two parameter fit for |b| > 25 yields values of [A=648, D=-592] which provides a better match, but has no straightforward physical interpretation.

2.3.2 Relationship with other Galactic properties

The diffuse FUV intensity at high latitudes is determined by the distributions and intensities of both FUV emission from bright stars throughout the disk and the dust which scatters that emission. Here we investigate the relationship between FUV intensity and other Galactic quantities that trace dust and gas. In this section all sky maps of 100 μm emission, Hα intensity, and N_{HI} column density are each compared to the diffuse FUV data. While there are overall correlations, we also explore how scatter may provide information about the distribution and properties of the dust and illuminating sources. We note here that the resolution of the N_{HI} column density map is significantly lower than the other maps used. We expect this will increase the scatter in our correlation between FUV and N_{HI} column, but will not change the overall result.

Two dimensional histograms are plotted for FUV emission vs. each Galactic quantity in log-log space in Figure 2.7. All three graphs show strong correlation between the FUV intensity and the other measured quantities (correlation values calculated using the linear Pearson method are shown). All three quantities are well correlated with FUV emission, but include a large amount of scatter. The strongest correlation is between FUV emission and 100 μm intensity, with r=0.80. The correlation between FUV emission and N_{HI} is also quite

high, with r=0.78. The weakest correlation is between FUV emission and Hα intensity, with r=0.73.

In all three plots of Figure 2.7, we find a low level minimum FUV. The FUV intensity has a minimum at around a few hundred CU, flattening below 2 $\times 10^{20}$ cm^{-2} for N_{HI}, 1 MJy/sr for 100 μ, and 0.5 R for Hα. The plots of N_{HI} and 100 μm both also have a significant flattening of FUV intensity at large values. The FUV median remains constant above 10 $\times 10^{20}$ cm^{-2} for N_{HI} and 8 MJy/sr for 100 μ. The plot of FUV vs. Hα, however, continues to be linear at high values of both. Some flattening at large values of 100 μm and N_{HI} was also observed by Seon et al. (2011a) with SPEAR/FIMS data. The GALEX avoidance of bright regions of the sky could make this more pronounced in our data.

As noted above, any quantity which has a plane parallel distribution with respect to the Galactic plane will vary with latitude roughly as the cosecant of latitude. By removing the cosecant dependence, we can verify that deviations from a plane parallel distribution are also correlated between two different Galactic quantities. As such, we re-plot Figure 2.7 with a factor of sin|b|, shown in Figure 2.8. The correlation coefficient is again calculated using the linear Pearson method and are weaker after the cosecant correction. The scatter in all plots is increased compared to Figure 2.7. The correlation between 100 μm emission and diffuse FUV remains the strongest and is discussed further in Section 2.3.4. The correlation between Hα and diffuse FUV is still the weakest of the three, and we examine it in more detail in Section 2.3.5. As a simple plane parallel model only crudely represents the true 3-D distribution of any Galactic component (Witt & Petersohn 1994 and discussed above), it is not surprising that we find these weak correlations. A more detailed model is required

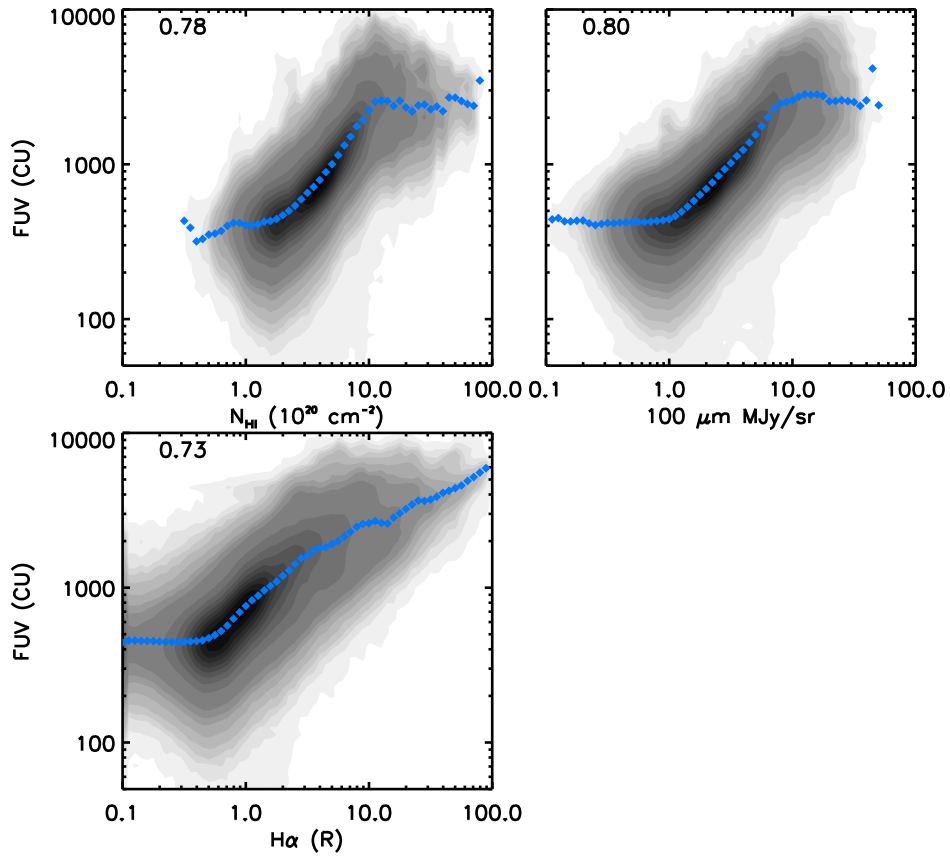

Figure 2.7 2-D histogram of FUV intensity vs. Galactic quantities in log-log space. Blue dots indicate the median value in abscissa bins of 0.05 dex. The linear Pearson correlation coefficient is shown in the upper left of each panel. **Top Left:** FUV intensity vs. N_{HI}. At low ($< 10^{20}$ cm^{-2}) and high values ($> 10^{21}$ cm^{-2}) of N_{HI}, the FUV intensity levels off. **Top Right:** FUV intensity vs. 100 μm emission. As with N_{HI}, the relationship is flat at low ($<$ 1 MJy/sr) and high ($>$ 8 MJy/sr) 100 μm intensity, with a linear relationship in between. **Bottom Left:** FUV intensity vs. Hα intensity. Unlike the previous two plots, the FUV intensity does not level off at high values of Hα intensity.

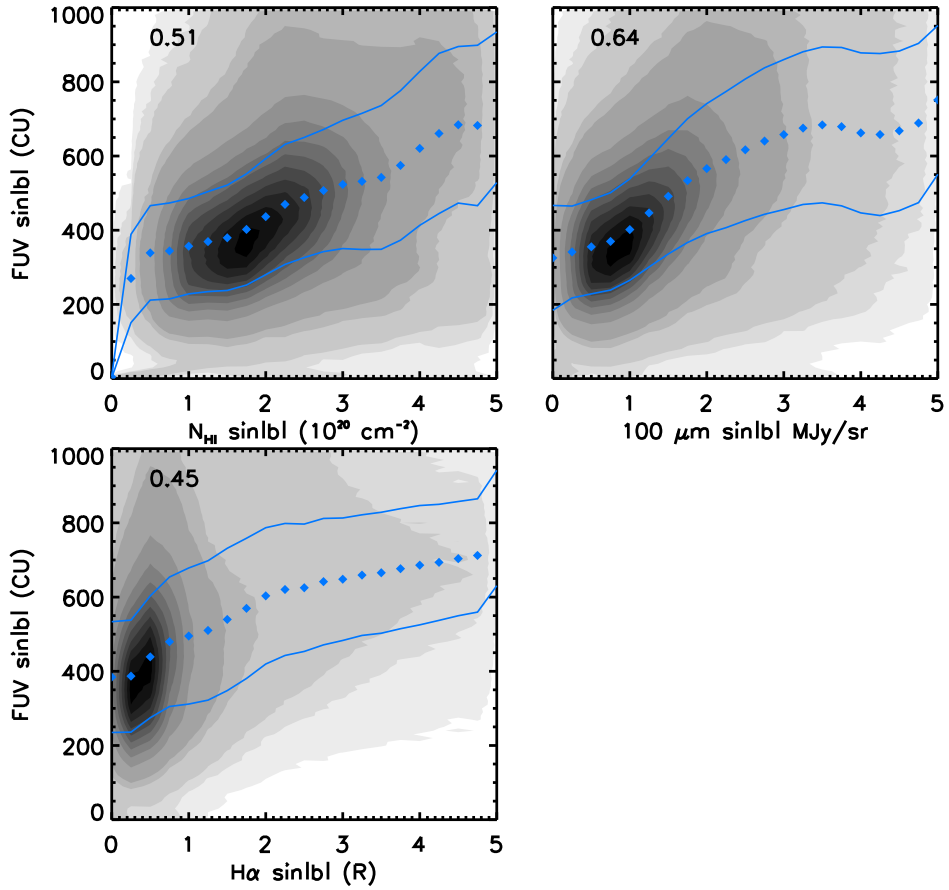

Figure 2.8 2-d histograms of FUV sin|b| vs. Galactic quantities times sin|b|. Blue dots indicate the median value for abscissa bins of 0.25, while blue lines indicate one standard deviation from the median. Linear Pearson correlation coefficients are shown in the upper left of each panel. **Top Left:** FUV sin|b| vs. N_{HI} sin|b|. **Top Right:** FUV sin|b| vs. 100 μm sin|b|. **Bottom Left:** FUV sin|b| vs. Hα sin|b|.

to fully interpret this result.

A comparison of the quantities is shown in Figure 2.9, to highlight behavior at low intensities where the relationship is primarily linear. Seon et al. (2011a) calculated best fit lines (in red) for b>25°, while our lines include data from all latitudes. The fits are similar for all but 100 μm. Restricting our data to b>25° yields a closer match in fit for FUV vs. 100 μm. Table 2.1 shows slopes and intercepts for the calculated best fit lines.

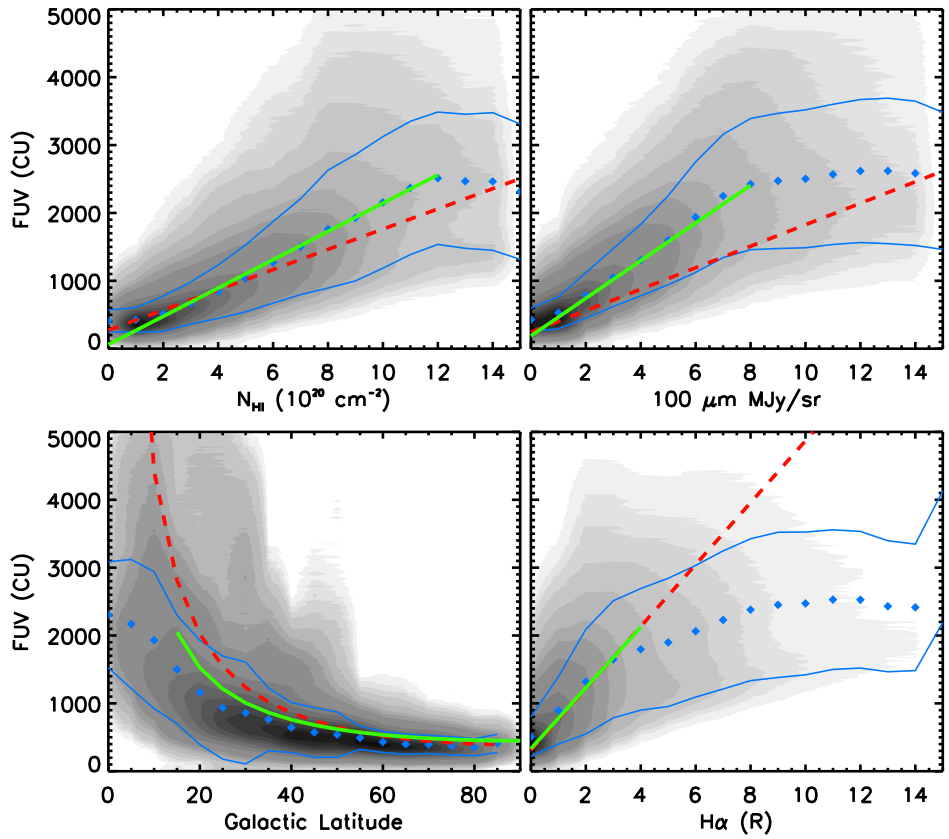

Figure 2.9 2-D histograms of FUV vs. Galactic quantities with a linear scale. Blue points indicate the median for abscissa bins of 1.0, while the blue lines indicate one standard deviation from the median. Green lines are best fit lines for the median. Red lines are best fits lines from Seon et al. (2011a). **Top Left** FUV vs. N_{HI}. The line fit is restricted to 0-1.2 $\times$ 10^{21} cm^{-2}, above which there appears to be a flattening off. **Top Right:** FUV vs. 100 μm. The line fit is restricted to 0-8 MJy/sr. **Bottom Left:** FUV vs. sin |b|. The fit to the median is a two parameter cosecant function, I=A/sin|b|+D for b $>$ 25°. Here A=457.9$\pm$248.7, D=-88.5$\pm$283.0. **Bottom Right:** FUV vs. Hα.

		all points	0-15°	15-30°	30-45°	45-60°	60-75°	75-90°
100 μm[a]	slope	275±95	253±68	250±53	168±43.9	100±33	62±18	82±67
	intercept	241±273	601±201	411±139	480±109	432±95	386±73	338±98
N_{HI}[b]	slope	184±50	223±50	123±39	121±30	88±18	68±21	6.3±33
	intercept	188±180	123±240	636±169	403±117	347±76	305±86	383±99
Hα[c]	slope	383±478	214±61	161±58	128±44	83±19	7±42	39±105
	intercept	519±859	1342±281	938±269	680±189	547±112	434±96	379±108

[a] < 8 MJy/sr for 100 μm
[b] $< 10^{21}$ cm^{-2} for N_{HI}
[c] < 4 R for all points only, < 10 R for all others, for Hα

Table 2.1 Best fit lines- slopes and intercepts

Because the correlation with dust (and other properties) is nearly linear at low intensities, it is conventional to use the fit to this relation to determine the value of the constant FUV offset, which presumably includes components that are not associated with dust-scattered light. Most analyses have assumed that this component is nearly isotropic and we do the same here. FUV vs 100 μm emission shows a pronounced flattening at low 100 μm values (< 1 MJy/sr, as seen in the log-log plot of Figure 2.7). Furthermore, there is a FUV offset in the plots in Figure 2.9, at zero values of the abscissa. This minimum appears to be 200-300 CU. This offset has also been noted as a positive offset at N_{HI}=0 cm^{-2} of 200-300 CU by Martin et al. (1991), who suggest that it may be partially due to an undetected dust component. These offsets have been discussed in other works as a combination of a low level extragalactic FUV background (a few tens of CU, Paresce 1990; Schiminovich et al. 2001), incomplete bright object masking and airglow contamination. In this work, we have used 300 CU as the offset and revisit this component in Section 2.4.

In the top right panel of Figure 2.9, we note the break in the FUV intensity at 100 μm > 8 MJy/sr, with a median FUV intensity of 2400 CU. This saturation in the FUV intensity has been noted previously (Seon et al. 2011a; Witt et al. 2008), and appears to

occur for lines of sight having an optical depth high enough to both self-shield emission from within the cloud and block scattered FUV intensity from behind the cloud, decreasing the overall FUV intensity from that region. At high 100 μm we also observe a large scatter in FUV intensity. Along some sightlines, the presence of nearby FUV bright stars can enhance the overall FUV intensity above that predicted under the assumption of a uniform radiation field. A more detailed analysis of UV self-shielding and illumination of these sightlines is discussed in a forthcoming paper.

We find a similar break in the correlation of FUV vs. N_{HI} at $N_{HI} \sim 12 \times 10^{21}$ cm^{-2}. There is a break in the plot of FUV intensity vs. Hα intensity at 4 R, although this is a more gradual transition than for the other two quantities. In all plots, there is increased scatter as the abscissa values increase. The plot of FUV vs. Galactic latitude shows this occurs primarily at the lowest latitudes. Cutting out intensity from points with $|b| < 25^\circ$ decreases this scatter.

2.3.3 Correlations vs. Galactic latitude

We have already noted above that a difficulty in comparing our results to that of previous work is that derived correlations will depend on the Galactic footprint of the data used, and in particular the range in latitude. In order to understand the magnitude and physical origin of these effects, it is useful to divide our large data set into Galactic latitude cuts. In doing so, we note that regions of high scatter are generally confined to the lowest latitudes, while the FUV emission adheres to a linear fit at higher latitudes.

Figure 2.10 shows contour plots of FUV vs. 100 μm for latitude bins of 15°, combining

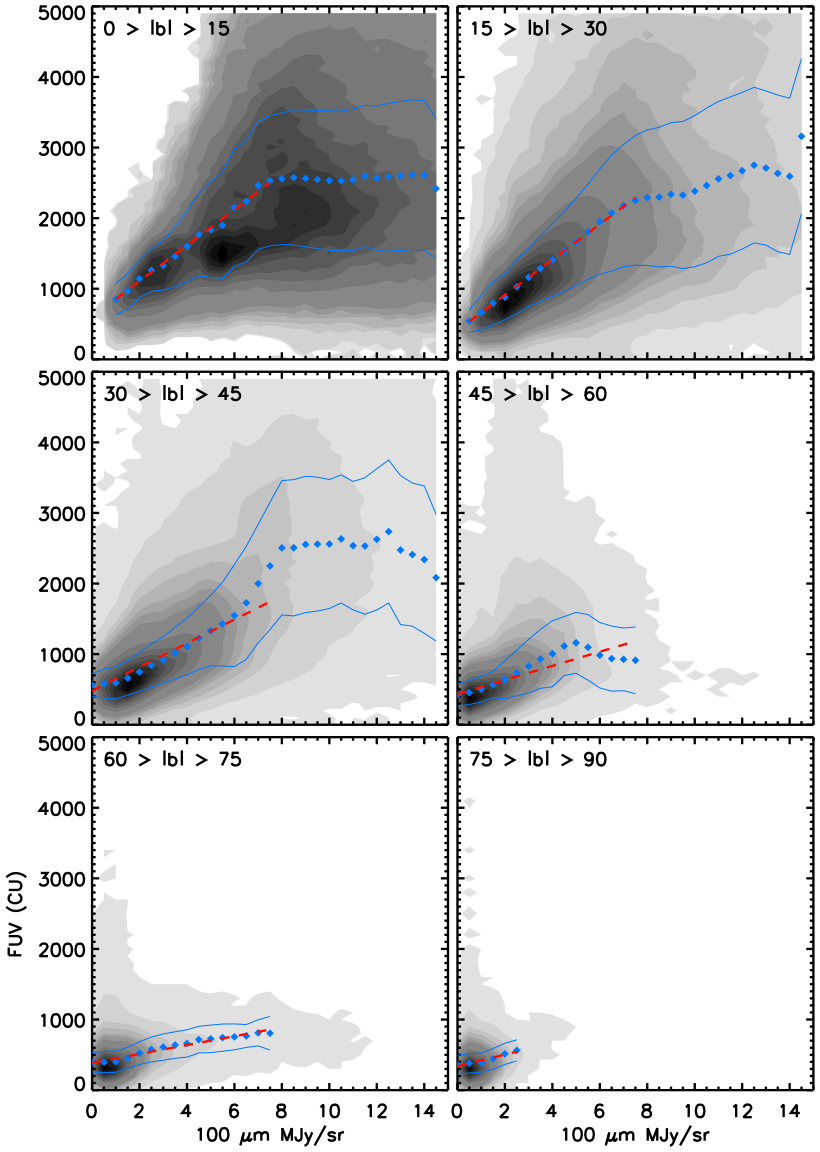

Figure 2.10 2-D histograms of FUV intensity vs. 100 μm emission for latitude cuts of 15°, N and S combined. Blue dots are the median for bins of 0.5 MJy/sr, with blue lines indicating one standard deviation. The red line is the best fit line to the median below 8 MJy/sr. At low latitudes, there is significant scatter in the relationship, due to both FUV bright stars and obscuring dust. There is a turnover in FUV intensity at ∼8 MJy/sr, above which the median FUV value remains constant. The slope of the linear relationship decreases systematically with increasing latitude, becoming smaller at the highest latitude cut.

the northern and southern hemispheres. Above 8 MJy/sr in latitude bins from 0-15° and from 30-45°, there is a flattening in the FUV profile, with the median constant at around 2500 CU. This flattening is not as clear in the latitude cut from 15-30°, but this is likely due to very high FUV emission around the Ophiuchus and Orion OB associations.

At high latitudes |b| > 45°, few points have 100 μm values above 8 MJy/sr, leaving the low intensity linear relationship. The slope of the linear portion does appear to change with latitude, with the low latitude cuts having a larger slope than at higher latitudes. Line fits below 8 MJy/sr are plotted in red, with fits as in Table 2.1.

Some of the scatter from the linear relation can be directly traced to specific objects or regions in the Galaxy. For example, in the latitude cut 45-60° there is a region of low 100 μm, but very high FUV (> 2500 CU), which stands out compared to the rest of the high latitude region. This appears to come primarily from the region directly around Spica (α Vir, at $l = 316°$, $b = 51°$, Park et al. 2012), which is a spectroscopic binary with two B type stars. The FUV intensity here is high, while the dust emission is more consistent with the rest of the latitude. This area also appears in Figures 2.11 and 2.12, at similarly low values for the abscissa.

At very high latitudes, where there appears to be only a weak relationship between dust and FUV intensity, increased relative scatter may be masking any correlation. This is reflected in the Pearson r value for the fits which is generally observed to decrease with latitude. For example, while the overall correlation between FUV and 100 μm is quite high (r = .80 for all points in log-log space, r = .64 after removing the cosecant dependence), at high latitudes, the linear Pearson r value drops to 0.14 (for |b| > 75°, with or without the

cosecant dependence). The FUV intensity in these regions is quite low, and the scatter is relatively large enough to give the appearance of high latitude FUV intensity that is only weakly sensitive to the 100 μm emission.

Figure 2.11 shows contour plots of FUV vs. N_{HI} column for |b| cuts of 15°. As with Figure 2.10, there is a flattening of the FUV emission at high values of N_{HI}. This appears to occur at 12 $\times 10^{20}$ cm^{-2}, which is consistent with the behavior found by Hurwitz et al. (1991). Low column at high latitudes means that this flattening column density is not reached above |b| = 45°. As with Figure 2.10, the slope of the linear portion changes between latitude cuts. Line fits below 10 $\times 10^{20}$ cm^{-2} are plotted in red, with fits as in Table 2.1.

Figure 2.12 shows contour plots of FUV vs. Hα intensity for |b| cuts of 15°. Here, there is much more scatter than with 100 μm or N_{H1}. We also observe variation in the Hα intensity where FUV plateaus. In the low latitude cuts, the turnover appears at 8-10 R, while at mid latitudes (30< |b| <60), there is little evidence for a turnover even above these Hα values. At the highest latitudes (|b| > 60) the relationship is nearly flat. Line fits below 10 R are plotted in red, with fits as in Table 2.1. Along with the high FUV intensity region around Spica mentioned above, there is a region of high FUV intensity at latitudes between 30-60°. These can be traced to the region directly above the Ophiuchus association (l=355°, b=18°). This region has significantly more scattered FUV than Hα. The Spica and Ophiuchus regions cause a bump in the median FUV value between 1-4 R. A more detailed discussion of FUV vs. Hα is found in Section 2.3.5.

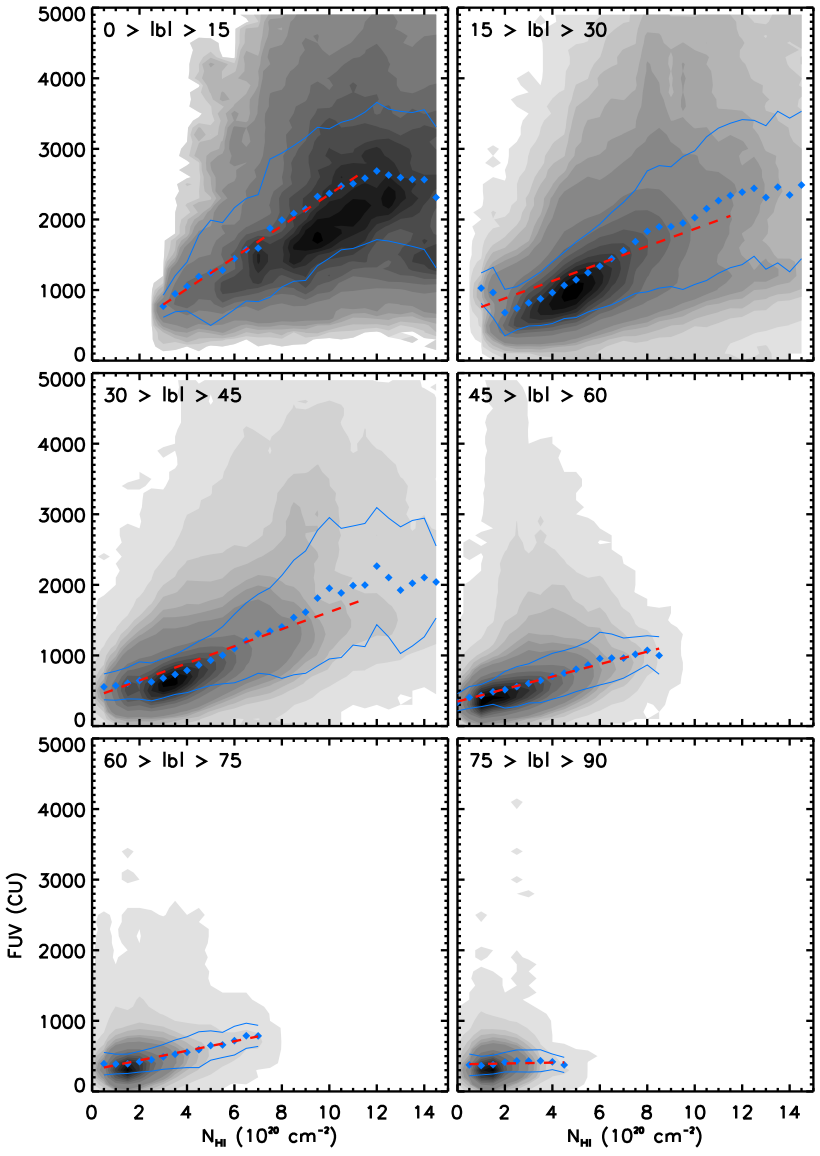

Figure 2.11 2-D histogram of FUV intensity vs. N_{HI} column. Blue and red lines as in Figure 2.10. There is a turnover in FUV intensity at $\sim 10^{21}$ cm^{-2}.

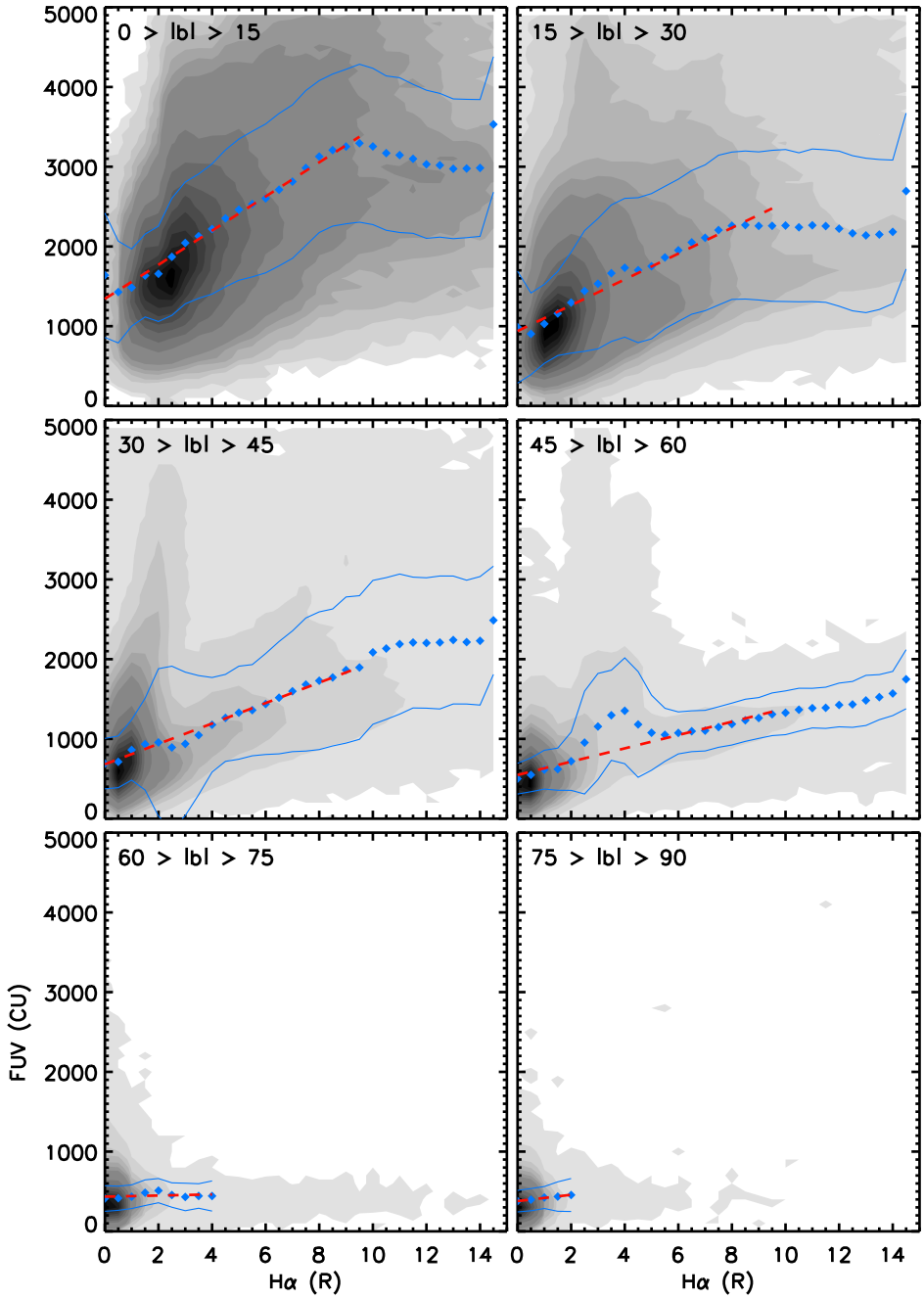

Figure 2.12 FUV intensity vs. Hα intensity. Blue and red lines as in Figure 2.10.

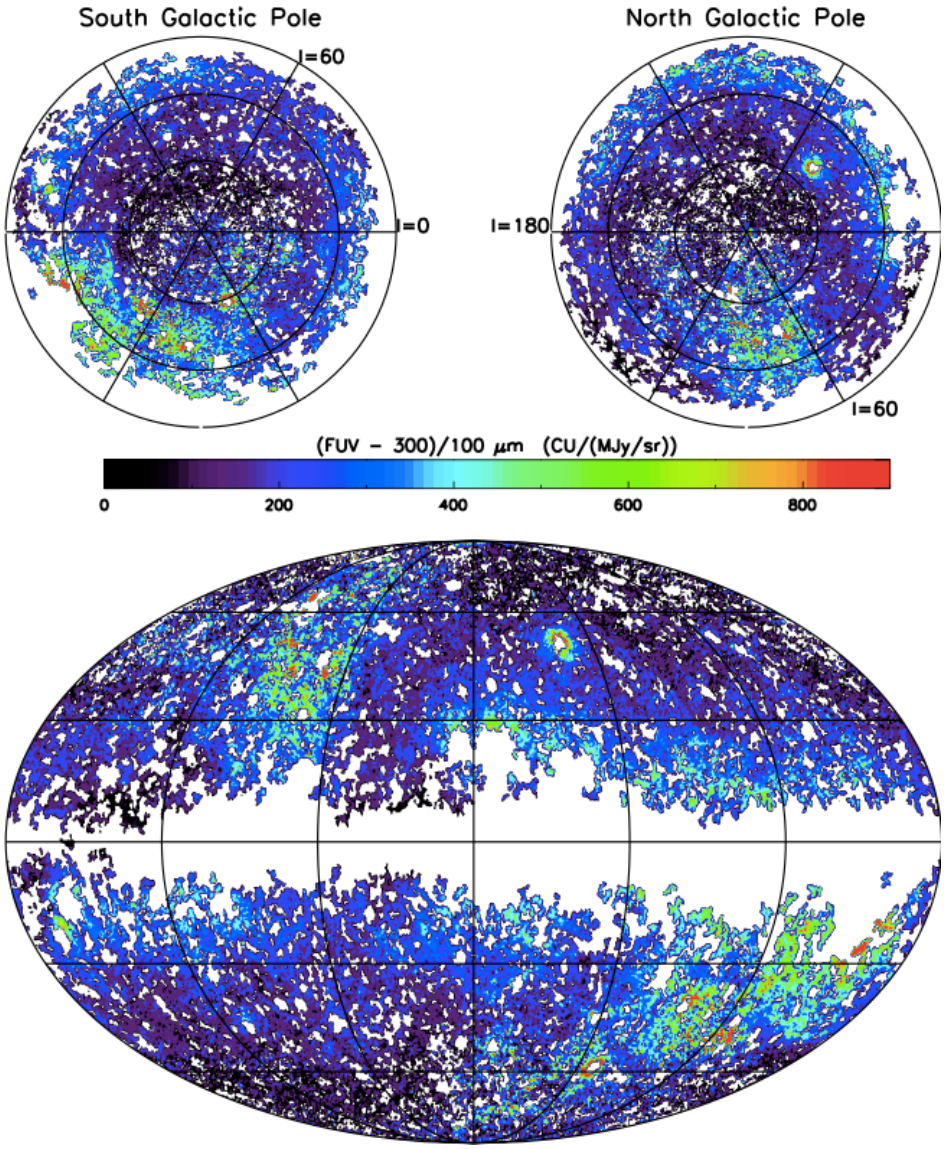

Figure 2.13 FUV/100 μm ratio (CU/(MJy/sr)) for the whole sky. The FUV offset of 300 CU has been removed for these plots. Notable high slope regions are around OB associations, e.g. Ophiuchus, and brights stars, e.g. the spectroscopic binary Spica (at l=316, b=51., Park et al. (2012)).

2.3.4 FUV vs. 100 μm

The relationship between diffuse FUV intensity and 100 μm emission is often expressed as a slope with units of CU/(MJy/sr). Previous work shows a wide range of slopes. Perault et al. (1991) measured 244 CU/(MJy/sr) in the northern hemisphere and 214 CU/(MJy/sr) in the southern hemisphere, using data from the ELZ spectrophotometer on DB2-AURA. Hurwitz et al. (1991) found ∼294 CU/(MJy/sr) using data from the Berkeley spectrometer on UVX. Wright (1992) obtained 203 CU/(MJy/sr), using data from Fix et al. (1989). Haikala et al. (1995) used FAUST data to observe Galactic cirrus near the north Galactic pole, finding 128 CU/(MJy/sr). Sasseen & Deharveng (1996) found a range of slopes from -49 to 255 CU/(MJy/sr) in 13 regions using data from FAUST. Sujatha et al. (2010) find slopes between 50 and 480 CU/(MJy/sr) using data from GALEX of part of the Draco Nebula. Murthy et al. (2010) find an average slope of 302 CU/(MJy/sr) using smoothed GALEX data from the whole sky. Seon et al. (2011a) find a slope of 158 CU/(MJy/sr) from SPEAR data. In our all sky GALEX data, we find an average slope of 280 CU/(MJy/sr).

Clearly, the behavior of FUV intensity and 100 μm emission can vary significantly from region to region, and even within the same cloud complex. We show a contour plot of ratios (FUV/IR) for the whole sky in Figure 2.13. The isotropic diffuse FUV offset of 300 CU is removed. There are two large regions with high ratios, one in the northern hemisphere above $b > 30^\circ$ between $l = 60^\circ$ to $l = 180^\circ$ and one in the southern hemisphere below $b < -45^\circ$ between $l = 240^\circ$ to $l = 0^\circ$. These features correspond to regions of particularly low IR emission, with 100 μ m intensity of less than 1 MJy/sr, and often lower than 0.5 MJy/sr. In their original dust map, Schlegel et al. (1998) note these extremely low emission windows as good regions

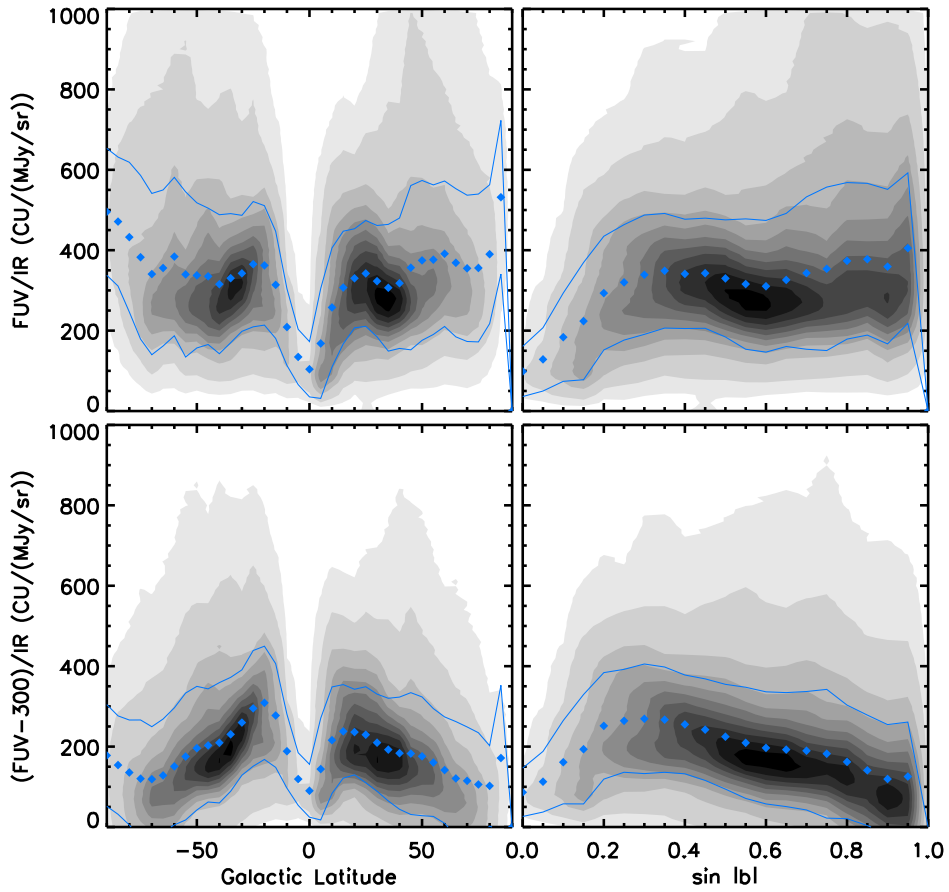

Figure 2.14 2-D histograms of FUV/IR (CU/(MJy/sr) vs. Galactic coordinates. Blue dots indicate the median for bins of 5°, with blue lines indicating the standard deviation from the median. **Top Left:** FUV/IR ratio vs. Galactic latitude. **Top Right:** The same data as in the top left plot, but plotted vs. sin|b|. **Bottom Left:** Same as above, but with the 300 CU offset removed from the FUV data. **Bottom Right:** Same as above, but with the 300 CU offset removed from the FUV data. The declining slope above sin|b| = .4 and the decrease in FUV/IR ratio with increasing latitude both suggest a deviation from a simple plane parallel distribution.

for observations requiring minimum dust contamination.

Very low ratios (< 100 CU/(MJy/sr)) are found near the Galactic plane, reflecting the high dust content in these regions. There are some low latitude areas with high ratios from excess FUV intensity due to proximity of nearby OB associations, particularly Orion (l=200°), the Gum nebula (l=260°,b=-2°), and Ophiuchus(l=355°, b=18°).

In Figure 2.14, showing the FUV/IR ratio vs. Galactic latitude, the ratio is nearly constant. With the 300 CU offset removed, as in the bottom panels, the ratio begins to decline at latitudes above |b|=30°, the same behavior as the slopes in Figure 2.10. This is likely driven by decreasing FUV intensity at high latitudes. In both panels, there is significant scatter at all latitudes.

The origin of this scatter becomes more clear in Figure 2.15, which shows the ratio of FUV/IR vs. Galactic longitude for different latitude cuts. The high ratio regions centered around l=90° in the northern hemisphere and at b < -45°, 350 < l < 250° in the southern hemisphere, are the same regions that have been noted previously. Otherwise, elevated ratios at low latitudes indicate higher than expected FUV intensity. In particular, the Orion OB complex, the Gum nebula, and regions in between have excess FUV intensity, concentrated in the Galactic plane. There is little leakage of this to higher latitudes, as evidenced by the general flat profile in the top two panels of Figure 2.15. High slopes in the southern hemisphere below this region could point to leakage of FUV photons, but that may also be the result of the low IR emission region discussed above. The region of high slopes near b> 45° at l=310° is again due to excess FUV intensity from Spica.

2.3.5 FUV vs. Hα

The relationship between diffuse FUV intensity and diffuse Hα intensity has not been as well studied as other Galactic quantities. For high latitude Hα intensity in particular (tracing the diffuse warm ionized medium, WIM), the common assumption was that most Galactic Hα originated in ionized HII regions, with significant leakage of Lyman continuum photons

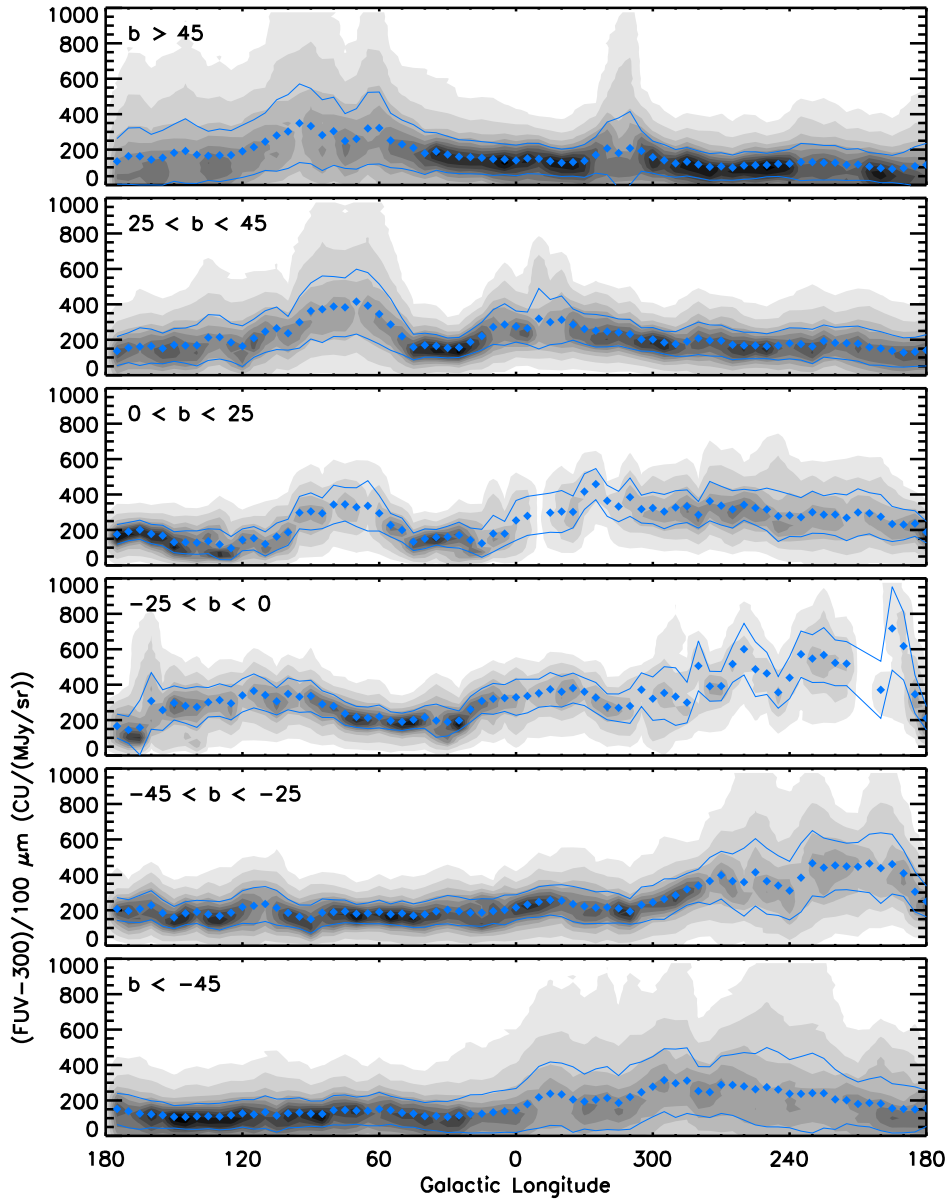

Figure 2.15 All plots show 2-D histograms of FUV/IR (CU/(MJy/sr)) vs. longitude for latitude cuts as indicated, with the 300 CU offset removed from the FUV data. Blue dots indicate the median for bins of 5° with blue lines indicating one standard deviation. These plots show both the median slope, 280 CU/(MJy/sr), but also the large regional variations. Some variations are spatially coherent, as evidenced by high slopes at northern latitudes around l=60° and southern latitudes around l=260°.

responsible for the Hα intensity observed elsewhere, although the mechanism to provide the necessary leakage was not well explained (Reynolds et al. 1995; Haffner et al. 2009). Recent work by Witt et al. (2010), Seon et al. (2011b), and Dong & Draine (2011) have argued that a significant percent of Hα intensity observed outside of HII regions is in fact dust scattered, and can be shown to correlate with the diffuse FUV intensity.

Scattering percentages for Hα in the WIM have been calculated to be as low as 5-20% (Wood & Reynolds 1999), 20% (Dong & Draine 2011), and as high as 37% (Seon et al. 2011b), using varied techniques. Brandt & Draine (2012) have recently measured the visible spectrum of diffuse Galactic light, and in so doing find that scattering accounts for around 19% $\pm$ 4% of Hα intensity, for $|b| > 60^{\circ}$.

As shown in Figures 2.8 and 2.7, there is a correlation between the diffuse FUV and Hα intensity, although it is not as tightly correlated as 100 μm and N_{H1}, with r=0.73 (log-log) overall and r=0.45 after the latitude dependence is removed. Still, this indicates that there is some shared dependence between FUV and Hα as discussed above. Our data set mainly encompasses the diffuse WIM due to the avoidance of the Galactic plane and bright regions.

Figure 2.16 shows an all-sky map of Hα/FUV in units of R/10^3 CU, following Seon et al. (2011b). An offset of 300 CU has been subtracted from the FUV data. There is clear structure, including especially high ratios around the Gum Nebula and Orion complex. These are all likely due to high Hα intensity from HII regions. Other OB associations, including Ophiuchus and structures from l=0 to 180°, do not have the same high ratios, despite similar FUV emission values. Finally, there are high ratios at both poles, primarily driven by low FUV intensity than high Hα. Outside of these regions, at mid-latitudes, there

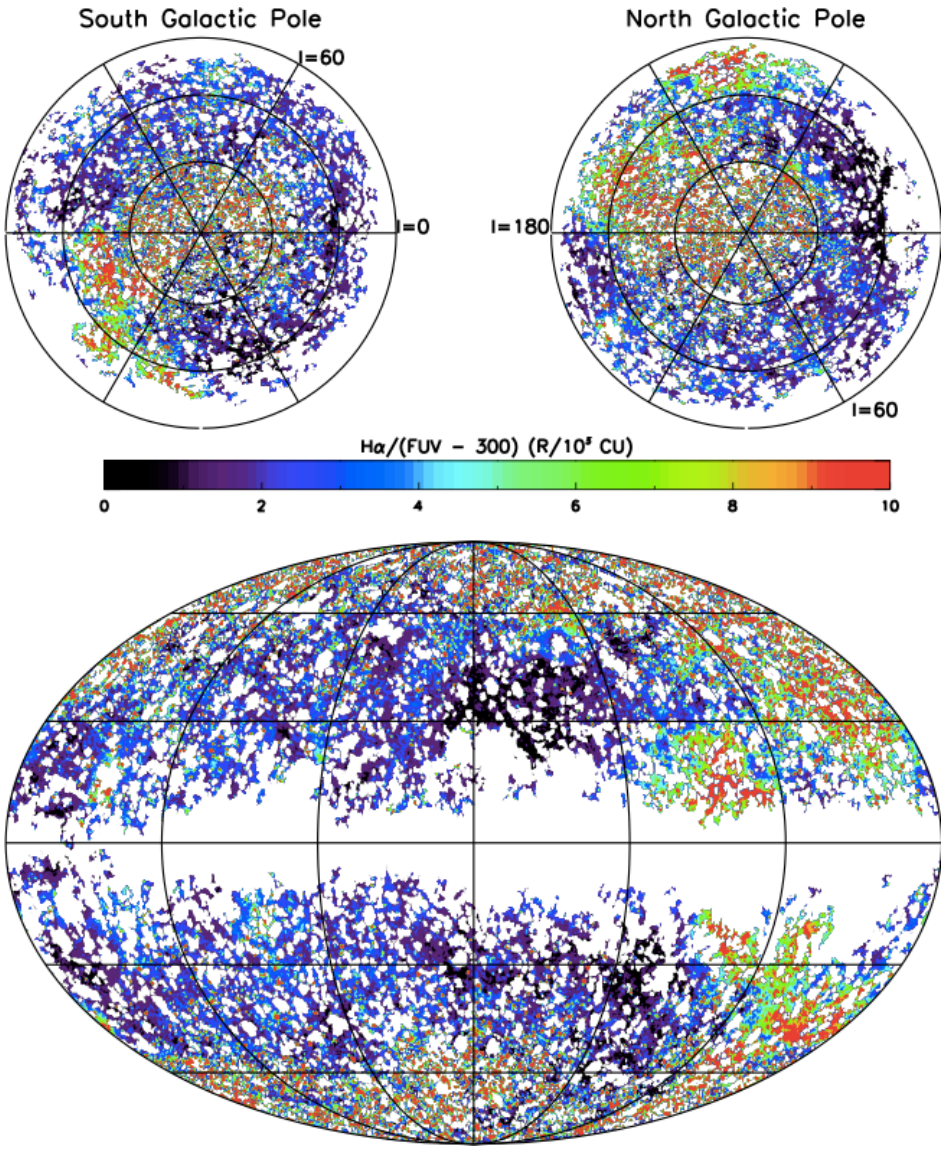

Figure 2.16 All-sky map of Hα/FUV, in units of R/10^3 CU. A 300 CU offset for the FUV map has been removed.

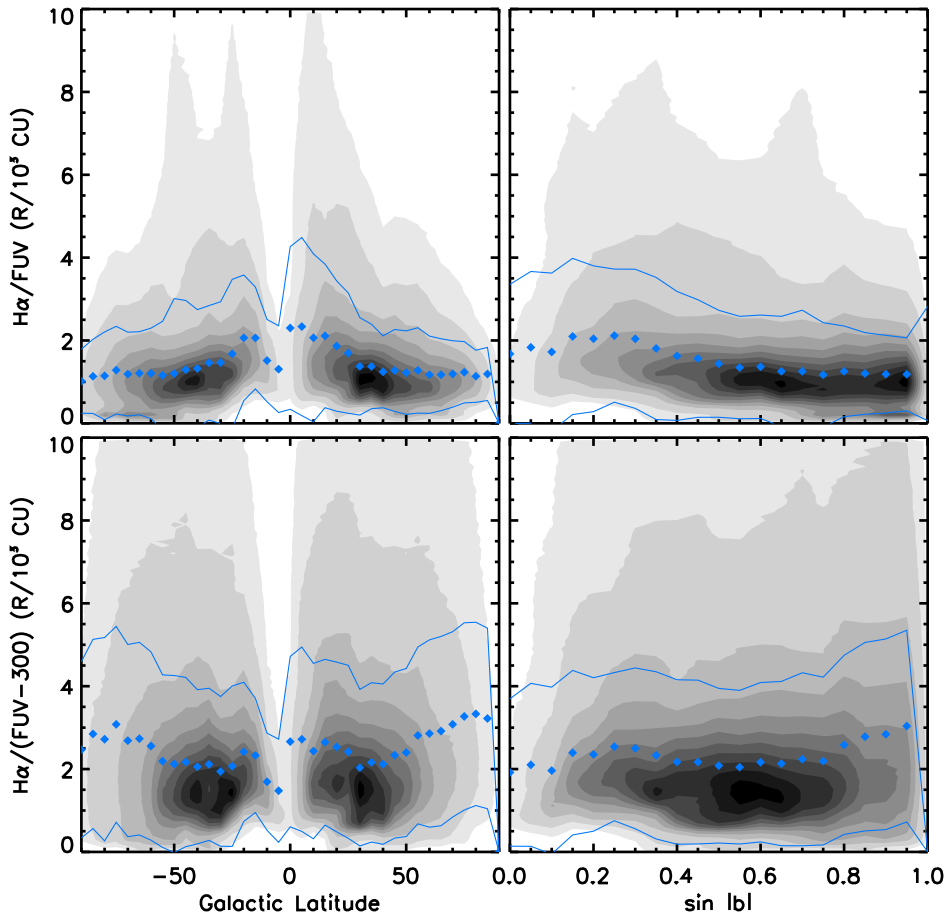

Figure 2.17 2-D histograms of Hα/FUV (R/10^3 CU) vs. Galactic coordinates. Blue dots indicate the median for latitude bins of 5° with blue lines indicating one standard deviation. **Top Left:** A 2-d histogram of Hα/FUV vs. Galactic latitude. **Top Right:** The same data plotted vs. sin|b|. **Bottom Left:** Same as above, but with a 300 CU offset removed from the FUV data. **Bottom Right:** Same as above, but with a 300 CU offset removed from the FUV data.

.

is a relatively stable ratio of 2-3 R/10^3 CU.

Figure 2.17 shows the ratio of Hα/FUV as a function of latitude. The higher ratios at low latitudes are the result of bright HII regions, but in general the ratio is nearly constant. Unlike for FUV/100 μm (Figure 2.14), the plot of Hα/FUV vs. Galactic latitude doesn't appear significantly changed by the removal of the FUV offset. Potentially this is because the

Hα intensity is the result of a wide range of processes, not just scattering, so the correlation is low to begin with (as noted in Figure 2.8). The range of ratios becomes larger at high latitudes, but the median remains roughly constant below sin|b|=0.8, and rises slightly after.

Figure 2.18 shows the ratio of Hα/FUV as a function of Galactic longitude for different latitude cuts, with the 300 CU FUV offset removed. Like its counterpart for 100 μm emission Figure 2.15, the ratio varies by an order of magnitude across the sky. At the highest latitude cuts, the standard deviation is 2 R/10^3 CU, but the mean is relatively stable with longitude. At latitudes closer to the Galactic plane, the standard deviation decreases, but the variation in ratio can be more than a factor of 2 between different longitudes. Some of this variation is seen in multiple latitude cuts, with high Hα/FUV ratios appearing in the same longitude range. Of particular note is the peak at l=200°, potentially associated with the Orion OB association, which appears at all latitude cuts. This peak is the result of high Hα intensity and recalls a similarly placed peak in Figure 2.15. In some cases, excess Hα intensity may be caused by significant Lyman continuum photon leakage into high latitudes. This may be related to the broad features of Hα excess found near the Gum nebula and Orion.

2.4 Discussion

The dust content of the Galaxy provides a common origin for both the diffuse FUV and 100 μm emission. Cold dust emits at IR wavelengths and efficiently scatters FUV starlight. In general, these two quantities vary proportionately. Here we consider two different simplified models of the observed FUV intensity. The first assumes that it can be modeled as a linear function of 100 μm emission. A second refined model fits FUV as a function of Galactic

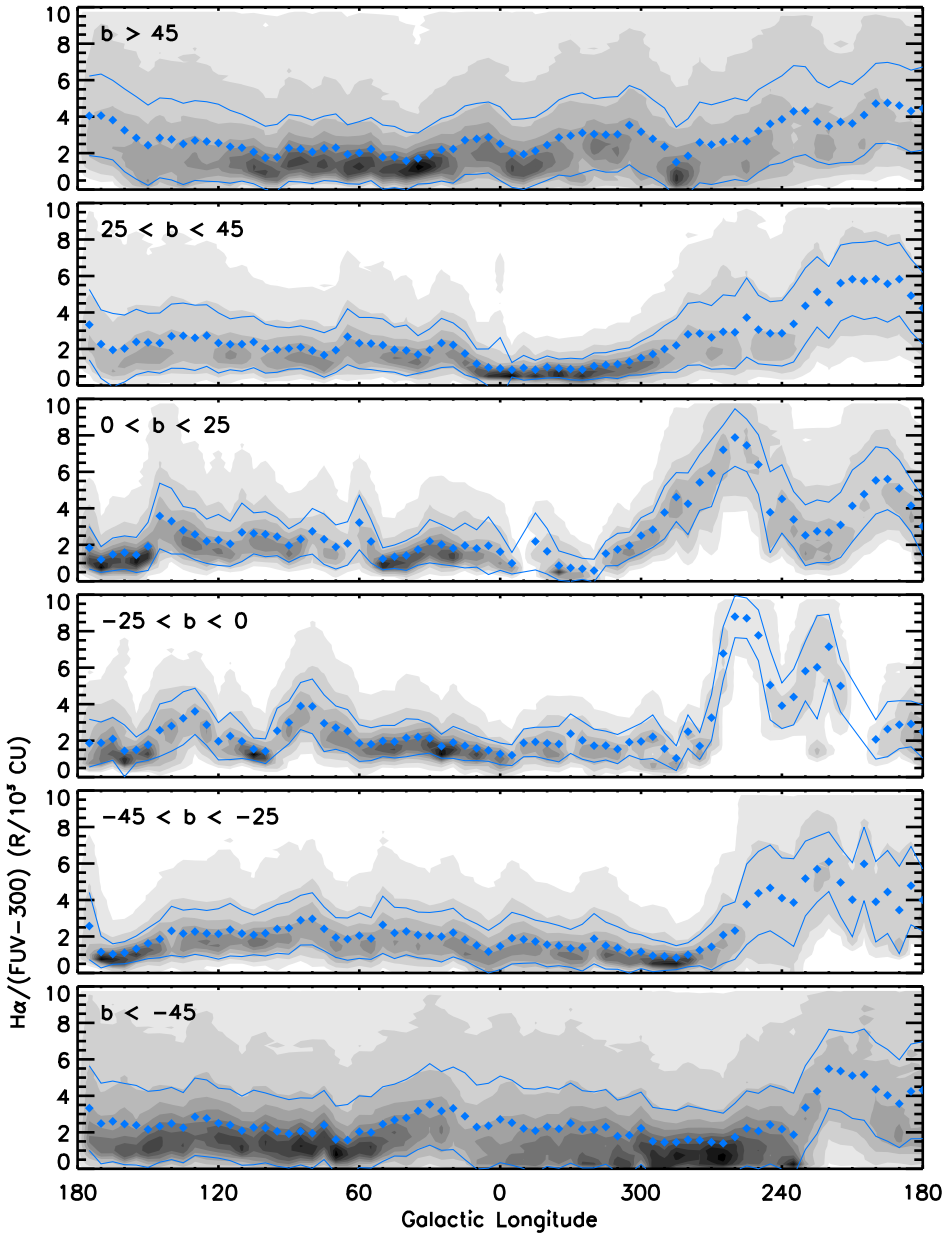

Figure 2.18 All plots show 2-D histograms of Hα/FUV (R/10^3 CU) vs. longitude for latitude cuts as indicated, with the 300 CU offset removed from the FUV data. Blue dots indicate the median for longitude bins of 5° while blue lines indicate one standard deviation. These plots show both the low level average slope (2-4 R/10^3 CU), but also the large regional variations. Some variations are spatially coherent, as evidenced by high slopes at southern latitudes around l=260° and 200°.

latitude, albedo, and scattering asymmetry, using a modified cosecant fit to overcome the deficiencies described in Section 2.3.1.

2.4.1 Linear fit between FUV and 100 μm

Linearity between FUV intensity and 100 μm emission is found for points with 100 μm emission less than $\sim$8 MJy/sr. Line fits and other evidence discussed in Section 2.3.2 also indicate a FUV offset at the 100 μm zero-point. These two values, the slope and offset, of the linear fit between FUV intensity and 100 μm emission are discussed in further detail.

2.4.1.1 FUV offset

An FUV offset in the linear relationship with other tracers of the cold Galactic ISM has been observed previously, and in our work appears to be $\sim$300 CU. This offset is assumed to result from a local source of diffuse isotropic background, an extragalactic background or an isotropic Galactic source not yet considered. As discussed above in Section 2, some contribution may also come from incomplete masking of known resolved objects.

As the FUV background shows low-level variability over the course of an orbital night, some contribution is likely to originate from OI (1356Å, 1304Å) airglow and/or geocoronal Ly α (1216Å) lines, which have night-sky intensities of 1.0, 10 and 3000 R respectively. OI 1356Å falls within the FUV bandpass (at 35% peak efficiency) resulting in a count rate at the detector corresponding to a $\sim$150 CU FUV continuum background. GALEX included a blue edge filter which is expected to attenuate the contribution from OI 1304Å and Lyα below these levels. During orbital night we observe a variation in the background intensity of $\pm$50

CU. Observations of an identical target throughout the year show a similar 50 CU scatter, presumably due to seasonal variation in orbit geometry and airglow intensity. Murthy (2014) also calculated the expected contribution to the GALEX FUV channel from airglow as a function of both time from local midnight and angle between the Sun and the observed target. From this work, airglow was estimated to be 200 CU ± 100 CU at local midnight, comparable to our assessment, with a similar variation vs. local midnight. As the low level of variation is not likely to impact our analysis, we have left more detailed modelling (and subtraction) of the variable airglow component to a subsequent paper. The contribution due to Zodiacal light is sufficiently low for the FUV band that we do not attempt to remove it (Leinert et al. 1998). Inspection of FUV intensity vs. ecliptic latitude shows no evidence for zodiacal contamination.

Another possible source of low level intensity is unresolved or incompletely masked FUV objects. There are at least three potential contributors here: 1) unmasked scattered light or ghosts from bright stars; 2) any unresolved and/or undetected light from faint stars or extragalactic objects that have not been masked and 3) unmasked light from the other masked objects in the field. The GALEX pipeline mask, which is used to remove bright objects (see Section 2.2.1) could potentially have missed faint stars. Furthermore unmasked reflections and ghosts around bright stars are visible in the data. These can contribute to the overall scatter, aside from any contribution to the offset. In general GALEX avoided observing bright stars with m_{FUV} ∼9.5 with a flux producing a local count rate exceeding 5,000 counts per second. If we conservatively assume that 1% of the light from the brightest observable star filled an 11 square arcminute pixel then we would anticipate

a diffuse contribution of <6000 CU at that location on the sky. The source density of stars just below the avoidance limit (e.g., with 9.5< m_{FUV} <12) is low, much less than 1 per square degree over the AIS region, suggesting that fewer than 0.1% of all pixels may be contaminated by unmasked bright starlight. Additionally, our object detection software treats most bright stars as extended sources, creating a larger masked area than for fainter unresolved objects.

Extragalactic diffuse FUV intensity is believed to contribute only a few tens to 100 CU. Xu et al. (2005) calculated the contribution to the GALEX data from both resolved and unresolved galaxies to be 1.03 ±0.15 nW m^{-2} sr^{-1}, or about 51.5 ±7.5 CU. Voyer et al. (2011) find that the integrated light from field galaxies contribute flux at the level of 65-82 CU to the extragalactic background. Seon et al. (2011a), also calculated that the cumulative effect of unmasked unresolved FUV stars and galaxies is probably not significant. These same results suggest that unmasked light from the objects below the AIS detection limit will be negligible.

Additional components could come from other sources of FUV intensity, including molecular hydrogen fluorescence and line emission such as C IV. It seems unlikely that there is enough evenly distributed molecular hydrogen at these high latitudes to contribute significantly to the continuum offset. Ryu et al. (2006) and Ryu et al. (2008) report band-averaged $I(H_2)/I_{cont}$ ratios of ∼0.15 in molecular-rich star-forming; the ratios in diffuse gas is likely to be lower (e.g. Martin et al. 1990; Lee et al. 2006, 2008). Ryu et al. (2008) also suggest that the band-averaged contribution from C IV is even lower. As significant concentrations of molecular gas are present closer to the disk, H_2 fluorescence may contribute to

the large scatter for |b| <25°.

A last concern is whether a possible systematic zero-point offset exists in the comparison data sets. We can investigate this possibility by comparing the relationship between different tracers of the Galactic ISM, provided that they are uncorrelated. More recent data sets, such as the Planck map of cold Galactic dust, could provide new measures of the lowest dust column densities. However a preliminary inspection of the 2013 Planck data indicates the low dust regions are still present at the levels observed previously (Planck Collaboration et al. 2013). The offset calculated using these data did not change.

Hα provides a different view of the ISM which is indeed suggested in the correlations we observe. The presence of HII regions will introduce additional scatter, and the intercepts of the fits in these regions are typically a few hundred CU above the value used here. However, at high latitudes where star-forming regions are not present, the offset decreases to ∼400 CU, similar to the offset obtained using other Galactic quantities.

2.4.1.2 FUV-IR Slope

With the offset removed, the slope of the FUV vs. 100 μm relation is variable across the sky, as seen in Figures 2.13 and 2.14. There are two regimes in the behavior of the FUV. In the optically thin regime, typically where 100 μm is less than 8 MJy/sr, the FUV and 100 μm are correlated. In the optically thick regime, FUV saturates and the correlation disappears. In the discussion below we only refer to the optically thin regime. At mid and high latitudes there are very few regions that deviate from a linear relationship, due to an absence of optically thick dust.

A very simple model, assuming isotropic scattering, an average cosecant dust column relation and a constant scale height, predicts a uniform relation between 100 μm and FUV across the sky. Instead, the slope declines with increasing latitudes. This change in slope for optically thin clouds between mid and high latitudes indicates that a simple scattering picture may not be valid. The emission at 100 μm decreases at high latitudes, following the csc|b| relation, with the simple model suggesting that the FUV intensity should decrease proportionally. Our results show that the FUV intensity is decreasing faster than expected, leading to a smaller typical value for the slope at high latitudes.

2.4.2 Modified cosecant fit and scattering properties

The changing slope between FUV intensity and 100 μm emission at high latitudes is related to the deviations from a cosecant dependence (Figure 2.6). As discussed in Section 2.3.1, a function of the form I=A/sin|b| for FUV intensity with the offset removed is not able to fully describe the observed intensity. Adding an extra term to the function, making it I=A/sin|b|+D, yields better fits for $|b| > 25^\circ$ (see also Seon et al. 2011a). But under the assumption that all isotropic components have been accounted for and removed, there is no physical basis for the inclusion of the constant D.

The simple cosecant fit does not include parameters for non-isotropic dust scattering, instead assuming that the dust scattering scale factor was constant with latitude. Jura (1979) proposed that the surface brightness of a cloud at various latitudes is a function not just of the ISRF, but also of the scattering function for the dust, assuming all illumination originates in the plane. With the inclusion of optical depth by Wright (1992), the dust

scattered intensity, S, can be expressed as:

$$S = S_o \tau a (1 - 1.1 g \sqrt{sin|b|}) \tag{2.5}$$

This approximation is valid for |b| > 10°, g < .85, and optical depths of less than 1 where S_o is the peak scattered ISRF. To calculate optical depth, we used E(B-V) values from Schlegel et al. (1998), and a standard optical depth calculation:

$$\tau = \frac{R_\lambda}{1.086} \times E(B-V) \tag{2.6}$$

We then use Equation 2.5 and fit for values of a, g, and S_o. We compare predicted intensity to FUV intensity (with 300 CU offset removed), and find the best fit values are 0.62 ± 0.04 and 0.78 ± 0.05, for a and g respectively, with S_o =6260 ± 400 CU for sin|b| > 0.3, or |b| > 20°. Here, a non-linear least squares fit was applied to the median of FUV intensity in bins of |b| = 1.0 degree. There is some degeneracy between the choice of peak intensity S_o and albedo a. The albedo value we predict is related in part to the selection of S_o. Larger values of S_o allow for a smaller a. If we force S_o = 5000, the best fit model predicts an albedo of .75 ± 0.04, while g remains unchanged. The value of S_o in the best fit model is similar to the 5800 CU scaling used by Hurwitz et al. (1991). An overlay of the fit on the data is shown in Figure 2.19.

As with the cosecant fit, this modified fit is not valid at low latitudes. The best fit we find is similar to the two part cosecant fit described in Section 2.3.1, but is able to more accurately capture the effect of asymmetrical scattering.

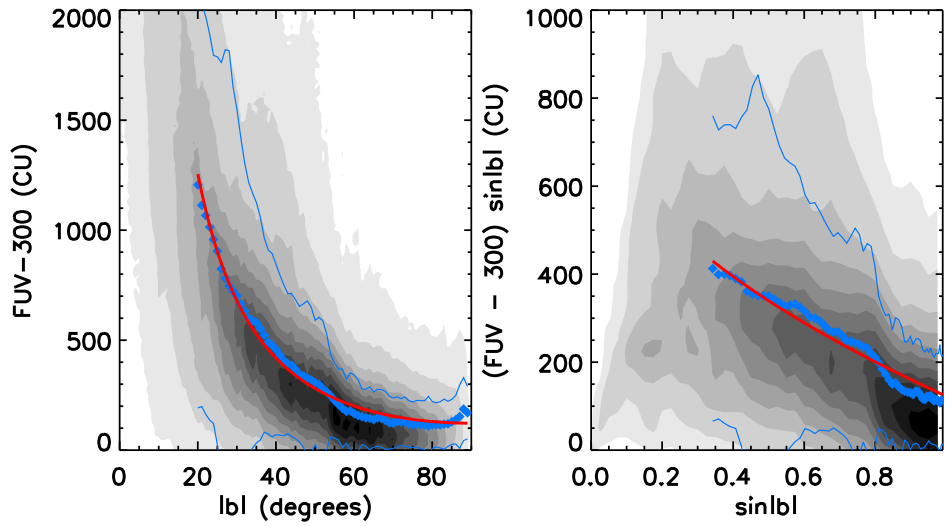

Figure 2.19 2-D histograms of FUV intensity vs. Galactic latitude, with 300 CU offset removed. **Left Plot:** FUV intensity vs. Galactic latitude, |b|. **Right Plot:** FUV sin|b| vs. sin|b|. Blue dots are the median for bins of 1°, above |b|=20°, with blue lines indicating the standard deviation. The red line is the best fit of Equation 2.5 for FUV intensity. Values of 0.62 ± 0.04, 0.78 ± 0.05, and 6260 ± 400 are used, for a, g, and S_o, respectively.

The values we derive for a and g are slightly higher but within the limits of previous measurements. Draine (2003), in a review of previous work, reported a range of modeled values for diffuse Galactic light (DGL) plus values predicted from dust models: a varied between 0.2 and 0.6 in the FUV, while g varied between 0.0 and 0.8. Albedo from the dust models of Weingartner & Draine (2001) was $a \approx 0.4$, with predicted scattering asymmetry of $g \approx 0.7$. Witt & Petersohn (1994) found $a = 0.5$ and $g = 0.9$. Schiminovich et al. (2001) fit for values of $a = 0.45 \pm 0.05$ and $g = 0.77 \pm .1$. Murthy & Conn Henry (2011) found limits on g between $0.58 \pm .12$, based on scattering angles around individual stars. Lee et al. (2008) find an albedo of $a = 0.36 \pm 0.20$, and $g = 0.52 \pm 0.22$. Reported values for a and g for individual regions or clouds have lower values than those of the DGL. For example, Lim et al. (2013) found $a = 0.42 \pm 0.05$ and $g = 0.47\ ^{+.11}_{-.27}$, for Taurus-Auriga-Perseus complex. See Draine (2003) for additional clouds and reflection nebulae. The range of values for a and

g in individual regions reflect in part the ambiguity of geometry in these clouds. Values for g in particular can vary if the dust is placed behind the illuminating stars or between the stars and the observer.

2.4.3 Deviations in FUV intensity

After accounting for the FUV offset and the scattering asymmetry of Galactic dust grains, there remain two high latitude regions of the sky that are worth further consideration. These two regions, one in the northern hemisphere and one in the southern hemisphere, have high FUV/IR ratios ($\sim$600 CU/(MJy/sr)) compared to ratios found in areas at the same latitude ($\sim$200 CU/(MJy/sr)).

As shown in Figure 2.13, the region above b=30°, and between $60° < l < 120°$ in the northern hemisphere and below b=-30° and between $240° < l < 300°$ in the southern hemisphere, have somewhat elevated FUV intensity given the dust content, even with the offset removal. These regions do partially coincide with structures in the halo (high latitude Galactic clouds) and some Galactic satellites including the Magellanic clouds and stream, but it is unlikely that excess FUV from these objects is being detected. Uniformly increasing the offset to require that these regions of the sky have zero FUV intensity (as the low levels of N_{HI} and 100 μm emission might require) ultimately causes other higher latitude regions of the sky to have negative FUV intensities. Thus, we do not think that the excess FUV intensity in these regions is a result of underestimating the offset.

Instead, we can consider two explanations for the excess FUV intensity here. The first case is that these regions contain additional FUV intensity that is unrelated to the dust

content. There are well known super bubble regions which contain FUV line emission due to ionized gas and other sources. However, known super bubbles are not coincident with the regions of interest, instead being adjacent (Orion-Eridanus in the south and Ophiuchus in the north) and likely unrelated to the FUV emission found in these regions. Furthermore, the known line emission in these regions is estimated at several thousand CU (in the case of Orion-Eridanus, Jo et al. 2011; Kregenow et al. 2006) and the FUV intensity in the regions of interest is only several hundred CU.

It might be more natural to consider a second possibility that infers a causal link between the low dust content and enhanced FUV intensity. One explanation for this may be that these regions are the remnants of old superbubbles. Such a remnant would have a low dust content as the super-bubble cleared out the dusty ISM in the region although a significant population of older UV-bright stars might remain to illuminate the surrounding area. That this could be the case is loosely suggested by the distribution of OB and A type stars from TD-1, as shown in Figure 15 of Seon et al. (2011a) and the lower ratios of Hα/FUV which may indicate the presence of a softer local radiation field with fewer ionizing photons. Furthermore, the presence of holes or chimneys in these directions is also suggested by observations of the 3-D distribution of the Local Bubble (Lallement et al. 2003) and the link to the EUV/soft-X-ray background. Alternative causes may be the leading arm of the Magellanic Stream having punched through the galactic plane, in a similar manner to that described by For et al. (2013) and McClure-Griffiths et al. (2008). Nearby nebular regions in the disk (e.g. the Gum Nebula) remain poorly understood and have been shown to contain expanding gas and clouds (Woermann et al. 2001) that may also trace successive generations

of star formation. We note that while star formation rate (e.g. FUV starlight) and molecular gas are globally correlated in external galaxy disks, on smaller physical scales less than 1 kpc they are known to show considerable scatter (e.g. Schruba et al. (2010), Leroy et al. (2013)).

2.5 Summary

We have constructed an all sky map of diffuse Galactic FUV intensity, using GALEX FUV AIS data, covering 65% of the sky. We have compared our map to other maps of the diffuse FUV sky and to maps of complementary Galactic quantities. We find the FUV intensity is highly dependent on a combination of 100 μm emission, Galactic latitude, and proximity to UV bright stars and OB associations.

Our main conclusions are:

1. FUV intensity is highest near the Galactic plane and around known OB associations and lowest at high latitudes.

2. There is a $\sim$300 CU FUV isotropic offset which is likely due to a combination of air glow (likely the dominant contributor), a small extragalactic background component including continuum light from unresolved galaxies, and/or a Galactic component not traced by other indicators.

3. FUV intensity and 100 μm emission show a linear correlation below 8 MJy/sr of 100 μm.

4. FUV intensity and N_{HI} show a linear correlation below 1.2×10^{21} cm^{-2}.

5. FUV intensity follows a modified cosecant shape with Galactic latitude with low intensity at high latitudes due to strongly forward scattering dust grains.

6. We calculate a best fit value of g=0.78 $\pm$0.05 for the scattering asymmetry, with a=0.62 $\pm$0.04 for albedo, and a peak scattering intensity, S_o=6260 $\pm$ 400 CU, for all points with |b| >20°.

A simple picture of this behavior is that the direct, linear variation of FUV intensity at low 100 μm emission can be explained as scattered starlight off of low optical depth dust. As 100 μm emission increases, the FUV intensity increases until reaching a plateau where the dust begins to self-shield. This plateau occurs at around 8 MJy/sr and appears to be constant across the sky. The exact ratio of FUV to 100 μm emission appears to depend on Galactic latitude, with starlight more effectively scattered at lower latitudes. The scatter in diffuse FUV intensity across a single latitude is primarily caused by anisotropies in the interstellar radiation field and geometrical effects caused by the exact structure of individual dust clouds. Less important, but still a component of the scatter could be variations in the type of dust present and the properties of that dust.

Of further interest are individual, small regions (less than 1 degree across) where FUV intensity deviates from the expected linear relationship with 100 μm intensity and modified cosecant model with Galactic latitude. These regions are typically individual dusty clouds or groups of clouds with high 100 μm emission. While only 10 % of our data covers points with 100 μm emission above 8 MJy/sr, this still contains numerous regions with flat or even inverse relationships between FUV and 100 μm. In a future paper, we discuss in detail individual clouds that deviate from the models described above, some of which show evidence

for FUV obscuration or excess FUV intensity.

2.6 Acknowledgements

This publication is based on observations made with the NASA Galaxy Evolution Explorer. GALEX was operated for NASA by the California Institute of Technology under NASA contract NAS5-98034. We acknowledge the use of the Legacy Archive for Microwave Background Data Analysis (LAMBDA), part of the High Energy Astrophysics Science Archive Center (HEASARC). HEASARC/LAMBDA is a service of the Astrophysics Science Division at the NASA Goddard Space Flight Center. This research made use of Montage, funded by the National Aeronautics and Space Administration's Earth Science Technology Office, Computation Technologies Project, under Cooperative Agreement Number NCC5-626 between NASA and the California Institute of Technology. Montage is maintained by the NASA/IPAC Infrared Science Archive. The authors also wish to thank Josh Peek for helpful discussions.

Chapter 3

The circumgalactic H-alpha spectrograph[1]

3.1 Introduction

Recent large scale simulations of the universe have pointed to the importance of a galaxy's environment in shaping its growth and evolution. This environment is generally split into several regimes: the immediate galactic halo, the circumgalactic medium (CGM), and the intergalactic medium (IGM). The CGM acts as an intermediary between the IGM and the galactic halo: gas from large scale filaments flows through the CGM to feed the galaxy while outflows due to star formation or AGN activity push back out through the CGM to pollute the wider IGM (Putman et al. 2012). This interplay, between gas flowing in and gas flowing out, may be a crucial part of understanding galaxy growth.

[1]This chapter is a slightly edited version of paper currently in preparation. The full author list for this article is: Hamden, Erika T.; Gordon, Samuel; Schiminovich, David; Corlies, Lauren.

The CGM is faint, since much of this gas is diffuse (over-density $\sim$1000) and the associated emission is quite low (emissivity scales as the square of density). Alternative ways of detecting this gas have relied on so called "pencil-beam" sightlines. This detection method uses very bright background objects to probe the CGM of foreground galaxies through absorption signatures from intervening material, as discussed in earlier in this thesis. Absorption lines from Lyman-α, MgII, and additional highly ionized metals have been detected in the halos of galaxies, and we have a rough, statistical understanding of how the CGM of a galaxy varies with distance from the galactic center (Werk et al. 2013; Tumlinson et al. 2013).

One drawback to this type of work is the limited number of bright sightlines in the background of a galaxy. An alternative to using quasar sightlines is to instead observe the CGM in emission by targeting specific, relatively bright, emission lines (van de Voort & Schaye 2013; Bertone & Schaye 2012) from nearby galaxies. As described earlier, one bright emission line in the rest-frame visible is Hα. In the CGM, Hα emission comes from at least two sources: photo-ionization or collisional ionization. Photo-ionized gas typically traces recent star formation and hot young stars, but may also be caused by the extragalactic UV background (EUVB). Collisionally ionized gas will trace shocks and may provide a tracer of hot outflows from galactic supernovae. Both sources of Hα emission can provide important details about the CGM of a galaxy.

CHαS has been designed specifically to detect both the presence of Hα emission in the outskirts of a galaxy and the dynamics of any emitting gas. This 3D picture is achieved using an integral field unit to capture both 2D spatial information and spectral information

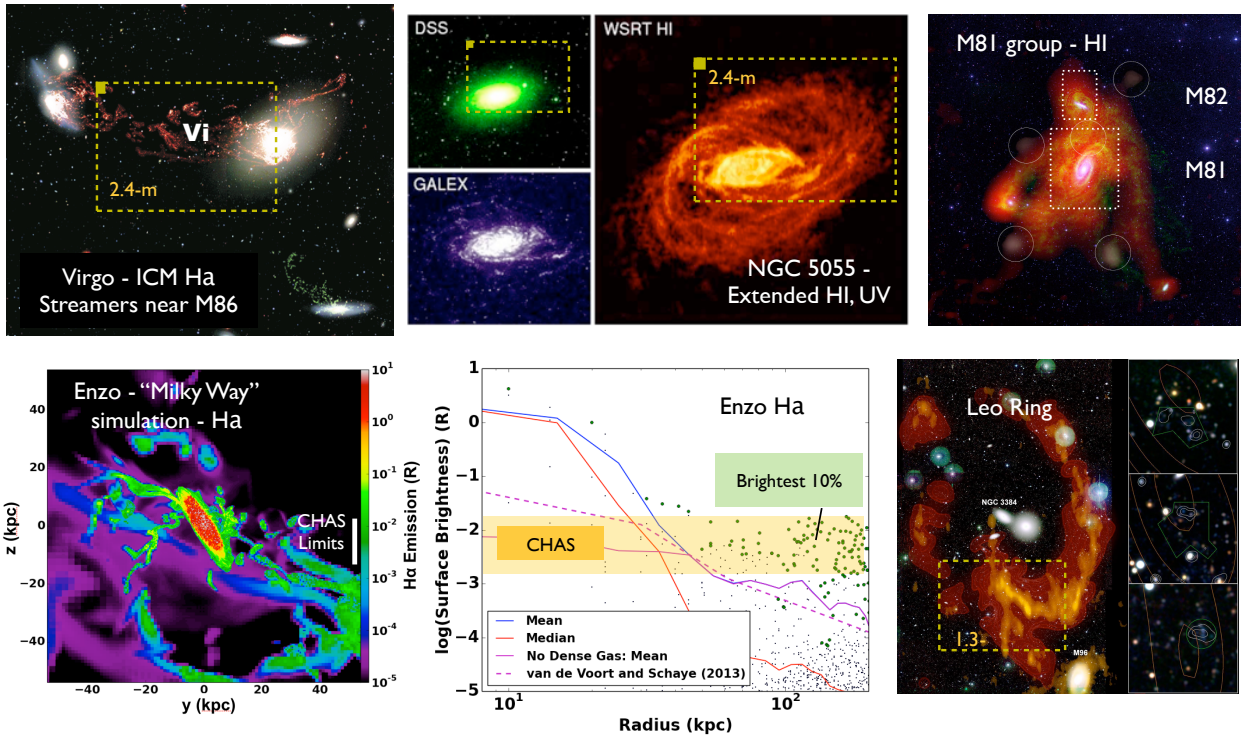

Figure 3.1 Models vs. Observations and possible CHαS targets with extended HI or detected bright (30-1000 mR) Hα emission. Figure used with permission from NSF ATI proposal, PI: D. Schiminovich. 2014 **Top Row:** Possible CHαS targets Virgo, NGC 5055, and M81 group. **Bottom Row** Enzo simulation by Joung et al. (2012) of a Milky Way like galaxy with radial profile indicating CGM filaments and other structure detectable by CHαS. Simulation figure courtesy of Lauren Corlies; Possible CHαS target Leo Ring.

for a wide field. Some examples of potential CHαS targets are shown in Figure 3.1.

3.2 Goals of CHαS

CHαS will be capable of detecting Hα emission that traces the photo-ionization of the CGM gas by the EUVB. We calculate the emission measure (EM) expected below.

$$EM = \int n_c^2 dl = \Gamma_{HI,z=0}/\alpha(T)N_{HI} \tag{3.1}$$

Where $\Gamma_{HI,z=0}$ is the incident rate of HI-ionizing photons at z=0 from the EUVB and α_B(T) is the temperature-dependent hydrogen recombination rate coefficient with assumed temperature 10^4K, Case B. Expected emission is calculated for N_{HI}=10^{17-18} cm^{-2} with a photo-ionization from the EUVB = 4×10^{-14} s^{-1}, and shown in Figure 3.2 as dashed and dotted lines. If we assume the emission region is 50kpc from the galaxy center with mean density between $3 \times 10^{-5} < n_H < 3 \times 10^{-4}$ cm^{-3}, or roughly over-densities of 100-1000 δ (where δ is the avergae density of the universe), we find expected intensities shown in the shaded region. CHαS will observe nearby galaxies, with distances less than 25 Mpc, and through many hour integration times, should be able to detect these low Hα intensities.

Calculations of the expected emission suggest CHαS will detect CGM clumps and filaments at the 1-10 mR (milli-Rayleigh) level. CHαS is able to reach these limits through a combination of large grasp (AΩ) and high resolution. CHαS's wide field of view and fast optics help provide a grasp which is comparable to, or even greater than, that of IFUs being built for large (8-10 m class) telescopes (Bershady 2009). The large grasp ($\Omega \sim 100$ m^2 arcmin^2) and high resolution (R$\sim$ 6000) are balanced by a very narrow-band over which spectra are taken ($\sim$ 30 Å). The limited bandpass focuses only Hα emission, with enough width to capture the rotation of the galaxy and outlying regions. CHαS is designed to observe nearby galaxies (with velocities between 0 and 2000 km/s), which fill the field of view, making it maximally efficient for this study.

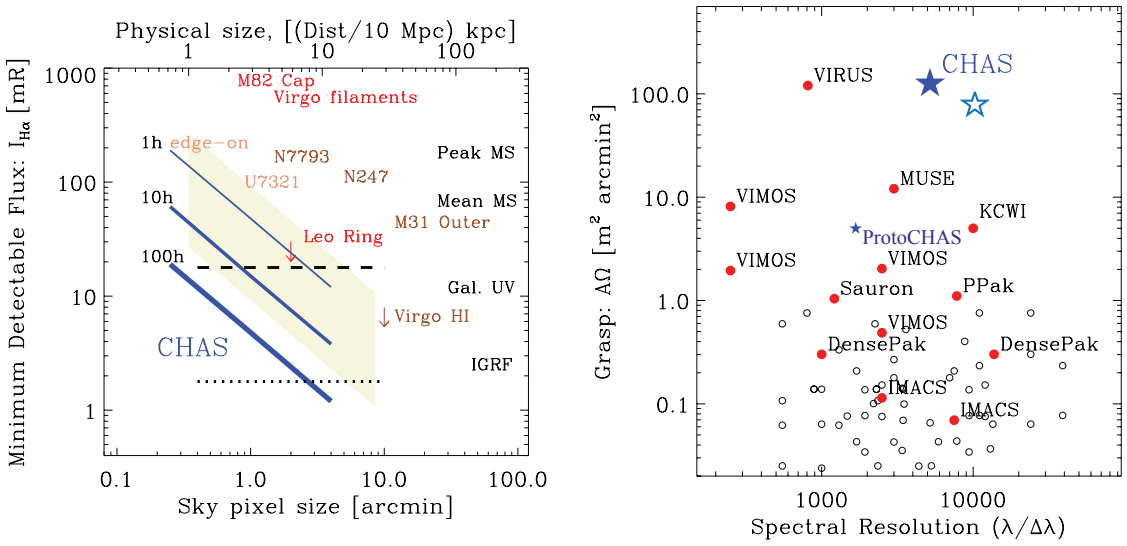

Figure 3.2 **Left Panel:** Minimum detectable flux for a range of objects, given "sky pixel" size. Dashed and dotted lines are expected emission as described in the text. Solid lines show expected detection limits for CHαS given observation length. Expected Hα emission from galaxies and other objects shown for comparison, including the Magellanic Stream (MS) and the intergalactic radiation field (IGRF). **Right Panel:** Effective grasp ($A_{eff}\Omega$) vs. spectral resolution ($\lambda/\Delta\lambda$). CHAS (blue stars, 1.3 m and 2.4 m MDM telescopes) vs. other current and planned integral field unit spectrographs (open circles; filled red circles are identified). CHαS has a grasp greater than nearly all other IFUs, many of which are significantly more complex and are designed for 8-10m telescopes. Comparison instrument data from Bershady (2009). Figure used with permission from NSF ATI proposal, PI: D. Schiminovich. 2014

3.3 Optical Design

CHαS is a monochromatic, low-cost, nebular spectrograph designed to be a facility instrument for the 2.4 m Hiltner and 1.3 m McGraw-Hill telescopes at MDM Observatory on Kitt Peak. A narrow-band filter (width of $\sim$ 30 Å) feeds a fast spectrograph with a dioptric Petzval collimator and camera, and a mechanically ruled grating. CHαS uses a micro-lens array as a field slicer and to speed up the telescope beam from f/7.5 to f/1.87. A summary of parameters for CHαS is shown in Table 3.1 and a schematic of CHαS is shown in Figure 3.3.

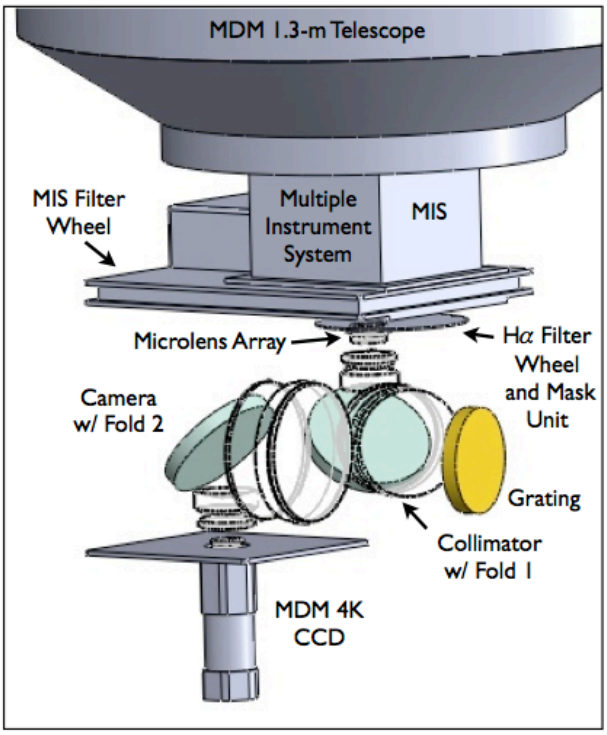

Figure 3.3 Optical layout of CHαS attached to the 1.3m telescope at MDM. The multiple instrument system (MIS) at MDM provides a standard interface for all instruments and contains a filter wheel with space for up to 8 filters. Two folding flats are used to keep CHαS compact. Figure courtesy of Sam Gordon.

CHαS is designed to observe Hα from galaxies with velocities from 0 to 2000 km/s, but is optimized for observations centered around 6586 Å(v $\sim$ 1100 km/s), to avoid contamination from Galactic Hα. To utilize this range narrow-band filters will be employed, each of which covers only a few hundred km/s, including NII. SII is also a possible filter for CHαS accessing Hα at z=0.025 (velocities of $\sim$7000 km/s, e.g. for Coma cluster).

The microlens array will be positioned at the Cassegrain focus of the telescope. The array will have a pitch of 250 μm and reduce the focal length from f/7.5 to f/1.87. An opaque mask will cover the spaces between lenslets and minimize crosstalk and scattering from the microlens array. The spectra for CHαS are packed tightly together on the detector, with the

pitch of the microlens setting the distance between spectra. While this limits the wavelength coverage in any one observation, the use of a micro-lens array instead of a field slicer or fiber bundle helps to limit the cost of construction over the wide field of view.

CHαS uses two identical Petzval lens combinations acting as a collimator and a camera, with standard AR coatings for $> 99\%$ transmission. CHαS will use a standard commercially available mechanically ruled grating (1200 grooves/mm), blazed at 6000 Å for use in the first order near Hα. We expect efficiencies of greater than 50% given the narrow bandpass. Finally, CHαS will use the existing facility detectors available at MDM. This includes the MDM 4K, an STA-0500 CCD with 15 μm pixels. The CCD will be binned 2x2 and has a standard gain of 2.2-2.4 electrons per ADU with a read noise of 5 electrons (RMS).

Parameter	**Quantity**	**Unit**	**Comments**
Telescope Aperture	2.32	m	MDM Hiltner 2.4m
Geometrical Area	37914	cm^2	Entrance Pupil
System Throughput (Hα)	0.18		w/o atmosphere, w/ telescope
Central λ, FWHM	6586, 30	Å, Å	assuming standard NII filter
Microlens Field of View	12x15, 24x30	$arcmin^2$	total on 2.4m, on 1.3m
f/# Telescope	7.5		2.4m and 1.3m
f/# Lenslet/Spectrograph	1.87		
Grating Parameters	1200, 6000	grooves/mm, Å	Groove freq., Blaze λ
Spectra per image	240x320		
Spectral Res. element/bandpass	1.2/25 [60/1000]	Å [km s^{-1}]	Band $\sim$ 25 Å. R vs. pitch
Expected Minimum Detectable Flux			**Sky Pixel**
I_{min}: t_{exp} 1 hr, S/N = 10	190/50/12	mR	15"x15",1'x1',4'x4' pix
I_{min}: t_{exp} 10 hr, S/N = 10	60/16/4	mR	15"x15",1'x1',4'x4' pix
I_{min}: t_{exp} 100 hr, S/N = 10	18/5/1.2	mR	15"x15",1'x1',4'x4' pix

Table 3.1 Summary of CHαS parameters and sensitivity calculations. 1 R= 79365 ph s^{-1} cm^{-2} sr^{-1} = 5.7×10^{18} ergs s^{-1} cm^{-2} $arcsec^{-2}$=2.8 cm^{-6} pc (EM, case B).

3.4 Proto-CHαS vs. CHαS

A proto-type of CHαS was designed and built at Columbia University using internal funding, as a low-cost feasibility study. Dubbed proto-CHαS and shown in Figure 3.4, this instrument differs from CHαS in several small ways. The first is the use of a relay to re-image the focal plane on the microlens several inches below and to the side of the Cassegrain focus. The microlens was not an exact match to the one planned for CHαS so the focal reduction was not as large. proto-CHαS also uses off the shelf, 2 inch optics from ThorLabs, with slightly different optical performance from CHαS which will have custom made optics. Finally, the smaller size of the optics reduced the overall field of view from 15x15 arcmin to 3.8x3.8 arcmin (for the 2.4 m), with 2.9" lenslet pixels. Despite these differences, we have had stunningly successful observing runs.

Beginning at the telescope focus, the light passes through either an Hα or NII filter, obtained from Astrodon, Inc., with 3nm FWHM band-passes. The filtered beam is then reflected through a relay, consisting of a flat mirror at 45° angle of incidence to the incoming beam, two achromatic doublets, two more flat mirrors, and a field lens. This re-images the focal plane on the microlens array. proto-CHαS uses a 20x20 mm microlens array from Advanced Microoptic Systems GMBH. This array had hexagonal packing of two-sided lenslets, with a 250μm pitch between lenslets. The microlens array acts as a focal reducer, resulting in an f/3 beam through the spectrograph optics (beam from the telescope is f/7). The microlens array is covered by an optical mask, made by Fineline Imaging. These masks have 200 μm diameter apertures designed to block cross-talk from between lenslets and interstitial boundaries. We also masked half of the lenses to lower the spectral packing, reducing

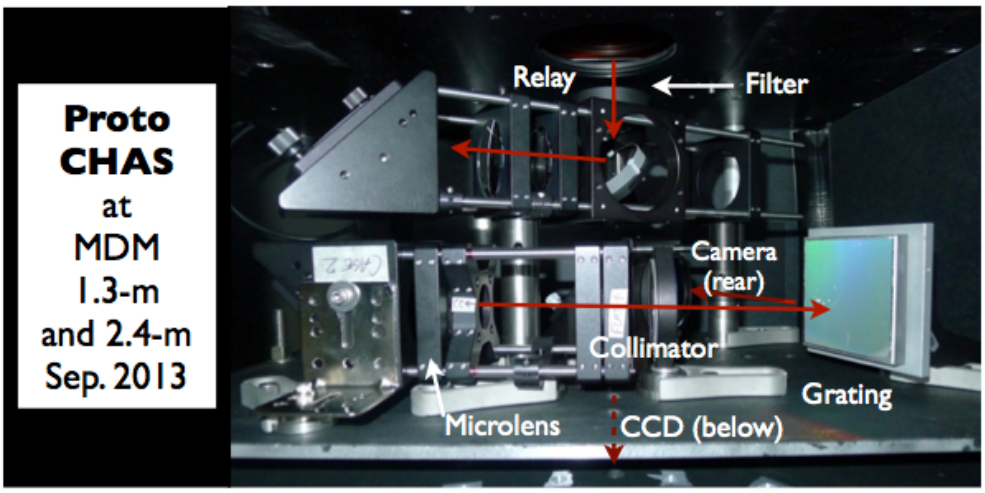

Figure 3.4 Side view of proto-CHαS as installed at MDM in September 2013. Light path is indicated by red arrows.

spectra overlap, simplifying both observations and data reduction. This resulted in a net filling factor of 30% on the sky, with a grid of 80x40 lenslets. The light than passes through the collimator lenses, reflects in the first order off the grating (from Richardson gratings), and is focused by a set of camera optics. There is a folding flat in the camera optics, at a 45 degree angle, to direct the light downward, into the MDM detector. The MDM detector is centered over the original telescope focus. A picture of proto-CHαS as installed at MDM is shown in Figure 3.4.

The optical bench and MDM detector interface plates were machined in-house and at Rush Machinery, respectively. The detector used is the MDM 4K, originally built by Ohio State. Our engineering run used the Templeton detector, a 1kx1k imager. The MDM detector interface plate also supported the enclosure and optical bench.

proto-CHαS first light occurred in April, 2013 using the MDM Templeton CCD. This run verified basic interfaces and general system functionality. A second and third run suc-

cessfuly observed a number of science targets in September 2013 and April 2014. These targets are summarized in Table 3.2.

3.5 First Data from proto-CHαS

3.5.1 Data Analysis

We have written a preliminary pipeline to reduce data from proto-CHαS. This pipeline takes raw images from our observing runs and extracts each of the 3200 spectra, performs wavelength calibrations, and creates a data cube, containing x,y, and λ information. Data cubes from each individual image are combined for observations of the same object, with automated registration to align the cubes. Certain galaxies and nebulae are large enough that tiled observations were necessary to cover the whole object. Here we outline in detail the data reduction pipeline.

Images taken with the MDM 4K detector display well known artifacts from cross-talk between amplifiers. A 16 pixel overscan is read out on each side of the image. This overscan is later used by the program proc4k to remove both the cross-talk and subtract bias levels from each image. Figure 3.5 shows example images taken with proto-CHαS of the Ring Nebula and of a calibration flat, both with cross-talk and bias removed. Small spectra are clearly visible, with the close packing a result of the microlens array. Two lenslets in the center of the field have been masked to provide a fiducial for our initial setup.

The next step is simple cosmic ray removal from all image types- *neon*, *flat*, *dark*, and *object*. This is done using sigma clipping. We then create master dark images for 300 second

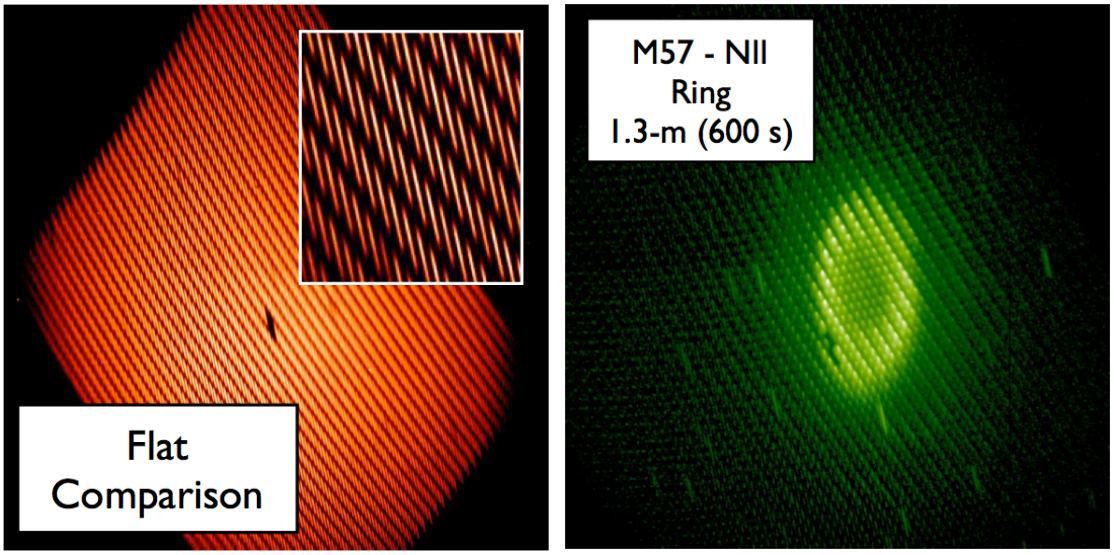

Figure 3.5 **Left:** Calibration flat from proto-CHαS. The microlens array is angled to prevent spectra overlap, and thus the image appears as a diamond on the detector. The inset shows a close up of the flat. Each line is a spectrum from a single lenslet. **Right:** Image of Ring Nebula from proto-CHαS after cross-talk and bias removal, but before additional reduction. The shape of the object is quite evident, and there are clear emission lines in each spectrum.

and 600 second exposures by taking the median of all darks with the correct exposure time. These master darks are applied to the *object* files. Mean dark counts are 7.0 and 5.4 counts (median dark counts are 2.5 and 1.5) for a 600 and 300 second exposure, respextively. *neon* and *flat* files are not dark subtracted since their exposure times are quite short (5 and 30 seconds, respectively).

The initial steps for spectra extraction require locating the position and dispersion of each individual spectrum, since these vary across the proto-CHαS field with each lenslet's *i,j* grid position. Furthermore as the telescope moves throughout the night, flexure in proto-CHαS causes the exact location of the spectra to move in the image. The flexure moves the field of view about 20 pixels in x and 10 pixels in y over the course of a night. To account for this, calibration flats and neon lamps were taken before and after observations for all

targets. For long observation times, additional calibration images were taken about every hour. The position of spectra relative to each other did not change with time, only their absolute position on the detector. Thus, a single solution can be applied to each image with only an x and y offset to account for the flexure. After finding a position solution, we also used calibration images to determine the wavelength dispersion for each spectrum, which changes across the field of view.

Dispersion was calculated using neon lamp images taken at zenith. Flats of neon emission lines at 6532.882 and 6598.953 were taken using the Hα and NII filters, respectively, without moving the telescope. We calculated the dispersion based on the distance between these two emission lines, finding a linear solution over all lenslet points. We assume that the dispersion does not change over time or with telescope flexure, but only depends on the lenslet.

Once the position and length of each spectra has been found on the calibration images, the proto-CHαS pipeline extracts a spectrum from the same position on the *object* image, creating a grid of spectra, one for each *i,j* position. Values are extracted from the center of the spectra and 2 pixels to either side, and added together. Spectra are extracted in the same way from the *neon* and *flat*, creating three spectra for each *i,j* position. The location of the neon peak at 6598 Å is used to assign an absolute wavelength value to each spectra. This wavelength calibration is verified by checking the spectrum of the corresponding $flat_{i,j}$ vs. the expected spectrum from the filter. Finally, each individual spectrum is interpolated onto a larger data cube with indices *i,j,*λ.

These data cubes are made for each *object* image (and associated *flat* and *neon* images).

Cubes for the same target are then co-added using an automated registration. A single cube is selected as the base against which other cubes are compared. The comparison cube is translated in x and y and both cubes are multiplied together. The Δx and Δy values at maximum are considered best fit. Refinement by hand is done after the automated registration to verify a good match.

The proto-CHαS field is not flat. Spectra along the very edges of the field of view are 50-75% dimmer than the brightest spectra. To correct for this, a master median flat spectrum is created from a single *flat* continuum lamp image. The central 20 wavelength channels in each *i,j* spectrum in a flat cube are compared to the same channels in the master flat spectrum to create a normalized flat field cube. This normalization is then used for flat fielding when adding up all object cubes.

After registration of all *object* cubes, three composite cubes are made. The first is the addition of all *object* cubes according to the registration. The extreme edges of the cubes in *i,j* are not included in all composites since they typically have very low throughput and only increase noise. The second is the addition of all *normalized flat* cubes, also following the registration and not including the edge spectra. Similarly, a cube is made of exposure times, again following the registration and not including edge spectra.

Finally, to create a cube with units of counts s^{-1} $Å^{-1}$ $pixel^{-1}$ we combine the three cubes:

$$Final_{i,j,\lambda} = \frac{CompositeObjectCube_{i,j,\lambda}}{CompositeNormalizedFlat_{i,j,\lambda} \times CompositeExposureTime_{i,j,\lambda}} \tag{3.2}$$

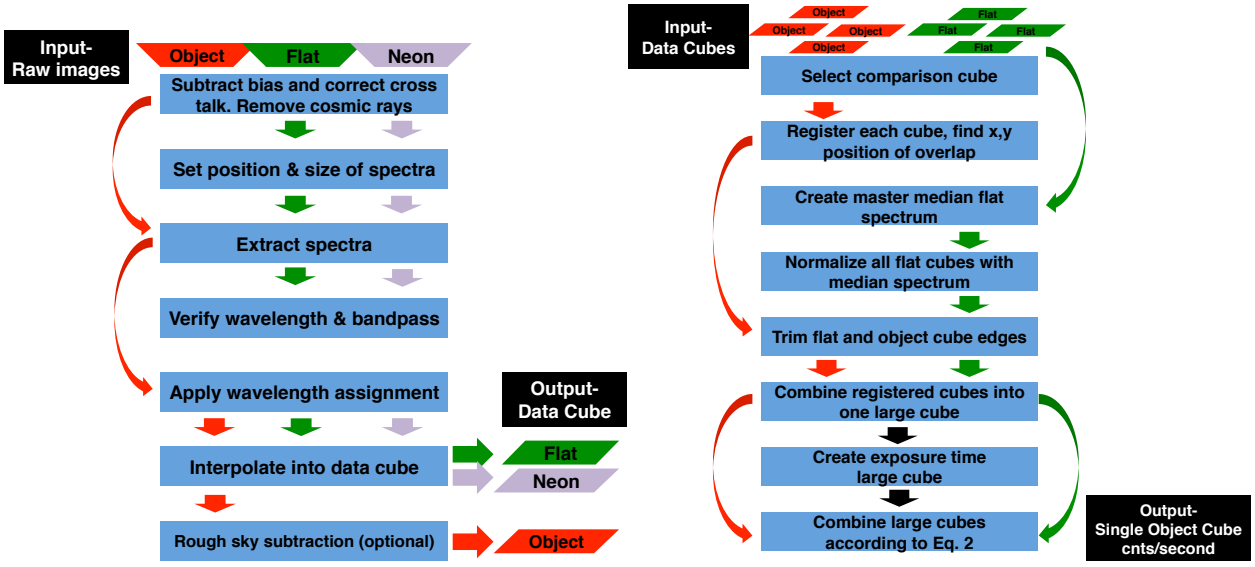

Figure 3.6 **Left Panel:** Flow chart of proto-CHαS pipeline from raw images to three data cubes, the *object*, *neon*, and *flat* cubes. **Right Panel:** Flow chart of proto-CHαS pipeline from individual data cubes to finished large cube of all observations of a single object.

This can then be converted to a surface brightness assuming each lenslet covers a solid angle of 17 arcseconds^2 (taking into account the masking), A_{geo}=10827 cm^2 for the 1.3 m telescope, and the CCD gain is 2.2 electrons/ADU. The overall throughput takes into account losses due to transmission, reflectance, and scattering, the grating efficiency, and pupil masking. A flow chart of the pipeline is shown in Figure 3.6 for clarity.

3.5.2 Results

We present initial results from our fall 2013 run. These results used the large composite cubes from several nights worth of observations. Initially, we focus on characterizing proto-CHαS as a whole, determining spectral resolution, verifying wavelength calibration, and overall throughput.

Using the *neon* data cube, we find the median FWHM of an emission line over the

proto-CHαS field to be 4.3 Å. The calibrated wavelength assignment for Hα and NII agrees with expected position of these emission lines in several targets, matching the expected wavelength to within 1 Å.

Overall throughput is calculated using a target with known flux at either H-α or NII. We focus on the Ring Nebula as a good standard. The average NII surface brightness on and adjacent to the bright ring region (Hawley & Miller 1977) was 3.8 $\times 10^{-14}$ ergs cm^{-2} s^{-1} arcsec^{-2}. Using our own data averaged over the ring region, we integrate NII flux over the 4 Å line width and find an uncalibrated surface brightness of 1 $\times 10^{-15} \times k$ ergs cm^{-2} s^{-1} arcsec^{-2}. The final flux we detected depends on the combined overall throughput of the instrument and the solid-angle losses due to our focal plane masking, expressed as an efficiency factor k. As discussed above, every other lenslet was masked to prevent overlapping spectra on the detector. Furthermore, the lenslet aperture of 250 μm in diameter was reduced to 200 μm to minimize crosstalk and scattering between lenslets. The lenslet masking gives a fill factor of 32%. This yields an overall throughput for proto-CHαS of 8.2%.

proto-CHαS has a grasp ($A_{eff}\Omega$) of $\sim$1.5 m^2 arcmin^2, with a spectral resolution ($\lambda/\Delta\lambda$) of 1600. We calculate the detection limit of proto-CHαS in Section 3.5.2.1.

3.5.2.1 NGC 7331

NGC 7331 is a SA(s)b galaxy with a total stellar and gas mass of 1.6×10^{11} M$_\odot$ (Thilker et al. 2007) at a distance of 14.7 Mpc (Freedman et al. 2001) measured by cepheids. NGC 7331 has a velocity of 816 km/s, red-shifting the Hα emission line to 6580 Å. We observed NGC 7331 for roughly 7 hours total using proto-CHαS with observations of both the galactic

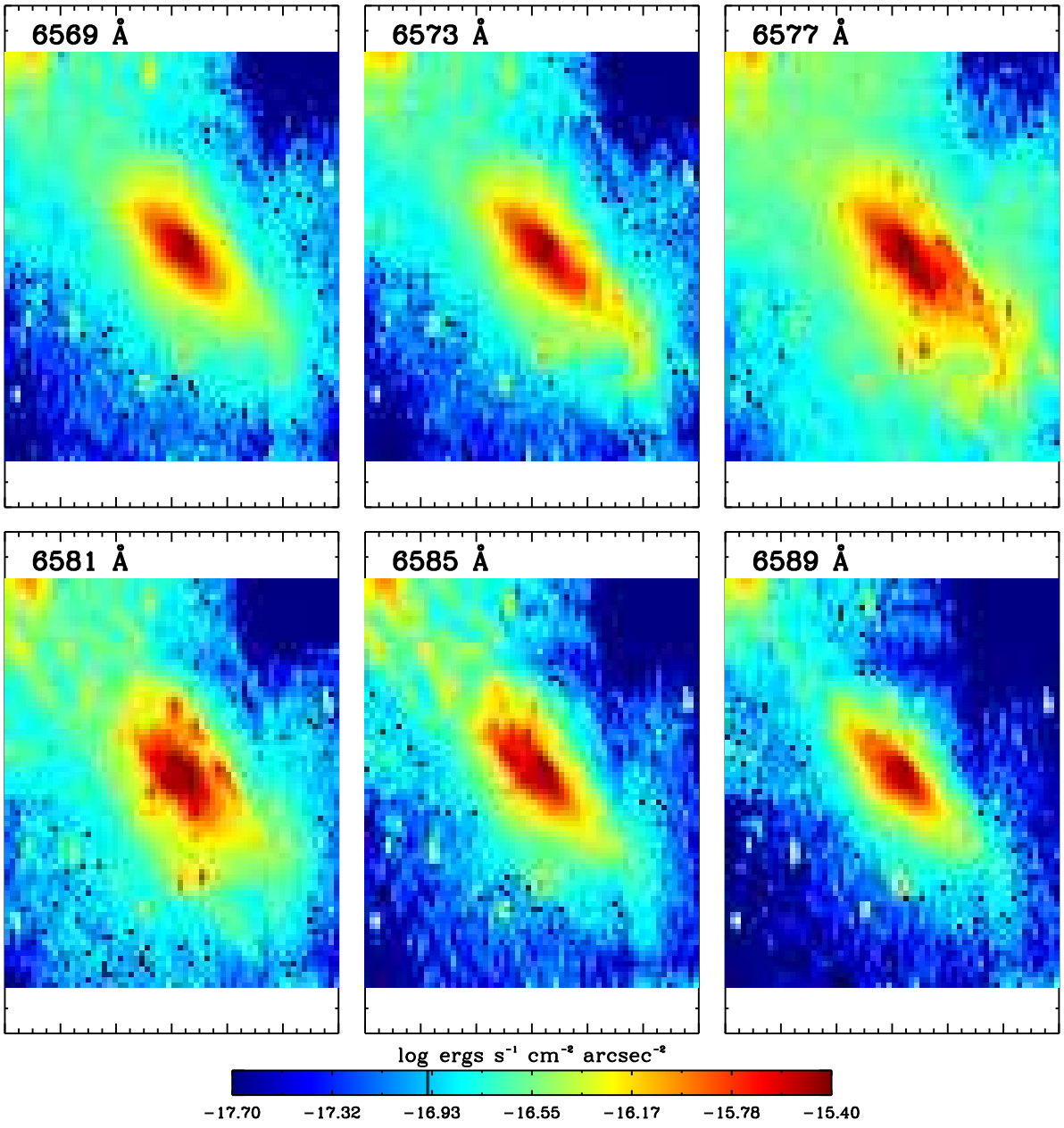

Figure 3.7 Channel maps for NGC 7331. Each panel shows surface brightness integrated over bins of 4 Åcentered around the wavelength shown, starting with 6569 Å in the upper left. One spiral arm of NGC 7331 can be seen in the lower right in the shortest wavelength maps, indicating a blue shift relative to the galaxy.

center and the outer regions of the spiral arms. Figure 3.7 shows channels maps from the composite data cube in bins of 4 Å.

The rotation curve of the galaxy is clearly visible, with the lower right arm rotating towards us and the upper left arm rotating away. The outer arm regions were not observed for as long as the galactic center, and so have lower signal to noise.

We use the NGC 7331 data cube to estimate the limiting sensitivity of proto-CHαS, assuming a sky background limited regime. The average background noise level is $\sim$2.3 R (or 1.31×10^{-17} ergs cm^{-2} s^{-1} arcsec^{-2}) at 6580 Å(redshifted Hα). Summing over the 4 Åline yields a background noise level of 10.1 R. This translates to 0.04 cnts s^{-1} pix^{-1} (efficiency of 0.025, with pixels of 17 arcsec^{-2}). Assuming a minimum valid signal to noise of 10, we find a minimum detectable flux of 1 R (5.7×10^{-18} ergs cm^{-2} s^{-1} arcsec^{-2}) for a 7 hour observations with 15"$\times$15" binned pixels (3$\times$3).

3.6 Future for CHαS

CHαS has recently been approved for funding by the NSF and will be built over the next few years. My work building and operating proto-CHαS provided an important proof of concept for the use of the microlens array in particular. We were able to verify its efficiency in slicing up the field while still being able to distinguish one spectrum from another. In our initial data analysis, we are able to clearly see large scale Hα emission from several galaxies. The rotation curve of NGC 7331 is just the first quick example of future interesting results. A more careful analysis of our combined data cubes, with good sky subtraction, should reveal Hα emission in the outer regions of other observed galaxies. While we were not able to conduct hundred hour observations with proto-CHαS, we observed several galaxies for $\sim$3 hours (NGC 7331 was the longest at 7 hours). These would provide minimum detectable

fluxes on the order of a few R, potentially revealing features similar to the Virgo filaments and the M82 Cap.

There are several potentially interesting objects: NGC1569 contains an Hα-bright hook feature, perpendicular to the plane of the galaxy. NGC 660 and IC 10, both unusually shaped galaxies, have Hα morphologies which may shed light on ongoing star formation. NGC 660 in particular is believed to have recently undergone a merger, resulting in a prominent polar ring containing recent star formation and its attendant Hα emission (van Driel et al. 1995). NGC 628, a grand design spiral, shows many Hα bright clusters along its spiral arms. These features, while not necessarily tracing the EUVB, and others revealed through deeper observations, will still trace inflowing and outflowing gas, illuminating the dynamic CGM around these nearby galaxies.

Table 3.2: Target information and total observation time for Fall and Spring proto-CHαS runs. 2013 run was at the 1.3m McGraw-Hill Telescope at MDM Observatory, from September 27th to October 1st, 2013. 2014 run was at the 2.4m Hiltner Telescope at MDM Observatory, from March 28th to April 6th, 2014.

Date	**Target**	**RA**	**Dec**	**Filter**	**Time (s)**
2013	M31	00 42 44.3	41 16 09	Hα, NII	1800
2013	NGC628	01 36 41.7	15 47 01	NII	7200
2013	NGC660	01 43 02.4	13 38 42	NII	8400
2013	NGC925	02 27 16.9	33 34 44	Hα	3600
2013	NGC1012	02 23 14.9	30 09 05	NII	3600
2013	ARP213	04 07 46.9	69 48 45	NII	6000
2013	NGC1569	04 30 49.0	64 50 43	Hα	8400
2013	NGC2146	06 18 37.7	78 21 25	NII	3000
2014	ATCNC	08 28 36.9	25 20 03	NII	6000
2014	IZW18	09 34 2.0	55 14 28	NII	3000
2014	M82+Cap	09 54 56.0	69 52 37	Hα	3000
2014	M81 Loop	09 57 14.8	69 16 46	Hα	1800
2014	NGC3239	10 25 04.9	17 09 49	NII	3600
2014	NGC3310	10 38 45.8	53 30 12	NII	3600
2014	NGC3432	10 52 19.0	36 38 8	NII	12600
2014	NGC3447	10 53 14.8	16 44 44	NII	3600
2014	Owl Nebula	11 14 47.7	55 01 8.5	6730/15 & 6715/14	600
2014	NGC3705	11 30 7.0	09 16 36.0	NII	4800
2014	NGC3718	11 32 34.9	53 04 05	NII	5400
2014	NGC4013	11 58 19.4	43 5548	NII	5400
2014	NGC4217	12 15 50.7	47 05 30.0	NII	5400
2014	KPG332	12 21 37.6	14 36 08	NII	1200
2014	M86	12 26 11.7	12 56 46	Hα	5400
2014	NGC4414	12 26 27.1	31 13 25	NII	4200
2014	NGC4438	12 27 45.6	13 00 31	Hα	2400
2014	M49	12 29 46.7	08 00 02	NII	1800
2014	VCC1249	12 30 01.0	7 55 46	Hα	2400
2014	NGC4625	12 41 41.0	41 15 5	NII	13200
2014	NGC4656 UV	12 44 15.7	32 17 00	NII	13200
2014	IC4040	13 00 37.9	28 03 26	6730/15	1800

Continued on next page

Table 3.2 – continued from previous page

Date	Target	RA	Dec	Filter	Time (s)
2014	M101	14 03 12.6	54 20 57	Hα	1800
2014	NGC5474	14 04 51.6	54 39 14	Hα	1800
2014	NGC5477	14 05 23.3	54 27 0	Hα	1800
2014	NGC5585	14 19 38.2	56 42 15	Hα	1800
2014	NGC5866	15 06 29.5	55 45 48	NII	11400
2014	NGC5879	15 09 46.7	57 00 01	NII	7200
2014	NGC5907	15 15 29.8	56 21 44	NII	8400
2013	NGC6239	16 50 05.0	42 44 23	NII	9000
2013	NGC6503	17 49 26.4	70 08 40	Hα	5400
2014	Cat's Eye	17 58 33	66 37 59.52	Hα	4800
2014	Ring Nebula (M57)	18 53 35.1	33 1 45	NII, Hα, 6715/14	1800
2013				Hα, NII	4800
2013	M27	19 59 36.3	22 43 16	Hα/NII	8460
2013	NGC7094	21 36 53.0	12 47 19	Hα/NII	2400
2013	NGC7331	22 37 04.0	34 24 56	NII	25200
2013	IC10	00 20 17.3	59 18 14	Hα	9000

3.7 Acknowledgments

The authors wish to thank the staff and support team at the MDM Observatory at Kitt Peak. This work was funded by support from Columbia University Internal Funds and by a NASA Earth and Space Sciences Fellowship, Grant No. 13-ASTRO13R-0010.

Chapter 4

UV anti-reflection coatings for use in silicon detector design[1]

4.1 Introduction

Charged Coupled Devices (CCDs) were first invented at Bell Labs in 1969, and have since revolutionized imaging. The CCD's ability to quickly and efficiently digitize data, its relatively low noise capabilities, and a sensitivity 100 times that of film meant that they quickly became indispensable to modern astronomy (Janesick 2001). For UV astronomy, CCDs have not historically been a success. While film is sensitive at nearly all wavelengths of light, unmodified CCDs present a number of deficiencies. The front circuitry of a CCD is absorptive at UV wavelengths. For high efficiency, CCDs are back illuminated, however the Si substrate

[1]This chapter is a slightly edited version of a previously published paper which appeared in *Applied Optics*. The full citation for this article is: "Ultraviolet anti-reflection coatings for use in silicon detector design". E. T. Hamden, F. Greer, M. E. Hoenk, J. Blacksberg, M. R. Dickie, S. Nikzad, D. C. Martin, and D. Schiminovich. *Appl. Opt.*, 50:4180–4188, July 2011.

is in turn highly reflective. More crucially, UV photons have a very short absorption depth in Si. The resulting electron-hole pairs find traps at the surface and never reach the gates for eventual readout. These characteristics have created problems in developing efficient CCD based UV detectors. One notable work-around to these issues was used for the Wide Field Planetary Camera 2 (WFPC2) on the Hubble Space Telescope (HST) (Holtzman et al. 1995). WFPC2 used thick, front illuminated CCDs but coated them in a layer of the UV phosphor Lumogen, which provided a UV response of 10-15% from 200 to 400nm by down converting the UV photons to 510-580nm photons. The current camera on HST, WFC3, also utilizes a CCD (thinned and backside illuminated with a charged backside) and AR-coating for near UV, but suffers somewhat from quantum efficiency (QE) hysteresis (Baggett et al. 2010; Collins et al. 2009). Other types of UV detectors have been developed and are in use on current missions, including micro-channel plates (MCPs) (such as JUNO Gladstone et al. 2008, FUSE Moos et al. 2000, GALEX Martin et al. 2003, ALICE Stern et al. 2008, and FIREBall-1 Tuttle et al. 2008, to name a few). While their photon-counting capabilities make them useful and at times the only option, MCPs still suffer from low quantum efficiency (QE from 25% in the FUV (1344-1786 Å) down to 8% in NUV (1771-2831 Å), for the GALEX MCPs) and are challenging to produce and utilize. Additionally, the MCPs on GALEX could not observe very bright objects with high count rates (discussed in Chapter 6), which limited the targets that GALEX observed. In this work, we examine an improved CCD which is able to overcome the difficulties described above.

Improvements to traditional CCD design beyond optical use have been made in recent years with the advent of delta-doped backside illuminated CCDs (Hoenk et al. 1992). Using

a custom backside treatment developed at JPL, these modified CCDs achieve near 100% internal quantum efficiency from the ultraviolet to the near infrared. This is achieved by thinning the backside surface to the epilayer (which can vary between 5-20μm depending on CCD type) and then delta-doping the thinned backside layer. Delta-doping passivates the silicon surface and produces a highly stable, QE-pinned detector. The atomic-scale precision of molecular beam epitaxy (MBE) growth is used to embed a layer of dopant atoms with the silicon lattice, which, when ionized, forms a sheet of negative charge that isolates the surface from the bulk. The boron atoms used in this case have an areal density of 2 $\times 10^{14}$ cm^{-2}, and are confined by MBE growth to nearly a single atomic plane located 1.5nm below the silicon surface. These adaptations have greatly expanded the spectral range of modified CCDs, while also dramatically increasing QE and stability compared to their ready-made brethren (Nikzad et al. 1994). Further work on anti-reflection (AR) coatings in the visible and near-infrared has been successful ((Blacksberg & Nikzad 2006), (Nikzad et al. 1994)), prompting the current efforts to create similar AR coatings for the ultraviolet. The technical limitations preventing new, innovative designs in UV detectors are quickly receding, and further development in the manufacturability of these thinned and doped devices is underway (Hoenk et al. 2009). This chapter describes work on the design, modeling, materials considerations and sample measurements on live devices as part of a larger effort for development of high QE, high performance far UV detectors.

This chapter focuses on the development of an astronomical detector optimized for use with a monolithic UV spectrograph from 120 to 300nm. Due to the highly variable indices of Si, no single material or thickness is sufficient to achieve high QE over the whole range.

The lack of a suitable broadband AR-coating in the UV does not rule out alternatives, and one can still achieve excellent performance through a creative use of coatings. Sacrificing a single coating, and thus broadband imaging potential, and instead using a series of sequential narrowband coatings allows for higher QE overall. Following this idea, a delta-doped CCD is to be coated in sections using different materials (an alternative would be a mosaic of devices, each with one coating). This tiling lends itself most readily to a fixed spectrograph, where only one wavelength of light hits a particular region on the CCD. Spectrographs with a fixed grating are becoming more common since they are relatively easy and low cost to mass-produce. Space based instruments may also employ a fixed grating to reduce complexity and cost.

We have selected MgF_2, MgO, HfO_2, Al_2O_3, and SiO_2 to test as suitable AR coatings. The materials chosen reflect the unique requirements of a UV AR coating, including a favorable index of refraction and low absorption in the desired waveband. One must be able to deposit the film in a uniform way, while not causing damage to the CCD itself. This eliminates electron beam evaporation (a common choice for dielectric coatings) as a potential technique because it causes X-ray damage to the CCDs. We have tested sputtering, atomic layer deposition (ALD), and thermal evaporation techniques for consistency and measured the reflectance of films on a substrate of bare Si. This is a low cost, faster alternative to testing on live devices. The downside is that testing is limited to reflectance off this surface, which necessarily omits any absorption losses. We then compare our measurements to the theoretical models. A further discussion of deposition techniques and their effect on film quality can be found in Greer et al. (2013).

We also briefly report on the application of films onto live devices. A detailed account of these results is described in Nikzad et al. (2012). Briefly, thinned and delta-doped standard and EMCCDs were both used in a variety of tests to measure absolute QE. EMCCDs are an advancement in CCD technology which enables photon-counting. A longer explanation is provided in Section 4.4. These live device tests provide a more realistic view of the performance of these films than simple reflectance tests. With live devices we are able to directly measure the effect the AR coating has on transmission into the the Si. More recent work from our group has focused on the stability and testing of these devices, as well as on detailed live results and future FUV detector technology (Nikzad et al. 2012; Jacquot et al. 2011).

Here we report on the growth of these films and the optical testing of reflectance which we have performed. In Section 4.2 we discuss how films were deposited and what materials were chosen. In Section 4.3 we discuss the conditions for reflectance testing, following with a discussion of our results in Section 4.3.1. We also include a discussion of the data from live devices in Section 4.4. Finally we briefly look to future work and more advanced coating models in Section 4.5.

4.2 Techniques

All film depositions were performed at the Jet Propulsion Laboratory (JPL) using thermal evaporation, Atomic Layer Deposition (ALD), and Radio Frequency (RF) dielectric sputtering. We have used thermal evaporation to deposit layers of MgF_2 and RF sputtering to deposit layers of MgO and SiO_2. RF sputtering and ALD were both used for making films

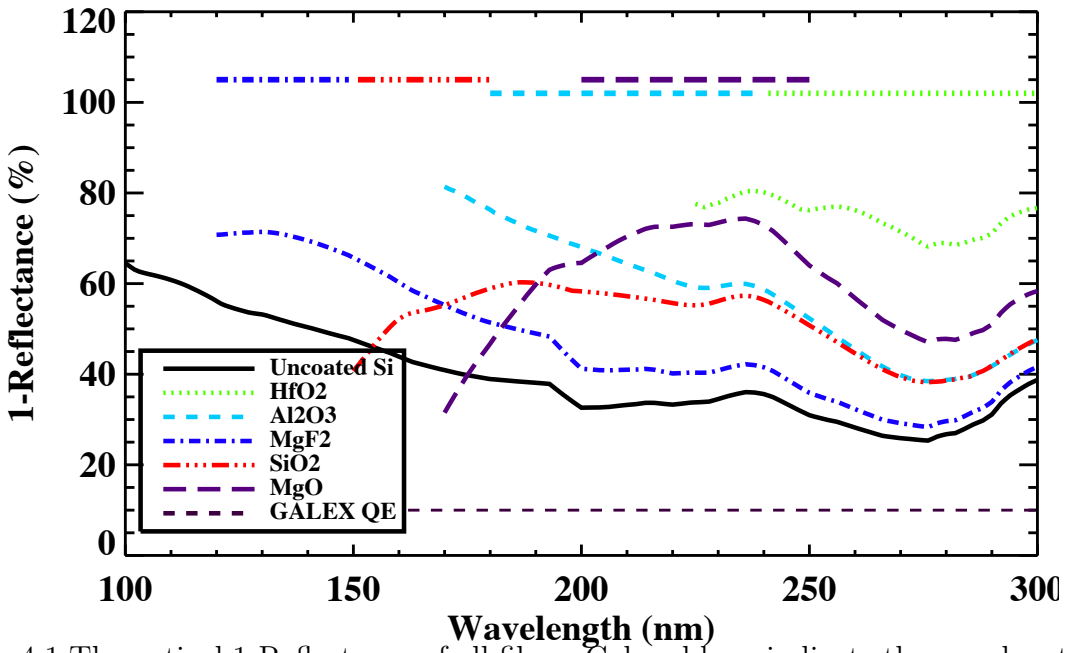

Figure 4.1 Theoretical 1-Reflectance of all films. Colored bars indicate the wavelength range over which each material is being considered. The dashed line at the bottom represents the average QE of the GALEX micro-channel plate detector.

of HfO_2, and Al_2O_3. All films were grown on 1" $\langle 100 \rangle$ P/B 1-20 Ohm-cm single-side polished wafers of Si, as a proxy for the actual device. The thickness of each material has been selected to minimize reflectance in a specific wavelength range. Calculations of predicted reflectance were done using the TFcalc^{TM} software package, with a bare Si substrate and are shown in Figure 4.1, along with the current average QE of the GALEX UV space telescope.

The thickness of the model film was varied until a minimum of losses (reflectance back to the observer plus absorption) was achieved in the target wavelength range. Contour plots showing potential transmission percentage as a function of wavelength and thickness are shown for each film in Figures 4.2 through 4.6. Each plot shows contours of 50-80 percent potential transmission, given a range of thicknesses. A dark vertical line on the plot indicates the absorption edge. This edge marks the region where absorption begins to increase rapidly

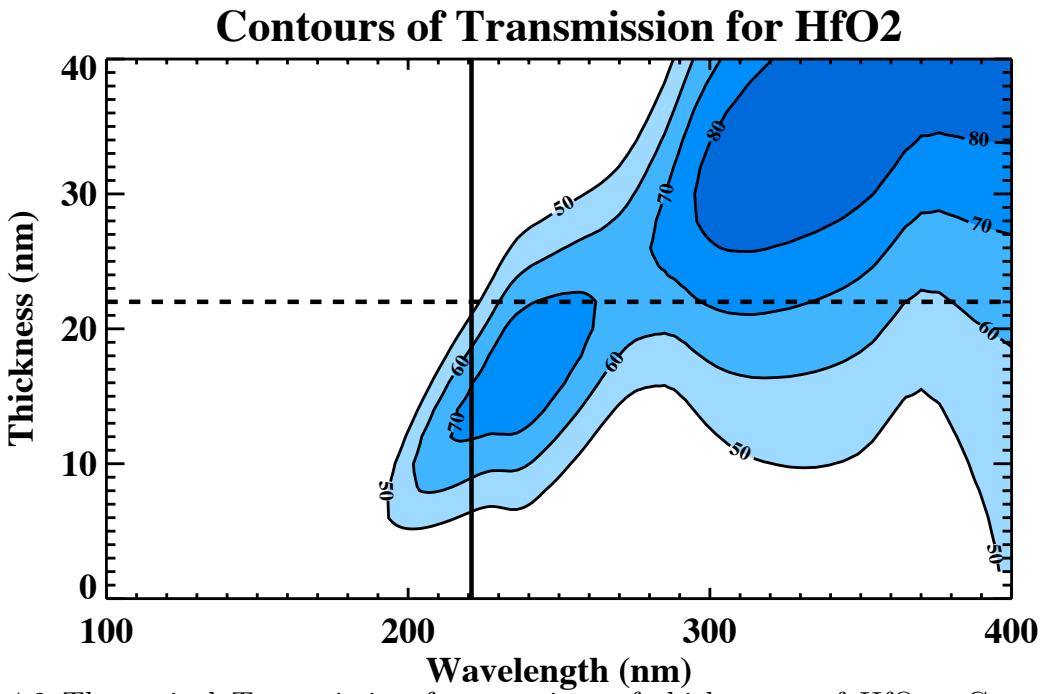

Figure 4.2 Theoretical Transmission for a variety of thicknesses of HfO_2. Contour lines begin at 50 percent transmission and increase in increments of 10 percent. Horizontal line indicates thickness target. Vertical line indicates absorption edge. Absorption increases rapidly as wavelength decreases.

as wavelength decreases; generally this fast increase begins when absorption has reached 10-20%. Thus anything to the right of the line indicates wavelengths where absorption is not a primary concern.

Thicknesses which provided close to peak transmission while also maintaining a wide range above 50 percent were selected. The reflectance that corresponded to this thickness was then used as a target during testing. We sought to make a range of film thickness that were centered around this target. Typically we tested several films that varried in thickness between 5-10nm above and below the target. There are several published indices of refraction for the Si substrate, which contributes to some uncertainty in the predicted reflectance. The indices of refraction for all materials were taken from Palik ((Palik 1985), (Palik 1991)), except for HfO_2, which came from Zukic (Zukic et al. 1990). An alternative

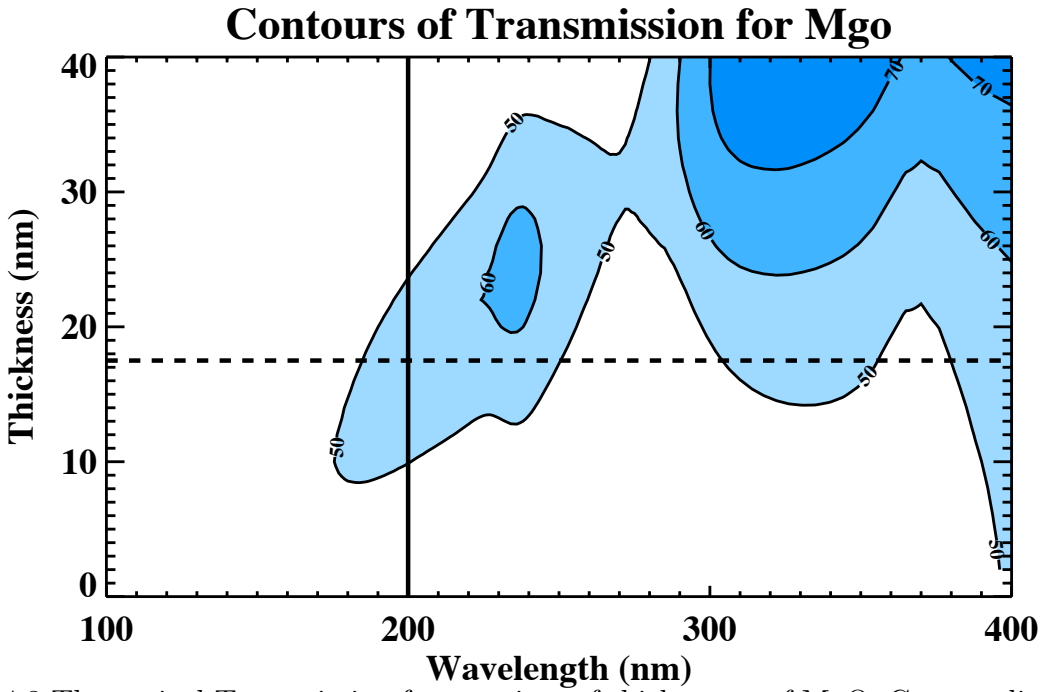

Figure 4.3 Theoretical Transmission for a variety of thicknesses of MgO. Contour lines begin at 50 percent transmission and increase in increments of 10 percent. Horizontal line indicates thickness target. Vertical line indicates absorptionedge. Absorption increases rapidly as wavelength decreases.

Wavelength Range (nm)	Material	Modeled ideal thickness (nm)	Best thickness based on reflectance test (nm)
240-300	HfO_2	22	25
200-250	MgO	17.5	20
180-240	Al_2O_3	10	16
150-180	SiO_2	15	19
120-150	MgF_2	7	11
120-150	MgF_2	13	11

Table 4.1 Targeted thickness and best actual thickness after reflectance measurements for all films

index of refraction for Si was also consulted, taken from Philipp (Philipp & Taft 1960). The Philipp values differed at the shortest wavelengths (below 150nm) and predicted a lower reflectance than the Palik values.

All RF Sputtered depositions were made using 15 sccm of argon gas flowing into the deposition chamber kept at a pressure of 25 mTorr during sputtering. Deposition times varied

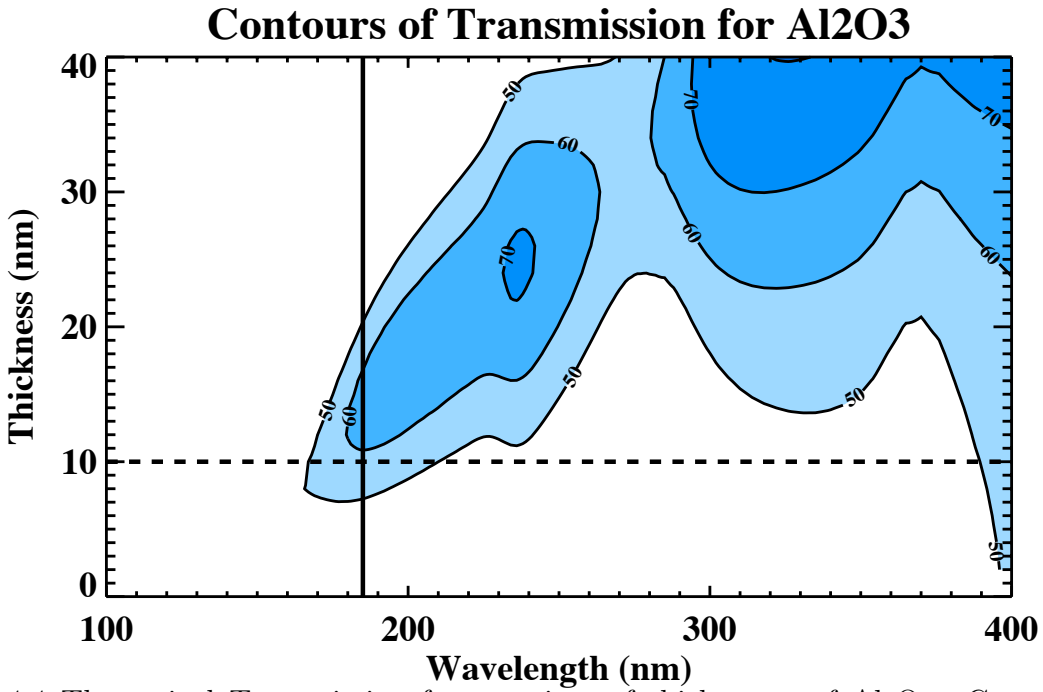

Figure 4.4 Theoretical Transmission for a variety of thicknesses of Al_2O_3. Contour lines begin at 50 percent transmission and increase in increments of 10 percent. Horizontal line indicates thickness target. Vertical line indicates absorption edge. Absorption increases rapidly as wavelength decreases.

for each material and between runs. Deposition rates were calculated based on the measured thickness of a witness sample and the time of deposition. All targets were conditioned for 3 minutes before sputtering began. The substrate temperature for all runs was 17° Celsius, except for so called "hot runs", which maintained a temperature of 180° Celsius. In these cases, a 5 minute "soak" time was added to ensure the substrate reached equilibrium at deposition temperature. SiO_2, MgO, and Al_2O_3 were deposited at a power of 480 W (80% of maximum), while HfO_2 was deposited at 252 W (42% of maximum).

Thermal evaporation was conducted at pressures of 10^{-7} Torr. Deposition rates for each run varied between 1 and 4 Å/sec. A crystal monitor displayed thickness and an automatic shutter closed when the desired thickness was reached. There was some discrepancy between the monitor thickness and the actual thickness due to a tilt in the substrate holder.

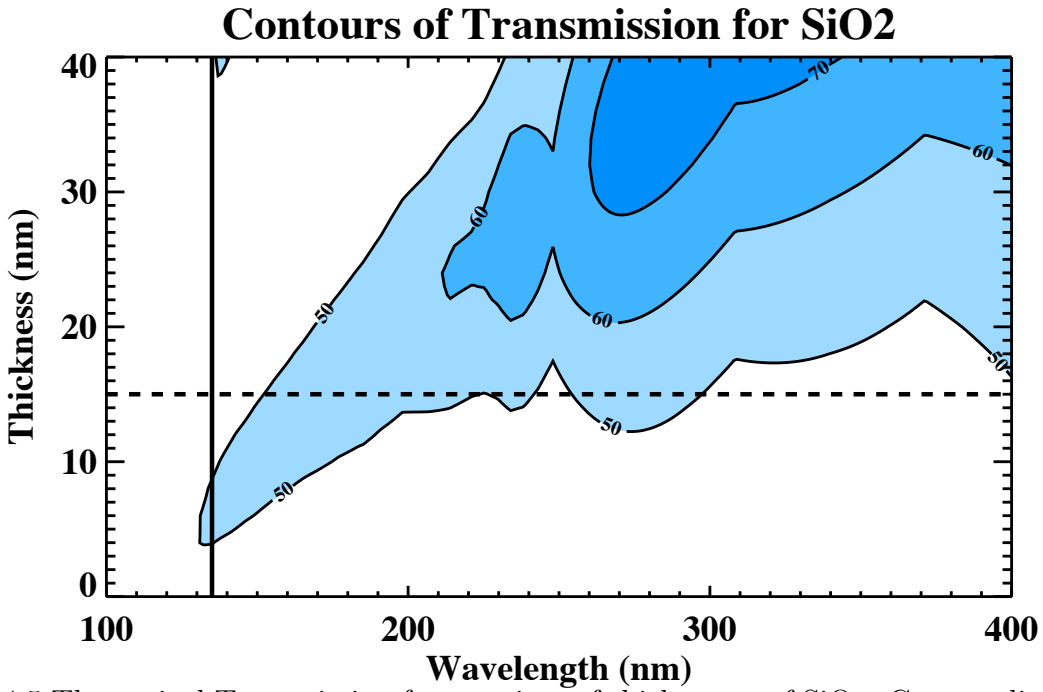

Figure 4.5 Theoretical Transmission for a variety of thicknesses of SiO_2. Contour lines begin at 50 percent transmission and increase in increments of 10 percent. Horizontal line indicates thickness target. Vertical line indicates absorption edge. Absorption increases rapidly as wavelength decreases.

Compensation was made for this discrepancy.

ALD deposition can be performed using either a plasma or a thermal recipe. The deposition of HfO_2 was performed using a plasma recipe nominally at 250° C, while Al_2O_3 was deposited also using a plasma, but one nominally at 300° C. Plasma ALD deposition recipes developed here were informed by the work of Goldstein, 2008 (Goldstein et al. 2008) for Al_2O_3 and Lui, 2005 (Liu et al. 2005) for HfO_2.

Layers were deposited as close to the selected thickness as could be made, given variations in deposition rate from run to run, and the thickness was verified in an ellipsometer. Precision of the thickness measurement was 0.1nm.

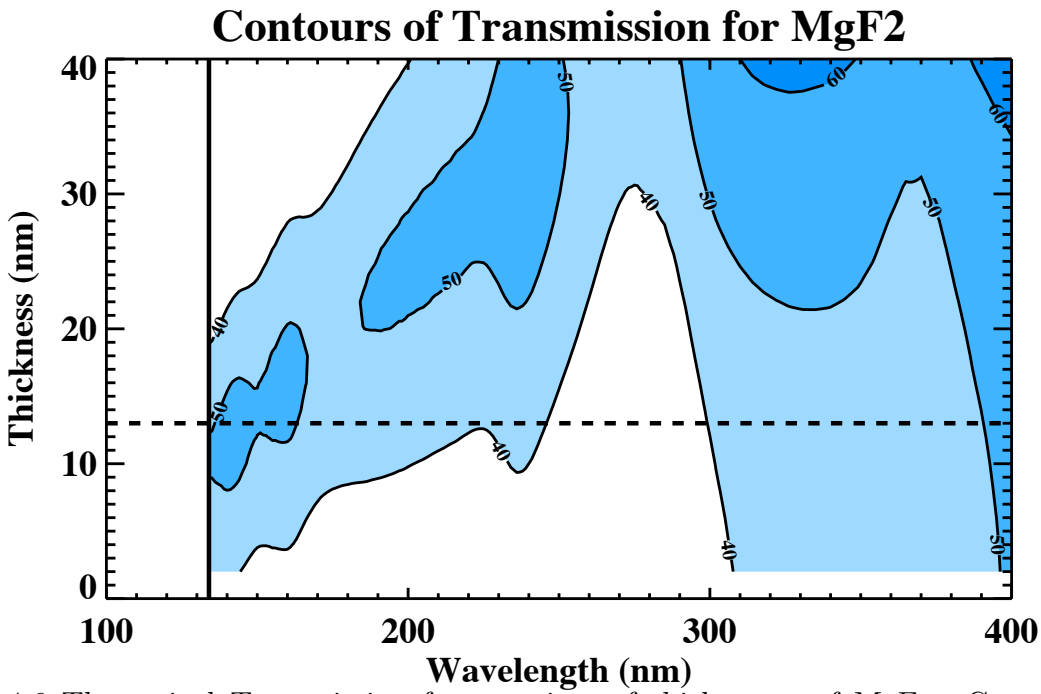

Figure 4.6 Theoretical Transmission for a variety of thicknesses of MgF_2. Contour lines begin at 40 percent transmission and increase in increments of 10 percent. Horizontal line indicates thickness target. Vertical line indicates absorption edge. Absorption increases rapidly as wavelength decreases.

4.3 Testing

All samples were tested at Columbia University in a reflectance setup. The samples were placed in a chamber maintained at less than 1×10^{-3} torr for the duration of the measurement. An Acton monochrometer fed by a focused deuterium lamp stepped through wavelengths from 100nm to 300nm in steps of 5nm to 15nm, depending on the testing run. The light reflecting off of the samples was detected by a Princeton/Acton CCD during exposures of 115 to 180 seconds, again depending on the run. The resulting images were then dark subtracted, and the counts from the illuminated area extracted. An Acton H1900-FS-1D standard and an uncoated bare Si wafer were used to calibrate each set of measurements. Figure 4.7 shows the measured (Acton) and predicted (Si) 1-Reflectance percentage of both over the relevant

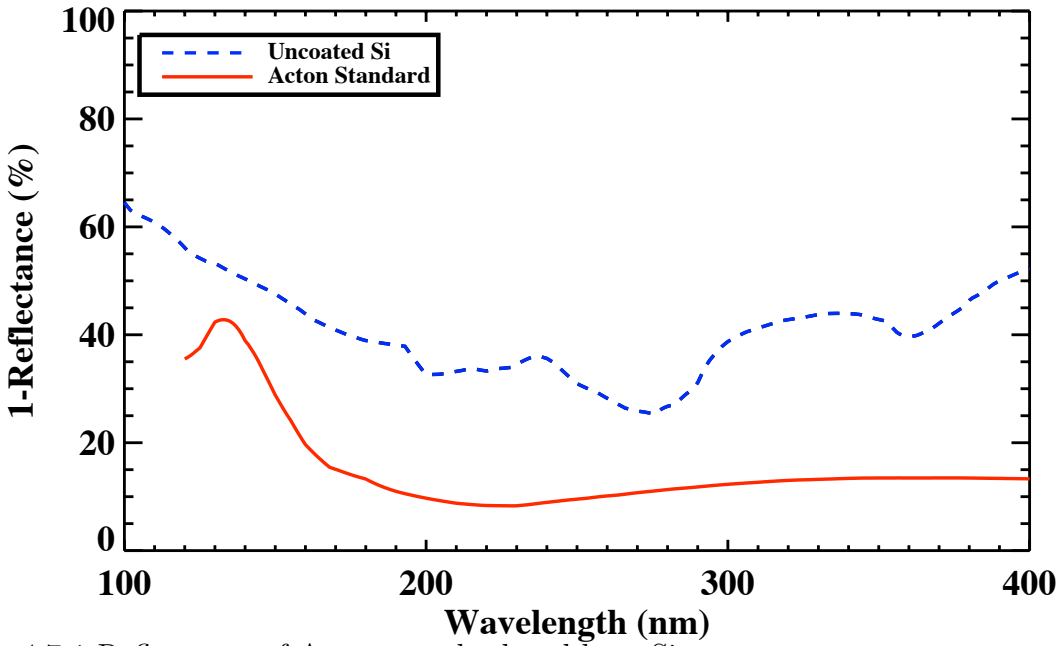

Figure 4.7 1-Reflectance of Acton standard and bare Si.

wavelength range.

Films were also sent out for testing by the J.A. Woollam company. They provided thickness measurements and measures of the optical indices down to 137nm in a vacuum ellipsometer for single samples of HfO_2 (both sputtered and ALD), MgO, Al_2O_3, and MgF_2. The returned values confirmed the expected behavior of all films, except HfO_2. We found the index of refraction below 250nm was much higher than that measured (Zukic et al. 1990) (maximum difference of 30%). Values for k were as expected. We have plans to further test this result.

4.3.1 Results

After comparing the reflectance of different thicknesses of the same material, a best fit layer thickness was selected. This best fit for each material (listed in Table 4.1) depended on

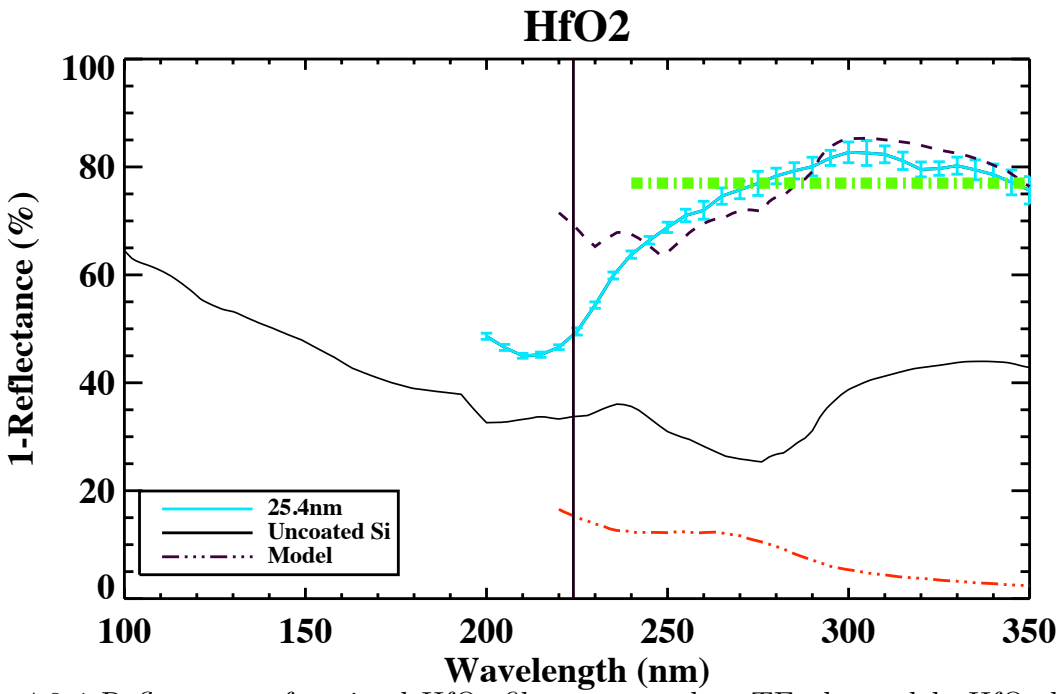

Figure 4.8 1-Reflectance of optimal HfO_2 film compared to TFcalc model. HfO_2 has been optimized for 240-300 nm. The solid vertical line indicates the absorption edge. The red dot-dashed line shows the corresponding absorption percentage.

how well the layer minimized reflectance over the wavelength range in question, as well as an adherence to the predicted behavior of the reflectance curve. We were able to achieve predicted behavior in almost all of the wavelength ranges, with the exception of SiO_2. The results of the initial tests are presented in Figures 4.8 through 4.12. Figures are plotted in terms of 1-Reflectance, which over the wavelengths of interest is a proxy for Transmittance. A vertical solid line passes through the figure at the point at which absorption reaches 10%. At wavelengths lower than the line, absorption grows rapidly and we assume the bulk of diminished reflectance is due to absorption and not transmission. For the sake of clarity, we present 1-Reflectance for only our best fit thickness.

Further tests were done to ensure reliability. Two to three films were made for each material with the same deposition process as the best fit film. Two things were tested here:

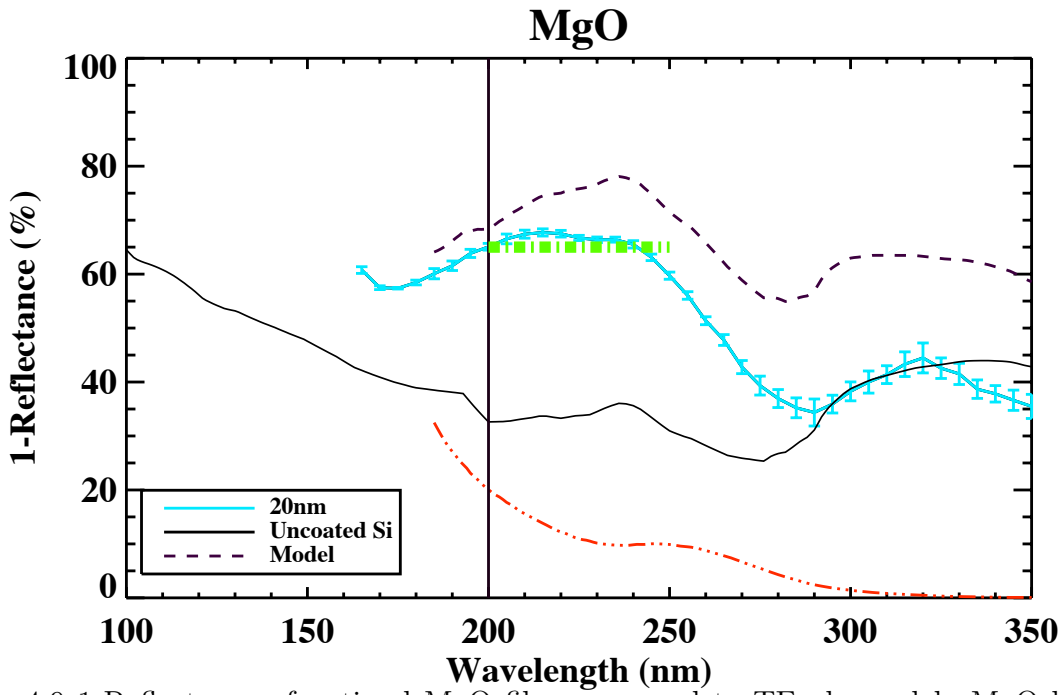

Figure 4.9 1-Reflectance of optimal MgO film compared to TFcalc model. MgO has been optimized for 200-250nm. The solid vertical line indicates the absorption edge. The red dot-dashed line shows the corresponding absorption percentage.

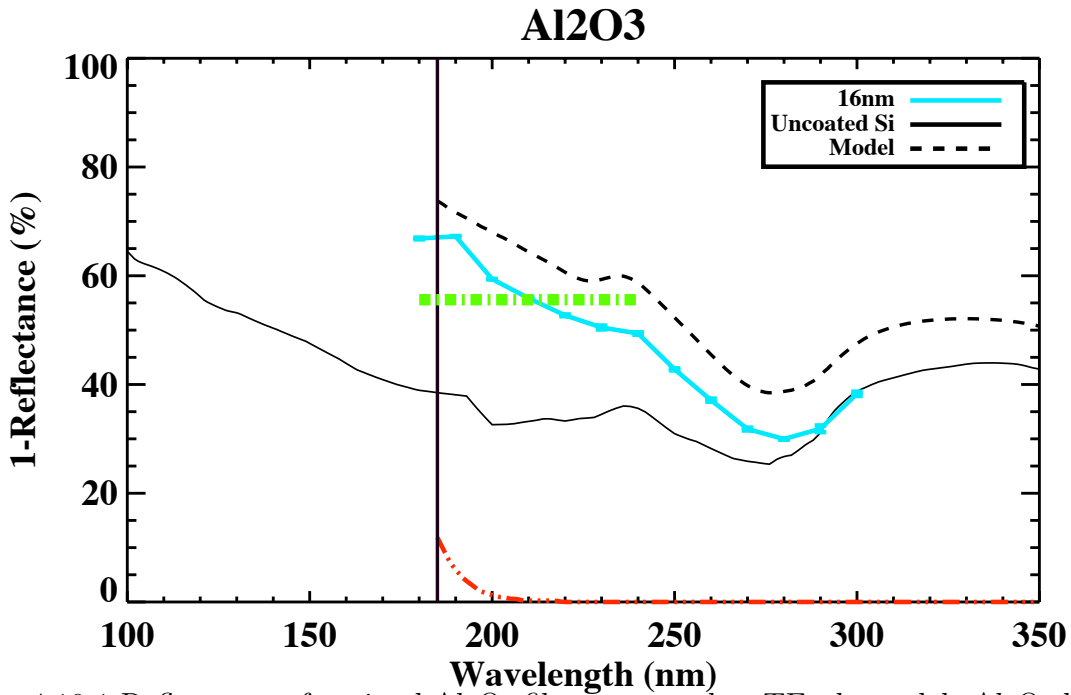

Figure 4.10 1-Reflectance of optimal Al_2O_3 film compared to TFcalc model. Al_2O_3 has been optimized for 180-240 nm. The solid vertical line indicates the absorption edge. The red dot-dashed line shows the corresponding absorption percentage.

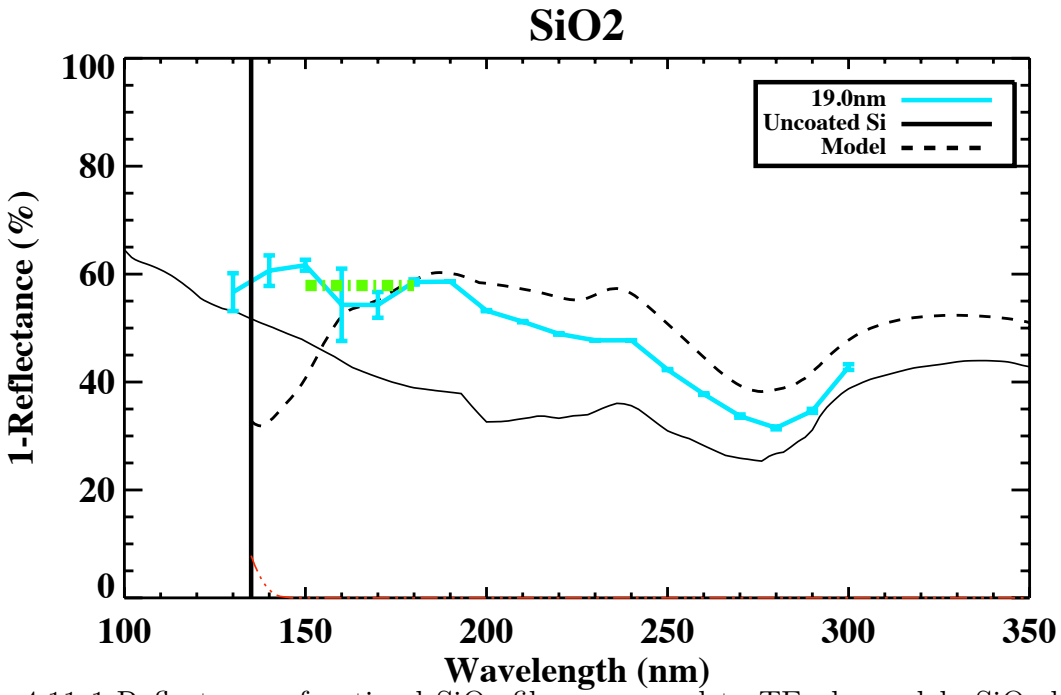

Figure 4.11 1-Reflectance of optimal SiO_2 film compared to TFcalc model. SiO_2 has been optimized for 150-180 nm. The solid vertical line indicates the absorption edge. The red dot-dashed line shows the corresponding absorption percentage.

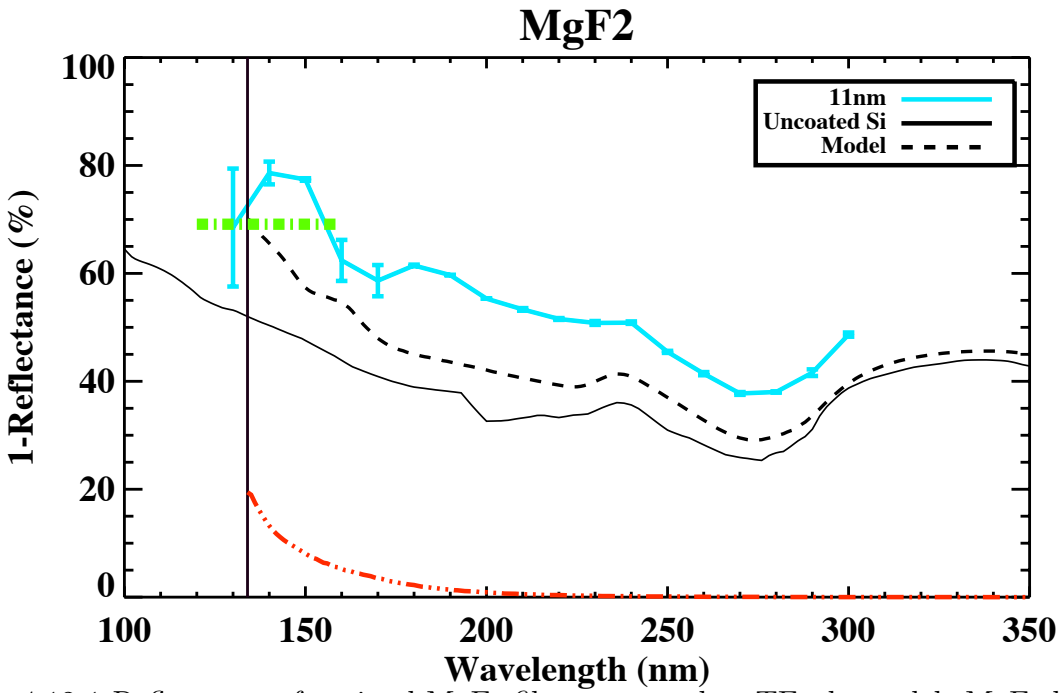

Figure 4.12 1-Reflectance of optimal MgF_2 film compared to TFcalc model. MgF_2 has been optimized for 120-150 nm. The solid vertical line indicates the absorption edge. The red dot-dashed line shows the corresponding absorption percentage.

the repeatability of the deposition procedure and consistency of performance from sample to sample. Deposition of all have proven to be quite repeatable (thicknesses vary by 1 nm from target) and are especially repeatable for ALD depositions. The values for reflectance are also consistent across samples of the same material.

Materials deposited using ALD, as opposed to sputtering, appear to produce better films. The thickness of the film is easier to control and the quality of the layer (as judged by how close the index of refraction at 500nm is to the bulk index) was consistently higher. Furthermore, on tests with live delta-doped devices, sputtering caused a variety of problems. We believe interactions of the film material with the surface Si created highly absorptive silicates. As such, our later work has used ALD exclusively for HfO_2 and Al_2O_3. We plan to transition to ALD for MgO and SiO_2 once the necessary precursors have been obtained. A forthcoming paper will discuss in more detail the comparisons between films made by ALD and sputtering (Greer et al. 2013).

AR coating films have shown good stability thus far and long term stability tests are underway, to be reported separately. Tests remain to determine the feasibility of applying different non-overlapping layers to the same CCD. Figure 4.13 depicts the overall outlook for multiple coatings on a single CCD. Each film is shown over the wavelength range of interest. The solid bar is an average of the reflectance values over that range. This provides an encouraging outlook for a future detector.

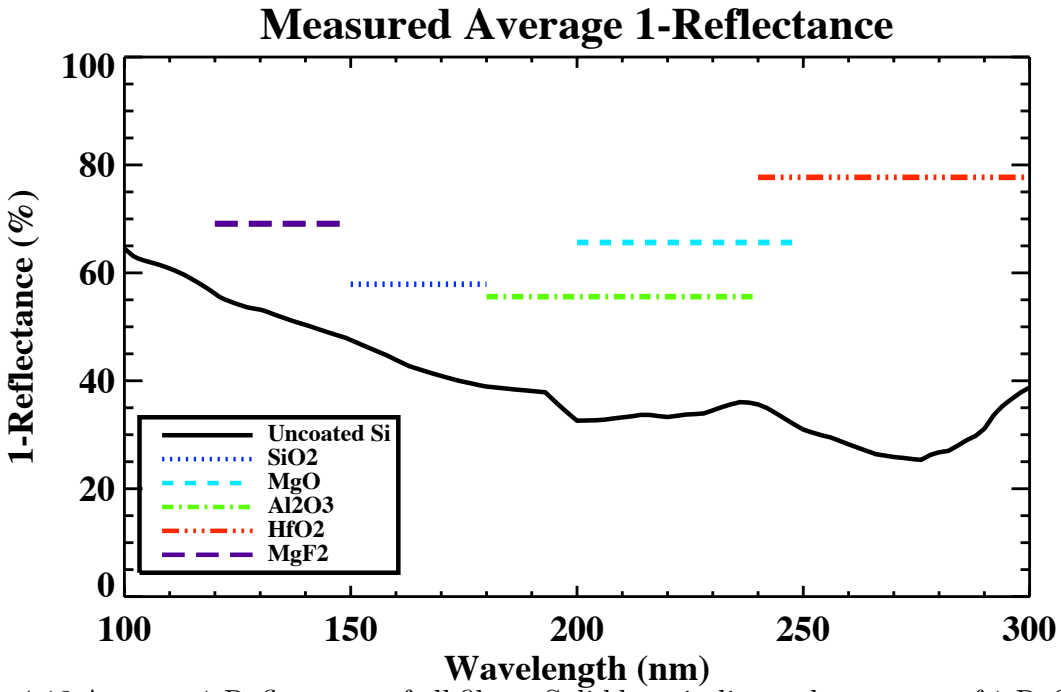

Figure 4.13 Average 1-Reflectance of all films. Solid bars indicate the average of 1-Reflectance over the wavelength range of interest for each material.

4.4 Testing on Live Devices

Our team has applied the films discussed above to thinned and delta-doped CCDs. Work on this is ongoing and another publication describes our results in detail, but it merits a short mention here.

The procedure for thinning and delta-doping, as described in Hoenk, (Hoenk et al. 2009), was carried out in the MicroDevices Lab at JPL on both Cassini CCDs and Electron Multiplying CCDs (EMCCDs) (Mackay et al. 2001). The standard n-channel CCDs used have 1024 square arrays and 12 micron pixels (Porco et al. 2004). The EMCCDs are 1024 by 512 rectangular arrays, with 16 micron pixels. EMCCDs are an advancement in CCD technology which enables low-noise photon-counting. These were first developed at e2v (formally Marconi), and sport a high internal gain before readout, which allows sub electron

read noise levels. The advantages for registering single photon events are obvious (Gach et al. 2004), and when combined with a high QE from a thinned, delta-doped, and AR coated CCD, we expect to dramatically improve the minimum signal detector threshold.

For each test, a single film is applied to a thinned and delta-doped device. Devices were then wire-bonded and packaged for testing. A measurement set-up for finding absolute QEs was developed using JPL's Vacuum UV Characterization setup (a detailed description of characterization system and methods of measurements are described in a separate paper (Jacquot et al. 2011) and used for measuring the effectiveness of each film type. The testing chamber steps through wavelengths from Lyman-α into the infrared, illuminating the CCD. A NIST-calibrated Si photodiode provides a standard at each wavelength. A region of interest was selected, and QE was calculated from the counts in each region after correcting for bias levels and comparing flux levels to the standard photodiode. The conversion gain (E/DN) is determined by a photon transfer curve.

Films made with RF sputtering failed to increase QE, and in some cases caused worse performance. Tests of RF sputtering with HfO_2 on silicon substrates showed the formation of an absorbing, interstitial silicate layer. This layer reduced the QE significantly and likely formed as a result of the high energy of the sputtering process. ALD and Thermal Evaporated films all performed well. Using parameters from the literature we have achieved qualitative agreement between our measured QE and the expected value. In films where we characterized the indices, we achieved more close agreement between modeling and experiments. More work is underway to complete the analysis. Nevertheless, we have been able to achieve greater than 50% QE over the range of interest in the four bands described previously.

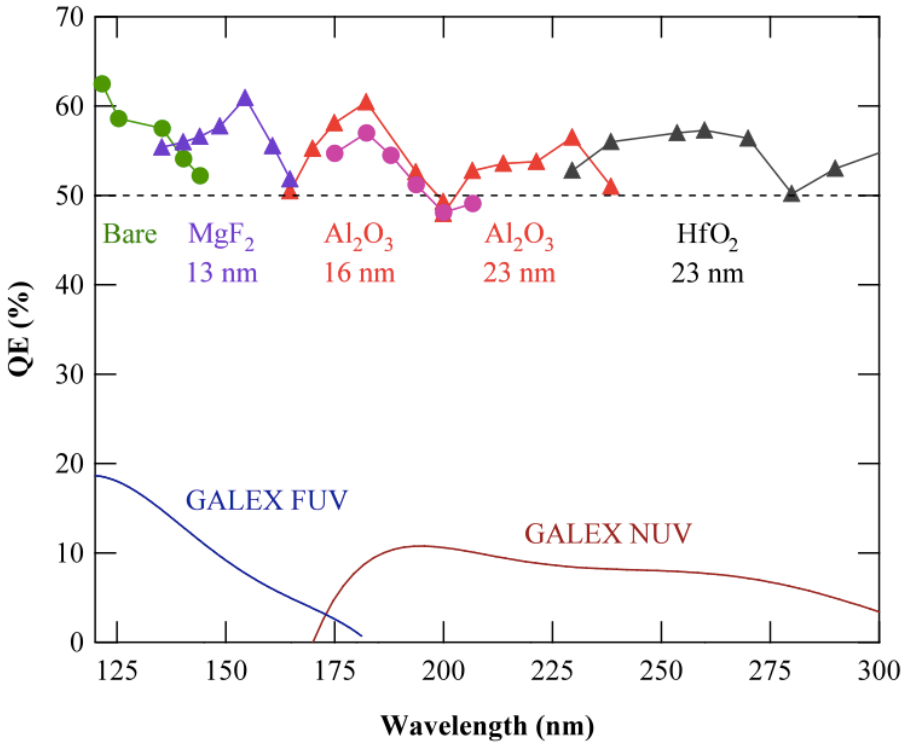

Figure 4.14 QE measurements for 4 single layer coatings applied to delta-doped CCDs. Each coating was applied to a single layer and is shown over the band of interest. MgF_2 (13nm) was grown using thermal evaporation, while the other coatings were made using ALD. An EMCCD was used to test the 16nm AL_2O_3 film, proving the functionality of these coatings on EMCCDs.

Figure 4.14 shows results as published in (Nikzad et al. 2012).

4.5 Future Applications

4.5.1 Applications in astronomy

Astronomical uses for these new devices will no doubt go beyond the few we have imagined here, as more work is done on these and other materials. The most immediate use we envision would be on a space, balloon, or rocket borne experiment in which the device is

fed by an Integral Field Unit (IFU) and will cover a wavelength range of 120-300nm. This would allow imaging and spectroscopy beyond the frontiers created by GALEX and HST, in a wider range of wavelengths and at much lower integration times for similar information. The use of an EMCCD would allow observations of the faintest regions of the intergalactic medium, and could provide an important view into the history of the Universe. Additionally, an EMCCD can operate in non-multiplying mode and observe bright objects without count rate limits. The large dynamic range accessible to an EMCCD (photon-counting multiplying mode and normal operation) can be extremely valuable for achieving a wider range of scientific objectives in a future mission.

Beyond an IFU covering a wide wavelength range, these coatings can be tuned to any variety of specific medium bands. An AR-coating is already in use on WFPC3, providing QE in the NUV and optical (Baggett et al. 2010). The coverage of a whole device in a thick layer of Al2O3 (23nm), for instance, would create an imager optimized for 200-250nm. HfO_2, already well known as an AR-coating in the optical, could similarly be useful in a near UV and optical imager. MgO and MgF_2, along with other as of yet untested materials, may also prove useful in specific instances. We plan to test more films and thicknesses on live devices to get a better idea of the potential range of uses.

4.5.2 Multi-layer and Graded Coatings

Thus far we have only discussed the effects of single films. One may also create narrow-band filters in the UV using these coatings. As is well known, multi-layer coatings with alternating layers of high and low index material can provide even better transmission than a single film

AR coating ((Flint 1982), (Haelbich & Kunz 1976), (Spiller 1972)). A highly tuned multi-layer, while being less broadly applicable, can provide a bandpass of high transmission over a short wavelength range. A multi-layer film using alternating layers of LaF_3 and MgF_2 is one such easily created design. These multi-layers could be optimized to create a bandpass around 200nm, taking advantage of an atmospheric window best exploited by balloon experiments (Huffman et al. 1980). This bandpass would have higher transmission than a single layer of MgO or Al_2O_3, but would be much narrower in wavelength. This particular example is ideal for looking at red-shifted Lyman-α and certain red-shifted metal lines while taking advantage of the very low sky background found in the UV (Tuttle et al. 2008), but coatings can be optimized for nearly any desired wavelength and observational purpose. Figure 4.15 shows an example of the high, but peaked, transmission that can be achieved with a multilayer film. LaF_3 and Al_2O_3 are used in sequence and with different thicknesses in each layer. There are 5 layers all together, starting and ending with Al_2O_3.

In our work so far, we have tried to achieve high QE across a wide wavelength range by using several different films, each with a specific thickness. Each film, while not being a true broadband coating, still provides coverage over many tens of nanometers. Taking this method one step further, one could create a series of many very sharply peaked narrow-band films, and similarly tile them across a device. Each would provide higher QE than the films described in previous sections, but only over a range of a few nanometers. This creates technological challenges in applying these films over a small area and in close proximity. One alternative to this would be to create a graded or ramped coating such that the thickness changes quickly enough to provide high QE without changing film materials. A wedge shaped

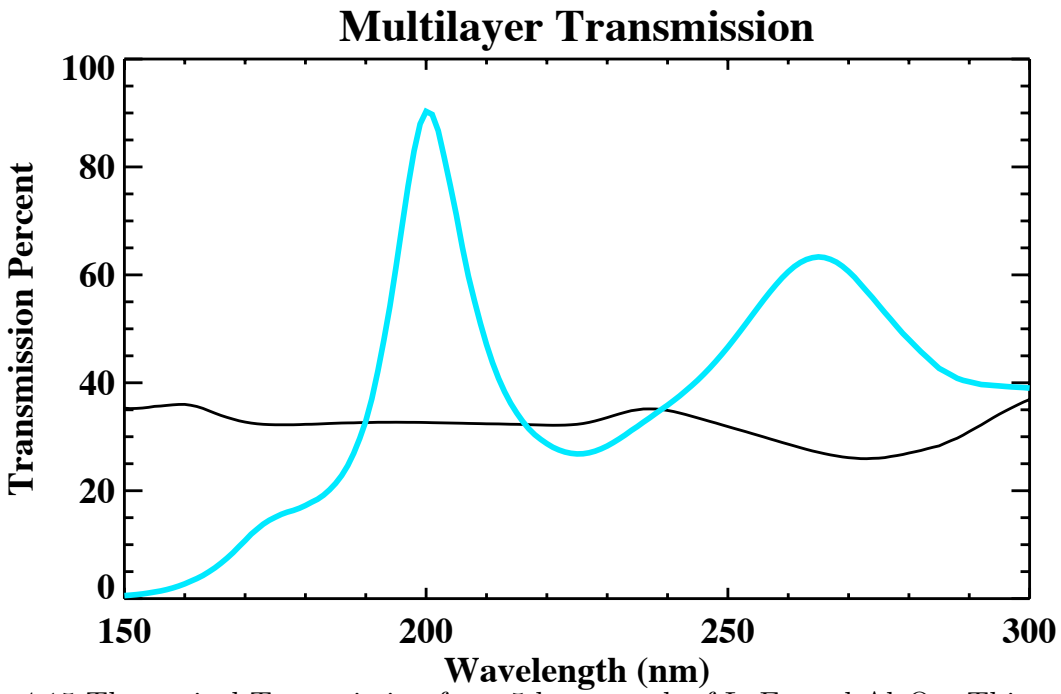

Figure 4.15 Theoretical Transmission for a 5 layer stack of LaF_3 and Al_2O_3. This particular multilayer is optimized to maximize transmission around 200nm. 1-Reflectance of Si is shown as solid black line.

film (thin at low wavelengths and thicker at high) would eliminate the need to change from one material type to another, and provide a way to reach a consistently high QE across the whole band instead of just one peak. This ramp would also prevent the creation of low QE 'seams', where two films meet.

One example of a potential ramp is found in Figure 4.16. The modeled coating is 5 layers of alternating Al_2O_3 and LaF_3. While the ratios between the layers remain roughly static, the overall thickness of the stack increases as one optimizes for higher wavelengths. By starting at one edge of the device with a coating optimized for 180nm and increasing all thicknesses until the coating is optimized for 350nm, for example, one can create a device with high QE across all wavelengths. The material combinations for this type of design are dependent on what ranges one hopes to target, and are somewhat constrained by deposition

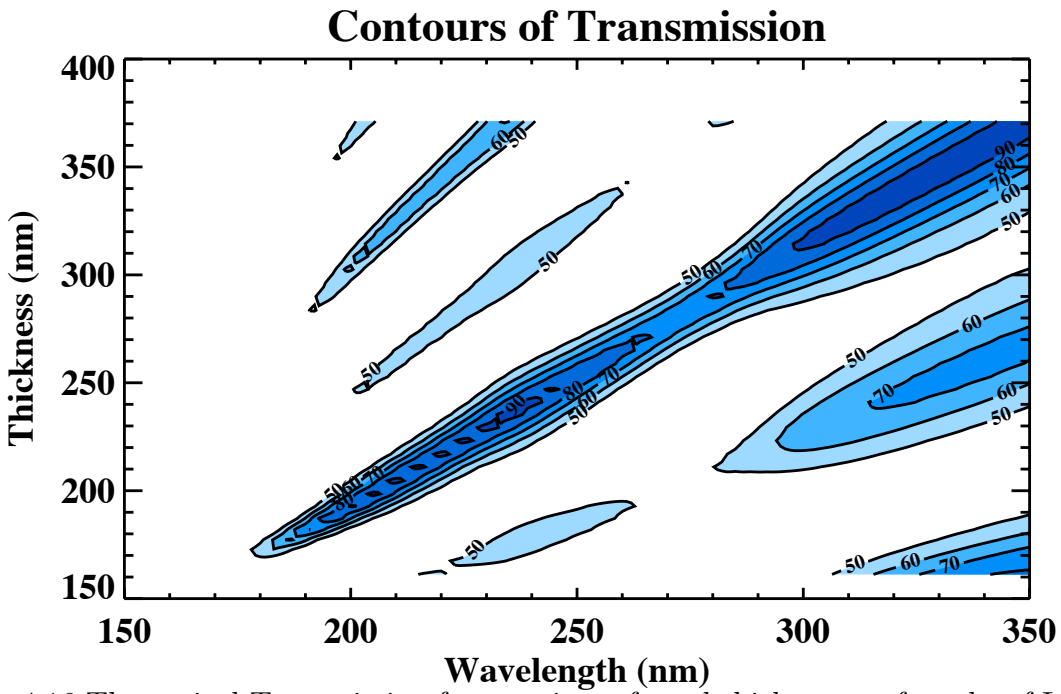

Figure 4.16 Theoretical Transmission for a variety of total thicknesses of stacks of LaF_3 and Al_3O_3. The 5-layer stacks are varied to achieve high QE in a narrow range. A film that was graded to follow the highest contours could achieve between 75 and 95 percent transmission across a large wavelength range.

techniques, but on the whole this represents a way to achieve numerous goals in high QE coatings.

4.5.3 Red Rejection

A common difficulty in UV spectroscopy is adequate red rejection. All of the AR coatings we have discussed above provide a boost in transmission in the UV, but at longer wavelengths has very little effect. Thus at the red end, the CCD should behave as an uncoated delta-doped device and be very responsive. Any optical assembly which seeks to use these devices will need to ensure that stray light of other wavelengths does not reach the CCD. The high QE over a wide range of wavelengths longer than the UV means this is a particularly

important issue to note. Filters, combined with a careful selection of reflective gratings, should minimize red leak, although characterization of the total leak into the device on the final optical assembly will be essential. We may also explore filters that simultaneously reflect undesired optical bands and transmit effectively in the UV.

4.5.4 Applications in other fields

While our expertise remains in astronomical and scientific applications, the uses of a high quality imager over the entire UV wavelength range will be considerable. The devices are relatively easy to manufacture on an industrial scale, especially when compared with MCPs. One immediate application is in small scale modular fixed spectrographs. A variety of these are made by Ocean Optics (USB2000 series), StellarNet (EPP2000), and other companies. Judicious use of AR-coatings for these modular spectrographs will immediately and easily improve performance. VUV spectrographs from Acton/PI and McPherson and VUV ellipsometers from J.A.Woollam, among others, can also see similar improvements. Instruments which already utilize spectrometers to identify chemicals in the fields of medical imaging, defense, materials analysis, and chemical testing can also take advantage of the coatings presented here.

Any potential uses one might imagine are immediately bolstered by the increased QE that these devices will provide. From an astronomical perspective, a boost in QE from delta-doping and AR coating, combined with a decrease in the noise level from an EMCCD, will result in two advantages. The first is a lowering of detection limits, allowing deeper images of fainter objects. The second is a cost savings on future missions. A smaller primary

mirror could be used while still achieving great scientific gains and lowering the overall costs of getting a mission into the upper atmosphere or orbit. Recent developments in creating low noise CMOS detectors mean our AR coatings may also be useful in this brand of UV detector development (Fowler et al. 2010) and recent work by JPL has shown the utility of delta-doping and AR coatings on CMOS devices (Hoenk et al. 2009). In other fields, using relatively easy to manufacture silicon detectors in place of MCPs or other more construction-demanding devices will also provide a savings in cost, design, and ease of use.

4.6 Acknowledgements

The research described here was funded in part by a NASA Space Grant. The research described in this paper was carried out in part at the Jet Propulsion Laboratory, California Institute of Technology, under a contract with the National Aeronautics and Space Administration. The research here was supported in part by internal funding from Columbia University.

The authors wish to thank Blake Jacquot, Todd Jones, and Patrick Morrissey for their help and advice in the writing of this paper.

Chapter 5

CCD detectors with high QE at UV wavelengths[1]

5.1 Introduction

Anti-reflection (AR) coatings have been used in a wide range of applications to increase transmission through a surface, including on CCDs at visible and near UV wavelengths. While CCDs have traditionally not been effective in most parts of the UV (100-350 nm), different treatments have been developed solve this problem. Backside illumination and delta doping, a process developed at JPL, can bring the quantum efficiency (QE) of treated devices up to the reflection limit of silicon at all wavelengths in a stable and consistent way (Hoenk et al. 1992; Nikzad et al. 1994; Hoenk et al. 2013); in the UV this brings the QE to around 30%. These CCDs have 100% internal quantum efficiency, limited only by reflection from

[1]This chapter is a slightly edited version of paper currently in preparation. The full author list for this article is: Hamden, Erika T.; Jewell, April D.; Goodsall, Tim M.; Hennessy, John; Nikzad, Shouleh; Hoenk, Michael; Jones, Todd; Greer, Frank; Gordon, Samuel; Schiminovich, David; Martin, D. Christopher.

the surface. Thus the QE can be increased beyond the reflection limit with the application of a suitable AR coating. Our initial work on single layer AR coatings at UV wavelengths has been successful at increasing QE to greater than 50% from 135 nm and longer (Hamden et al. 2011; Nikzad et al. 2012) using in part high quality coatings made possible by atomic layer deposition (ALD) (Greer et al. 2013). The high QE achieved with these single-layer AR coatings can be further improved with more complex designs.

Single layer coatings are often used to simply boost transmission over specific wavelength ranges in the visible (e.g. HfO_2 for increased blue sensitivity). For more complex applications and higher transmission, quarter wave stacks and other configurations will minimize reflectance to nearly zero over a limited range of wavelengths and have been well explored in the visible (MacLeod 1986). These multi-layer techniques can be extended to UV wavelengths, but are constrained by both the limited range of UV-transmissive materials and the changing index of refraction of silicon (varying from 0.5 to 6.0 between 100 nm and 350 nm). Further complicating matters is the trade-off between achieving a high QE through the use of multi-layers versus the potential for increased absorption as the overall film thickness grows. Here we model multi-layer films using the computer program TFCalc^{TM} (Software Spectra, Inc.).

Our first test multi-layers have focused on models centered near 200 nm. This wavelength was selected since it is the location of an atmospheric window between O_2 and O_3 absorption bands Brewer & Wilson (1965), which allows for observation in the UV at balloon altitudes ($\sim$ 35 km). A balloon experiment, the Faint Intergalactic Redshifted Experiment Balloon (FIREBall) Tuttle et al. (2008), is just such a mission. This experiment is funded

for a third launch, and is an ideal test bed for a delta-doped AR-coated CCD. With this in mind, we have selected a model design optimized for 205 nm as a first test of a very high QE multi-layer.

NASA's Jet Propulsion Laboratory (JPL), California Institute of Technology, has had great success in their development of delta-doping technology. This technique passivates the back surface of a thinned silicon CCD, CMOS, or PIN array and results in nearly 100% internal QE from the extreme UV to the IR (Hoenk et al. 1992). The shallow absorption depth of UV photons in silicon (< 10 nm) requires the use of both back-illuminated and thinned CCDs, to avoid both absorption in the front-side circuitry and recombination loses in the backside surface layer (Crowell et al. 1967). Despite these precautions, traps will form in the surface layer between Si-SiO_2, interacting with the shallowly generated charges, causing poor QE, hysteresis, and high dark current (Janesick et al. 1989). The insertion of a single atomic layer of heavily doped silicon, deposited using molecular beam epitaxy and capped with pure silicon, passivates the surface layer. This delta-doped layer eliminates traps and allows for stable and efficient charge collection within the CCD (Nikzad et al. 1994). While this procedure modifies the internal electric field of the device, the surface itself remains as silicon and its native oxide. Thus we can create AR coatings optimized for this simple starting surface.

In Section 5.2, we describe techniques for model creation and the model selected for deposition. In Section 5.3, we describe deposition recipes and techniques, along with growth rates for each material. In Section 5.4, we describe the reflectance and transmission measurements of the films on inert substrates. In Section 5.5 we describe deposition, testing and

results of a film grown on a delta-doped CCD.

5.2 Model Development

Multi-layer films were modeled using TFcalc. Materials under consideration include MgO, MgF_2, Al_2O_3, SiO_2, and HfO_2. For uses below 220 nm, we eliminate HfO_2 as a viable film layer due to absorption. Optical constants come from (Palik 1985, 1991), although in some cases constants used are from samples made at JPL and measured by J.A. Woollam using vacuum ellipsometry. We list these constants in the Appendix. Variation in the values for n,k was found for HfO_2 at UV wavelengths compared to those listed by Zukic et al. (1990).

The models are designed to fit several requirements. The primary requirement is a low reflectance (<20%) at 205 nm, with a band-pass of at least 15 nm. Typical FWHM for band-passes are less useful here since the out of band QE is not zero, but typically closer to the reflectance limit of silicon. Therefore, we will use the bandwidth at 50% to set a standard for comparison between film models in this paper. Larger band-passes than 15 nm are acceptable, since atmospheric transmission drops precipitously between 235 and 280nm, but minimizing out of band light between 210 and 235 nm is desirable. Secondary requirements are low absorption between 200 and 210 nm (> 5%). These requirements combine to yield an overall QE of >75% in the band-pass. We discuss further steps to reduce out of band light in Sections 6.2 and 6.4.1, but for these models we focus only on maximizing QE in the band-pass.

One thing to note is that these calculations have all assumed normal incidence light. The detector will be at the focal plane of the instrument, so in some respects this is a valid

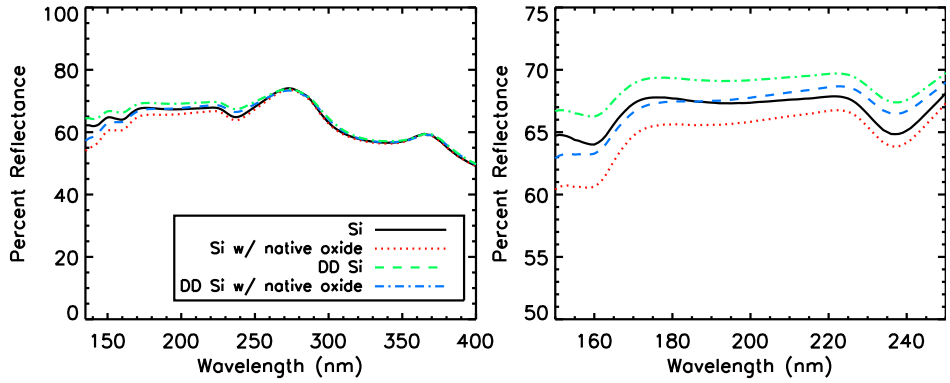

Figure 5.1 **Left Plot:** Reflectance for Bulk silicon from 137 nm to 400 nm. Over-plotted is the reflectance of silicon with the addition of a 3.413 nm thick delta-doped layer. Models are shown for silicon with a native oxide layer (2 nm SiO_2) in both cases. The average deviation is 2-3 percent, only becoming important below around 270 nm. The decreased reflectance below 150 nm for films with a native oxide is due completely to absorption in the oxide layer. **Right Plot:** A close up view of the region of interest for this work, between 140 and 260 nm.

approximation. For FIREBall-2, the intended instrument, the incoming beam is f/2.5, so the angles hitting the detector are between 0 and 11.3°. For these small angles, the change in QE compared to normal incidence is extremely small. The peak of the model may shift by 1 nm at the most. For a much faster telescope (f/1, for example), the angle of incidence can be as high as 26.5°, shifting the peak by several nm, and may become an important consideration in model development.

In previous work, we have used standard silicon optical constants to determine the expected reflectance and transmittance of film materials. However, we have found that the optical constants of delta-doped silicon are slightly different than undoped silicon. Alternative optical constants for delta-doped silicon were measured by J.A. Woollam, Inc. While the difference is slight at most wavelengths, the reflectance can change by several percent at UV wavelengths, and so we include this layer in our calculations. Figure 5.1 shows the

percent difference between bulk silicon and delta doped silicon. This change is minor, but given the importance of the substrate in multi-layer AR coating stacks, we chose to include this information. We use the following structure in our reflectance calculations: a bulk silicon substrate, a 3.413 nm thick delta-doped silicon layer with alternative constants, and a 1.7 nm thick native SiO_2 oxide. In this calculation, we determine the reflectance off of the stack and any added coatings. Absorption is not a concern for the delta doped layer, as any electrons liberated there are detected in the CCD. Absorption calculations take into account the native oxide and any added coatings only. Anticipated transmission is calculated by subtracting reflectance and absorption from 100%. The optical constants of delta-doped silicon are included in the Appendix.

We have developed a suite of sample films to increase QE above the reflectance limit of silicon, in some cases reaching 90%, at 205 nm. We summarize each model in Table 5.1. Listed characteristics are peak QE and corresponding wavelength, materials, and width of band at 50% QE. Initially, combinations of just two materials were used to develop the models and we restricted complexity to three layers films. These provided a base from which further films could be developed. We found that 4 of 6 combinations yielded transmission above 80% at 205 nm, as shown in Table 5.1.

Out of these, we selected SiO_2 and Al_2O_3 to use in multi-layer films with more than 3 layers, in large part because their growth is straightforward and repeatable using ALD. Al_2O_3 has also been used as a barrier layer in the growth of a HfO_2 AR-coating, described in Nikzad et al. (2012), and so was a reliable base layer for more complex designs. Absorption from Al_2O_3 begins to increase significantly below 180 nm, but there is still some absorption

(1-2% for a 3 layer film, higher for more layers) at 200 nm. This limits the number of layers that are viable with this combination. We show models for two more complex films, using 5 and 11 layers. The 5 layer film, 5A, is similar to the 3 layer film 3C, but with a higher peak and narrower width. The 11 layer film, 11A, has two peaks with lower QE than the single peak of film 5A, but higher QE at the edges of the band (above 70 % between 195-215 nm). The exact behavior is shown in Figure5.2.

Future work could explore more complex designs with other materials or with more than two materials. Additionally, it is worth noting that these films were developed for a particular wavelength but in principle one can develop high QE models for any wavelength between 155 and 350nm. The choice of materials is restricted at shorter wavelengths because of increased absorption. At longer wavelengths (above 370nm), broadband coatings can yield high QE (>90%) over several hundred nm, so these multi-layer stacks are less useful.

Table 5.1 Table summarizing characteristics of potential high QE films. Models 205 and 199/210 are pictured in Figure 5.2. Other models are pictured in Figure 5.3.

Model	Materials	# of layers	Max QE %	λ of Max (nm)	Width at 50% QE (nm)
GOAL			>75	205	15
3A	SiO_2,MgF_2	3	61.2	204	33
3B	MgO,Al_2O_3	3	75.9	205	37
3C	SiO_2,Al_2O_3	3	80.9	205	47
3D	MgF_2,Al_2O_3	3	82.8	205	48
3E	MgO,MgF_2	3	87.2	205	39
3F	SiO_2,MgO	3	87.6	205	40
5A	SiO_2,Al_2O_3	5	90.4	205	23
11A	SiO_2,Al_2O_3	11	79.7/84.0	199/210	22

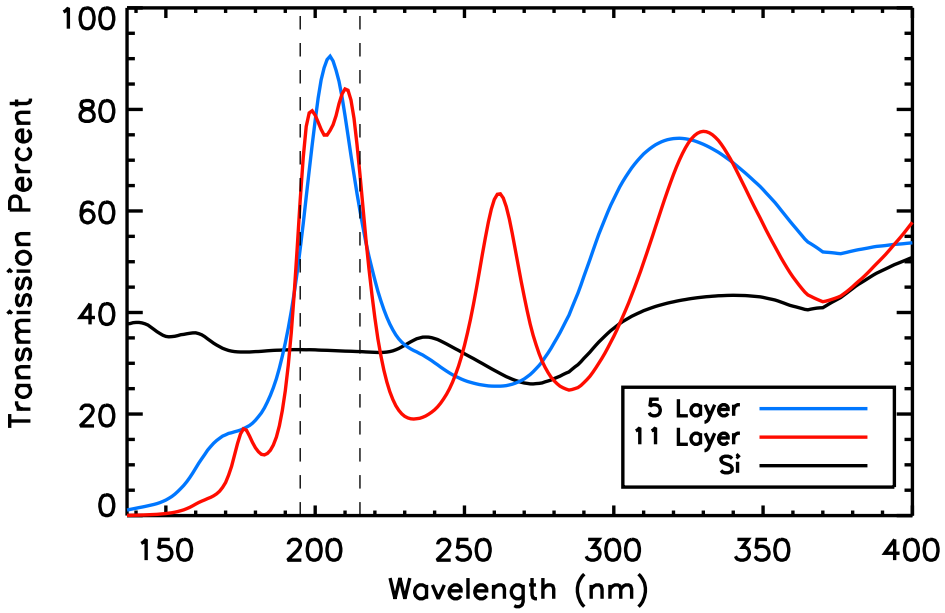

Figure 5.2 Expected transmission for two multi-layers optimized around 205 nm. The blue line shows a 5 layer film using SiO_2 and Al_2O_3 to achieve a single peak centered around 205 nm. This peak reaches 90.4 % potential QE. The red line shows an 11 layer coating optimized for high transmission from 195 nm to 215 nm, also using SiO_2 and Al_2O_3. The double peak has a lower maximum, but a higher overall QE from 195 nm to 215 nm. The black line indicates transmission into silicon without additional coatings.

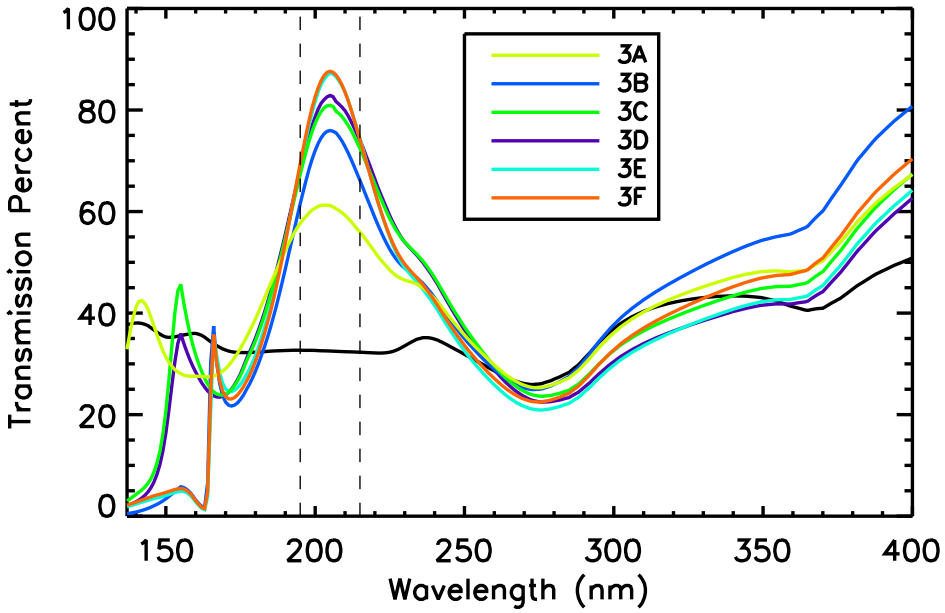

Figure 5.3 Expected transmission for several multi-layers optimized around 205 nm.

5.3 Deposition Techniques

All depositions were made using Atomic Layer Deposition (ALD) at NASA's Jet Propulsion Laboratory. ALD enables conformal, atomic level control over film growth and allows well controlled, repeatable depositions. ALD recipes for Al_2O_3 came from Goldstein et al. (2008), MgO from a custom reaction developed at JPL by the authors, SiO_2 from Dingemans et al. (2011) and HfO_2 from Liu et al. (2005). Often growth recipes required modifications to accommodate the equipment used. Modified growth recipes were typically validated using either X-ray photoelectron spectroscopy (XPS), transmission electron microscopy (TEM), or both. Growths were typically conducted at 200 °C. More information on ALD growth techniques can be found in Greer et al. (2013)).

Films were grown on 1 inch <100> 1-20 Ohm-cm silicon wafers (to test reflectance) and on fused silica windows (to test absorption). As noted above, differing optical constants between un-doped and doped silicon means the films tested here are slight modifications to the ones described above. These films will have reflectance percentages lower by 2-3 points than if applied to a doped layer. All measurements (and corresponding models) plotted are based on a silicon substrate without the doped layer. We are still able to test the overall nature of the film, its behavior compared to the film when modeled on normal silicon, and we expect few changes when grown on delta-doped CCDs. Previous work on delta-doped CCDs has shown good fidelity to model predictions. Thicknesses were verified by spectroscopic ellipsometry (Sentech).

Our previous work, described in Nikzad et al. (2012) and Hamden et al. (2011), has consisted almost entirely of single-layer film growths on silicon substrates. In general, ALD

growth calibration is done in this way—a single film on a silicon substrate. For these multi-layers, only the first layer is grown on silicon. For the second layer and beyond, we are growing films on top of an existing dielectric film, not silicon or silicon with its native oxide. Thus, growth rates of films may be different depending on what material forms the baselayer. In this instance, the SiO_2 layers (grown on Al_2O_3) were consistently 3-4 nm thinner than desired. Further study by our group has shown that the growth rate of SiO_2 is the same as on silicon, but the number of cycles required to achieve good surface nucleation changed. Figure 5.4 shows the measured thickness for growths of SiO_2 on normal silicon and on silicon with a 7 nm thick layer of Al_2O_3 applied first. In all cases, the SiO_2 grown on the Al_2O_3 base was thinner. The nucleation delay can be seen as the offset of the y-intercept. The growth rate (the slope of the lines) remains the same. In practice, several additional growth cycles are required when growing SiO_2 on Al_2O_3 versus silicon or its native oxide.

For deposition on delta-doped CCD devices, which are described in Section 5.5, we kept all the conditions the same as for growths on silicon wafers, with the addition of a carrier wafer to protect the frontside circuitry from scratching on the ALD plate surface.

5.4 Reflectance Testing

Reflectance tests were conducted using a reflectance set-up at Columbia University. The samples were placed in a vacuum chamber maintained at less than 1×10^{-4} torr for the duration of the measurement. An Acton monochrometer fed by a focused deuterium lamp provides light from 120 nm to 600-700 nm. The light then is directed towards samples and measured at any angle from nearly normal in reflection (5 °) to straight through in

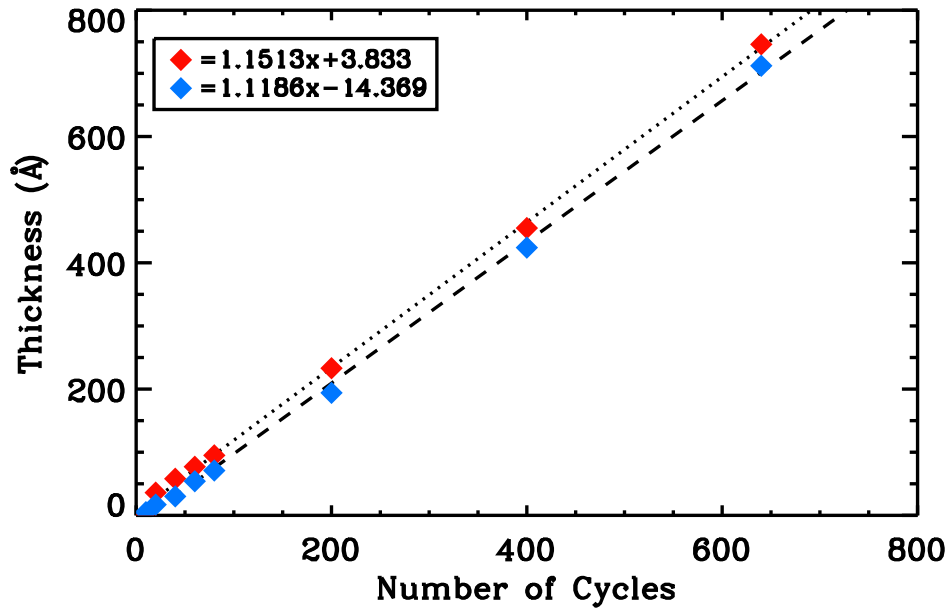

Figure 5.4 Growth rate of SiO_2 on both normal silicon (in red) and on a 7 nm thick Al_2O_3 base layer (in blue). While the growth per cycle remains constant, the initial growth is much slower on the AL_2O_3 base layer, reflecting the difference in the number of cycles required for good surface nucleation.

transmission. Current measurements were taken using a PMT (R6095) with a scintillator and light pipe assembly (McPherson Model 658). In testing films grown on silicon substrates, reflectance was at $5 - 10\,^\circ$ from normal. For transparent substrates, usually fused silica, the light was able to pass directly through the sample. For each sample the following set of measurements were made: direct intensity from the lamp, reflected intensity from the sample, reflected intensity from a bare silicon standard, reflected ambient intensity not directly in the path of the light. This last measurement is from an open filter position and serves as a background measurement. These measurements were then used to calculate direct reflectance from the sample and silicon (as a standard).

We found the film performed as designed, although the overall thickness was slightly thinner than desired, for reasons discussed in Section 5.3. We are able to model the new

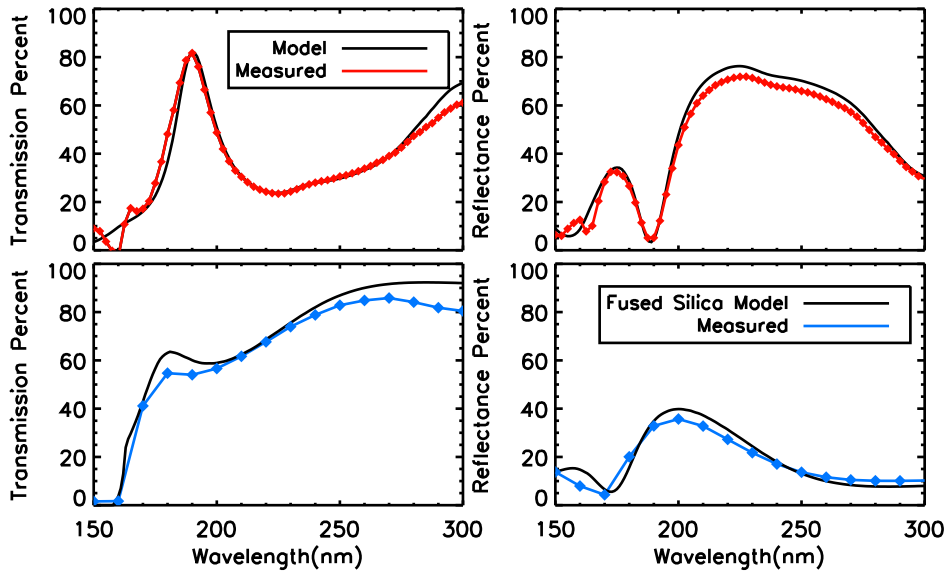

Figure 5.5 **Top Left** Estimated transmission for a 5 layer film of SiO_2 and Al_2O_3. Peak transmission is at 190 nm, and far exceeds previous work at this wavelength (approximately 60% transmission). This transmission was determined by subtracting the reflectance and absorption from 100 %. **Top Right** Measured reflectance for a 5 layer film of SiO_2 and Al_3O_3. Minimum reflectance is at 190 nm. **Bottom Left** Measured transmission for 5 layer film on fused silica window. **Bottom Right** Measured reflectance for 5 layer film on fused silica window. Both transmission and reflectance of the 11 layer film on fused silica were used to calculate expected absorption from the film itself, as described in Section 5.4. This absorption measurement is combined with reflectance measurements (Top Right) to calculate expected transmission (Top Left) from the film when deposited on a silicon device.

film with thinner SiO_2 layers, and find that it matches the observed reflectance and expected transmission very well (Figure 5.5).

Further growths of the 5-layer film have been conducted, incorporating the rates of SiO_2 growth described above. A plot of estimated transmission for a growth using new rates is shown in Figure 5.6. Transmission is estimated by measuring both reflectance off the silicon surface and absorption due to the layer applied to a fused silica window. Measurements of both reflection and transmission through the window were taken. These measurements, which also follow the model well, confirm that the behavior of the film is as expected. To

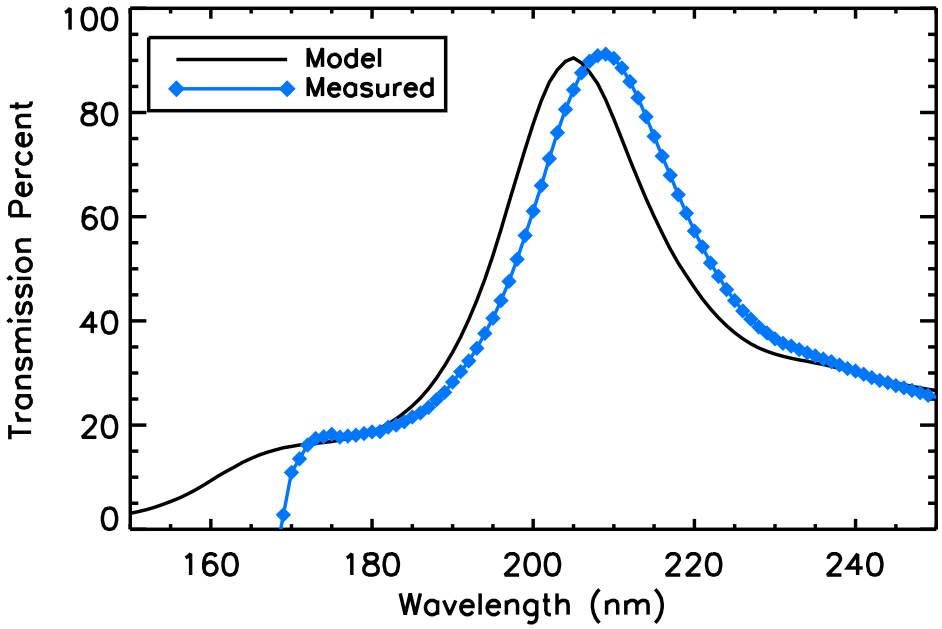

Figure 5.6 Estimated transmission of a refinement of the 5-layer film design, grown using new SiO_2 deposition rates. Peak transmission ($> 90\%$) is now at 209 nm, still somewhat off from the target of 205 nm. This is probably due in part to a native oxide layer on the silicon substrate. The height of the peak is increased above the model because of decreasing absorption at longer wavelengths.

calculate absorption in the layer, we subtract the measured absorption of an uncoated window from the measured absorption of the layer and window. The difference in absorption we ascribe to the effect of the layer. This underestimates the absorption at very low wavelengths (< 160 nm), where the fused silica is very absorbing. However, since our region of interest is at 200 nm and longer, substrate absorption will not significantly affect our results. For shorter wavelength coatings, a MgF_2 window would be advisable. Estimated transmission is calculated by subtracting this measured absorption absorption and previously measured reflectance off a silicon substrate from 100%.

Finally, we have begun experimenting with more elaborate multi-layer stacks. The 11 layer film, modeled in Figure 5.2 and tested in Figure 5.7, is our most complex to date and

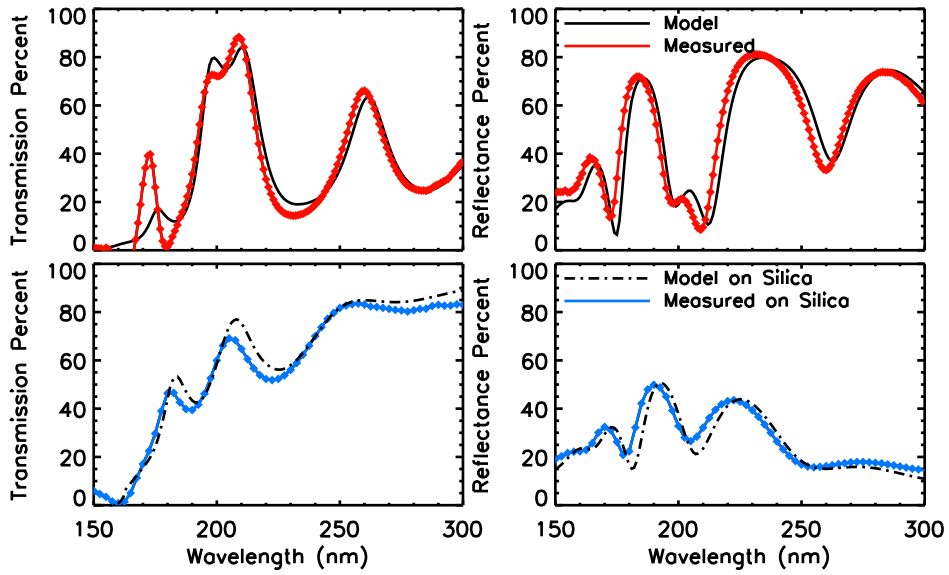

Figure 5.7 **Top Left** Estimated transmission for an 11 layer film of SiO_2 and Al_2O_3. Peak transmission is at 209 nm, with an average transmission of 79% between 195 and 215 nm. This transmission was determined by subtracting the reflectance and absorption from 100 %. **Top Right** Measured reflectance for a 11 layer film of SiO_2 and Al_3O_3. Minimum reflectance is at 209 nm. **Bottom Left** Measured transmission for 11 layer film on fused silica window. **Bottom Right** Measured reflectance for 11 layer film on fused silica window. Both transmission and reflectance of the 11 layer film on fused silica were used to calculate expected absorption from the film itself, as described in Section 5.4. This absorption measurement is combined with reflectance measurements (Top Right) to calculate expected transmission (Top Left) from the film when deposited on a silicon device.

allows us to achieve a double-peaked QE configuration. This film was grown incorporating the rates of SiO_2 growth on an Al_2O_3 baselayer. The model has a slightly lower peak QE (84% vs. 90%) but has higher average QE overall. The estimated transmission is somewhat off from the model, with absorption calculated as described above for the 5 layer film. This slight change is likely the result of a few nm difference of the top or bottom layer. Changes of only a nm or two can be enough to change the peak heights by several percentage points.

5.5 QE measurements from CCDs

The 5-layer film described above was deposited on thinned and delta-doped CCDs. The testing set-up is described in greater detail in Jacquot et al. (2011) and was used to measure QE for our previous work on single layer AR coatings described in Nikzad et al. (2012). To briefly summarize, this setup uses a calibration system to directly measure QE from a range of devices. The light source used is a deuterium lamp for wavelengths below 350 nm and a quartz tungsten Halogen lamp above 350 nm into the IR. A set of pre-filters restricts the wavelengths of light going into the monochromoter, minimizing leak from bluer wavelengths in the case of the deuterium lamp, and redder wavelengths for the quartz tungsten lamp. These filters are sufficient to reduce out of band leak to less than 2 percent, and below 0.5 percent at UV wavelengths. The filtered light passes through a monochromoter and is then either detected by a calibrated photodiode or sent through a series of diffusers to flatly illuminate the cooled CCD.

A set of images is taken with the CCD at each wavelength, including darks, and a region of interest extracted from each. The gain is calculated using the standard photon-transfer curve procedure. The mean number of counts per second in the region of interest is converted into electrons per second, using a quantum yield correction as necessary. A prior calibration of the system using a NIST photodiode in place of the CCD is used to calculate the expected flux hitting the CCD location and obtain a ratio relative to the flux at the calibrated photodiode. The ratio of flux should remain the same when the CCD is put in place of the NIST photodiode. This flux ratio is then used to calculate the flux incident on the CCD and thus the QE.

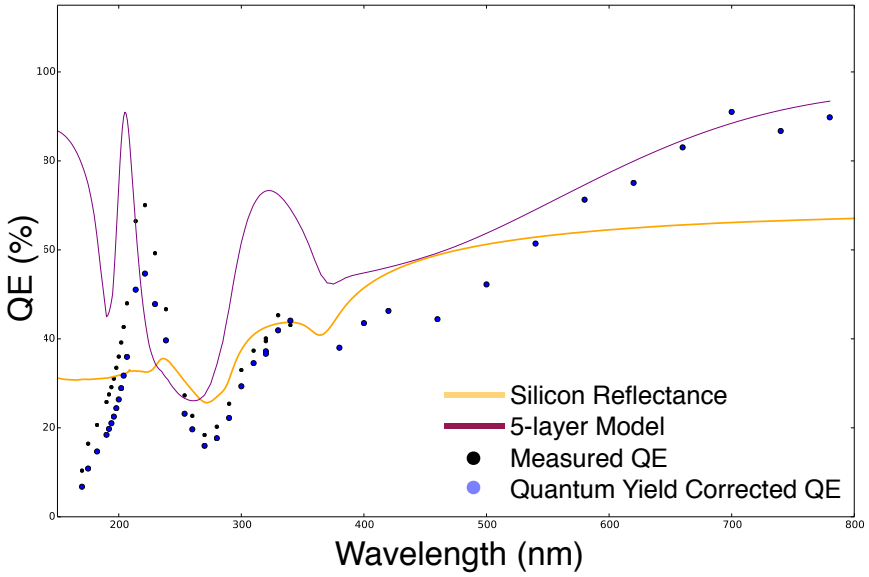

Figure 5.8 Preliminary QE data of 5-layer film on delta-doped STA device. This plot shows quantum efficiency in percent on the y-axis vs. wavelength in nm on the x-axis, as tested at JPL. Correction is made for quantum yield.

The 5-layer film described above was deposited on a number of devices for QE testing. A delta-doped STA device has been used for a number of reasons. These STA devices were intended for use on the guider segments of WASP (WAfer-Scale camera for Prime), a broadband imaging camera on Palomar. To achieve high QE in the red, these devices are thick. The JPL team has applied broadband AR coatings with excellent results to delta-doped STA devices. Since their characteristics are well known and QE testing with these devices has been successful in the past, we use them as a way of testing the quality of the 5-layer coating separate from the functionality of the EMCCD.

Preliminary QE data is shown in Figure 5.8, with quantum efficiency from 0 to 100% on the y-axis and wavelength from 160 to 800nm on the x-axis. The yellow line shows

expected QE from a delta-doped but uncoated device, following the reflectance limit of silicon. The purple line is the model 5-layer coating, and values we hope to match with the QE measurement. The dots indicate wavelengths with measured QE using the set-up described above. The black dots indicated the raw QE data, while the blue dots show the QE after applying a quantum yield correction. In the visible, above 400 nm, the quantum yield corrected QE (blue dots), show a reasonably good match to the model (purple line). Below this, in the blue to mid-UV (280-400 nm) and near UV (190-250 nm), the match is not very good in exact values, but the shape of the quantum yield corrected QE is encouraging. The relative heights between the 205 nm peak and the hump between 280-400 nm are similar for both the data and the model. The peak in the NUV is somewhat offset from the desired peak in the model, indicating that the coating may be too thick.

The overall drop off in QE below 400nm may be due in part to a window and air gap in the STA testing set-up, where UV transmission will be reduced. Other deviations from the model may be the result of surface oxides and contaminants, or contaminants in the AR coating itself. Contaminants in the coating itself are likely not very significant, since the sharp peak is sensitive to the optical properties of the component films. A significant deviation from the expected optical properties should result in no peak or a severely deformed peak. Finally, there may remain some calibration issues that are suppressing the QE at UV wavelengths. Despite these deviations, the location and general shape of the peaks matches the model and we remain hopeful that further testing will reveal high QE as predicted by the model.

5.6 Discussion

We find that films made with ALD are able to match expected values for reflectance and absorption on inert substrates with great accuracy. Our goals for this coating were reflectance below 20% and absorption $< 5\%$, centered on 205nm with a bandpass of roughly 15 nm. The 5-layer film we developed can achieve very low reflectance ($<10\%$) over a 22 nm bandpass, yielding potential QE of $>80\%$. The 11-layer film, our most complex to date, also shows very good fidelity to the model on silicon and fused silica substrates. As ALD technology improves and recipes for additional materials are developed, we will be able to create even more complex multi-layers with more reliability in the future.

In all of our films, we initially had systematic errors related to film growth. Typically deposition errors result from inaccurate growth curves for new materials (i.e. thickness of growth per cycle), and these errors are easy to correct with accurate characterization. Typical growth curves are also calculated by growing samples on silicon test wafers. But in our multi-layers, for example, SiO_2 is grown on existing layers of Al_2O_3, which appears to modify the nucleation behavior of SiO_2. Still, once characterized, the growth is highly repeatable, and we expect a good ability to hit thickness targets in the future. Random errors due to fluctuations in precursor dose between cycles, surface oxides, variations in pulse and pump times, and other deviations in the ALD process typically yield thickness errors on the order of a few percent.

In general, our previous work with AR-coated delta-doped devices (see Nikzad et al. 2012; Hoenk et al. 2013; Jewell et al. 2013 and more recent conference proceedings) has resulted in reliable coatings which yield expected QE. These coatings have spanned a wide

range of wavelengths in the visible (broadband 350-1000nm coatings) and UV (as described in previous works). Thus we view the results in Figure 5.8 to be extremely preliminary.

In developing a coating for use on FIREBall, we are fortunate in only needing to optimize for high QE over a small band-pass- the atmospheric window that enables FIREBall observations is narrow (20 nm). Because of the rapidly changing optical constants of silicon at UV wavelengths, the multi-layer coatings we have described here will tend towards narrow band-passes where the silicon constants are relatively stable. As additional layers are added, we are able to increase the peak transmission (from $\sim$50% with a single layer to nearly 90% with 5-layers), but at the expense of the bandpass, which narrows to 23 nm. The 11-layer coating we describe in Section 5.4 is able to maintain the bandpass width, but with a lower overall QE. In the case of FIREBall, a narrow bandpass is desirable, but for other applications this may not be the case. For now, we are forced to make a trade off between high QE and wide band-passes.

5.7 Acknowledgements

The authors wish to thank Michael Lee and Layton Baker, both of JPL, for their assistance with ALD processes. The research was carried out in part at the Jet Propulsion Laboratory, California Institute of Technology, under a contract with NASA. This work was partially supported by KISS, the W. M. Keck Institute for Space Studies, and by NASA Headquarters under the NASA Earth and Space Science Fellowship Program, NASA Grant NNX11AO07H, and NASA Grant NNX12AF29G. This research was supported in part through an appointment to the NASA Postdoctoral Program at the Jet Propulsion Lab, administered by Oak

Ridge Associated Universities through a contract with NASA.

Chapter 6

FIREBall[1]

6.1 Introduction

The Faint Intergalactic Red Shifted Emission Balloon (FIREBall-2) is a balloon-borne UV spectrograph funded jointly by NASA and CNES. FIREBall-2 uses a one meter primary mirror to feed a multi-object spectrograph optimized for narrow-band observations centered around 205 nm. The primary science goal of FIREBall-2 is to observe the diffuse gas around galaxies, known as the circumgalactic medium (CGM), via redshifted line emission. The main targets are emission from Lyman-α (121.56 nm) at a redshift of z=0.7, CIV at z=0.3, and OVI at z=1.0. This emission comes from the cooling of diffuse gas that is gravitationally bound to a galaxy, yet is far enough away from the galaxy to interact with the large scale structure of the universe.

[1]This chapter is a slightly edited version of a previously published SPIE conference proceeding. The full citation for this article is: "High efficiency CCD detectors at UV wavelengths". E. T. Hamden, A. D. Jewell, S. Gordon, J. Hennessy, M. E. Hoenk, S. Nikzad, D. Schiminovich, D. C. Martin. *Proc SPIE 9144*, July 2014.

Our current picture of the CGM comes from absorption line studies, using the spectra of background objects, such as quasars, to detect diffuse material around a foreground galaxy. These studies have successfully detected gas and metals around galaxies at a range of redshifts and impact parameters (Hennawi et al. 2006; Ribaudo et al. 2011; Steidel et al. 2011; Thom et al. 2012; Tumlinson et al. 2013), yet are limited by the small number of background objects per foreground galaxy. With only one or two sightlines per galaxy there is no straightforward way to distinguish between the presence of gas in filaments, a random collection of unconnected gas clumps, or a smooth distribution of gas filling the galactic halo.

FIREBall-2 is designed to overcome these limitations by observing emission directly from the CGM, instead of observing its effect on the spectra of background objects. With a multi-object spectrograph, we can target multiple regions of the CGM around a galaxy or cluster. This approach will provide both spatial and wavelength information about the CGM of a galaxy and will be the start of building a 3D picture of the dynamic CGM. The UV is targeted here for a variety of reasons. A large fraction of expected emission from the CGM (both continuum and line) is emitted at UV wavelengths for both low and high z galaxies. Additionally, almost all emission lines of note for the CGM are emitted at FUV wavelengths(Bertone et al. 2013). To observe these lines around a low redshift galaxy requires a space telescope, but a sub-orbital UV telescope can exploit certain wavelengths at a lower cost. There is an atmospheric window of high transmission ($\sim$80%) between O_2 and O_3 absorption bands (Brewer & Wilson 1965), shown in Figure 6.1, which allows for observation in the UV at balloon altitudes above ozone and oxygen (130,000 ft). FIREBall-2 seeks to exploit this window to observe the CGM in emission at low redshift for the first

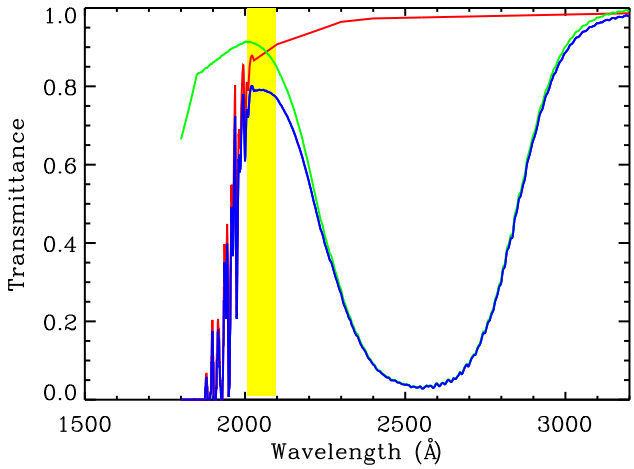

Figure 6.1 Atmospheric transmission between 100-300 nm at balloon altitudes. Yellow band shows FIREBall bandpass. The red line shows atmospheric transmission for O_2. The green line shows atmospheric transmission for O_3. The blue line shows the combined transmission of both O_2 and O_3, with an 80% transmission window at around 205 nm. The FIREBall bandpass is designed to fit in this narrow window of high transmission.

time. Atmospheric absorption varies significantly with altitude- the low altitude reached in FIREBall-1 (113,000 ft) resulted in only 25% transmission, instead of the 80% shown here.

6.1.1 Changes from FIREBall-1

A previous version of the mission, FIREBall-1 was launched on two occasions, in 2007 and 2009, from Fort Sumner, New Mexico (Tuttle et al. 2008; Milliard et al. 2010). FIREBall-1 was a fiber-fed spectrograph which used an Offner design and a GALEX-spare near-UV microchannel plate (MCP) (Doliber et al. 2000; Tuttle et al. 2010). FIREBall-1, while a technical and engineering success, found no detected CGM signal, with a detection limit of 20,000 LU. The spectrograph of FIREBall-2 has since been redesigned extensively to lower the detection limit.

Columbia in particular is responsible for delivering several parts of the redesigned spec-

trograph. Our work focuses on the Mask Guider System, which consists of a set of slit masks designed for calibration and 2-4 fields, guider camera and guidance software, a calibration lamp system, a shutter for protecting the detector, and red blocking coatings for the spectrograph optics.

A field corrector expands the field of view from 4x4 arcmin to 35x11 arcmin. This increases the number of potential targets per field, up to 50 at a time. The spectrograph itself will use a slit mask instead of fiber bundle. The slit mask, made by NiCoForm of a proprietary nickle cobalt alloy, has a radius of curvature (ROC) of 125mm, to perfectly match the curved focal plane from the telescope and field corrector. Laser cutting of the slit mask will be performed at the University of Arizona Instrumentation Center to create precise masks targeting several fields where bright circumgalactic medium emission may be found. The choice to use a slit mask does require the ability to select different masks for different fields of view. This increases the complexity of the system by requiring a rotating stage to select masks. FIREBall-1 conducted a blind survey with a fiber bundle covering the whole field of view. FIREBall-2 more efficiently uses detector area by conducting a targeted survey, where regions with expected CGM emission will be selected in advance. This multiplexing will provide large gains in overall sensitivity, increasing effective exposure time by a factor of $\sim$25. The slit mask also increases the overall throughput of the instrument by removing the fiber bundle IFU. The official throughput of the fibers used on FIREBall-1 (Polymicro FVP100110125) was 70% (Tuttle et al. 2008), although the actual bundle is believed to have a lower throughput. While a slit mask does force the selection of only certain targets for observation, and thus has a lower covering fraction, the regions which are observed suffer no

loss in throughput.

The detector change from a MCP to a CCD is likewise motivated by a desire to lower the detection limits to below the expected emission levels of the bright CGM (Bertone et al. 2013). The MCP used on FIREBall-1 was a GALEX NUV flight spare. This MCP had QE of 6% at the FIREBall bandpass, operating at high voltage and in a sealed tube. MCPs are known for having very low noise characteristics (Morrissey et al. 2005), which is vital for observations in this photon-limited regime. Recent improvements to CCD technology have made CCDs a viable alternative to MCPs at some UV wavelengths. These innovations are two-fold, incorporating very high quantum efficiencies at UV wavelengths with the ability to operate in a photon-counting mode with significantly reduced detector noise. These *electron multiplying* CCDS (EMCCDs) are described in more detail in other works (Mackay et al. 2001; Jerram et al. 2001; Gach et al. 2004). FIREBall-2 is pioneering the use of EMCCDs in sub-orbital missions, and will use the on-chip gain to minimize noise. We leave a more detailed discussion of this aspect of the detectors to other work.

The improvements in quantum efficiency via AR-coated delta-doped CCDs for FIREBall-2 has been described in detail in Chapters 4 and 5. Here we describe additional work towards increasing throughput via other optical surfaces in Section 6.2, as well as our mechanical work on the Mask Guider System (MGS) in Section 6.3. Finally, we discuss the theoretical overall throughput of FIREBall-2 as compared to FIREBall-1 in Section 6.4.

6.2 Red Blocking

FIREBall-1 used a dichroic to direct visible light to a guidance system and the UV output to the spectrograph. MCPs have some red sensitivity, less than 0.1%, so the dichroic also acted as a additional red blocking filter. FIREBall-2 will instead use a reflective slit-mask to direct light from non-science targets to the guidance system. Instead of a dichroic, out of band light will be rejected via the optical coatings on the surface of the spectrograph mirrors. The main function of the coating is to minimize out of band light and reduce red leak, while not sacrificing in-band reflectance. Here we require $< 10\%$ reflectance out of band and $> 85\%$ reflectance in band. Between 220 and $\sim$280 nm, even at 130,000 ft the atmosphere is very absorbing, and will remove those wavelengths without any assistance from us. Thus, we focus our rejection efforts on wavelengths longer than 280 nm. These coatings are very similar to traditional dichroics, passing long wavelength light and reflecting short wavelength light. Here we apply the coatings directly to a curved optical surface instead of using an additional optical element.

In developing potential red blocking coatings, we have relied on a relatively simple construction. The red blocking coating consists of two distinct sections grown on a fused silica substrate. The section adjacent to the substrate will be as transmissive as possible at all wavelengths, but with emphasis on wavelengths above 250 nm. This coating section serves to reduce out of band reflectance. A second section will then be applied which increases reflectance only in the desired band. This two phase structure serves to create highly reflective films in band without excessive out of band light. It also allows more freedom in our choice of materials. With UV light reflected off of the upper section, we are free to incorporate UV

absorbing materials in the lower section. To prevent visible light from reflecting off of the back surface of the optic and re-entering the optical path, we will apply a highly absorbing layer, potentially some optical black, to the backside of the optic. This layer will absorb any transmitted light that passes through the optic.

We have developed a suite of red blocking coatings optimized for the FIREBall bandpass. These coatings were designed to be applied to fused silica surfaces, but could easily be redesigned for almost any type of glass. The upper, reflective section is much less sensitive to the underlying substrate, and the lower section can be redesigned to accommodate the variations in optical properties between different glass types. The coatings we have developed are designed to be highly reflective over a range of angles of incidence (roughly 0-25° for all four spectrograph optics). In practice only the first two spectrograph optics will be coated. The simplest of these coatings uses HfO_2, Al_2O_3, and SiO_2 in a 13 layer stack, while the most complex uses 28 layers. These coatings are summarized in Table 6.1, and an example of reflectance for the most complex coating is shown in Figure 6.2, while the simplest such coating is shown in Figure 6.3. Other materials can also be used to create these types of coatings, but we selected these initial materials based on ease of growth using ALD.

We applied the simplest red blocking coating (RB-C-1) to a glass slide for initial tests, using ALD as described above. The reflectance results are shown in Figure 6.3. Both the model and the reflectance results are plotted. These samples were tested as described in Chapter 5.5. The results match the model to a good degree, with differences mainly attributable to a glass substrate instead of a fused silica substrate. One other consideration is the growth rate of HfO_2 on an Al_2O_3 base layer (and vice versa), which has not yet been

Name	No. Layers	Mean R In Band	Mean R Out of Band	Angles (deg)
RB A 1	18	87.7	5.3	0-7
RB A 2	18	87.8	5.2	0-7
RB B 1	24	92.1	4.0	15-23
RB B 2	22	92.1	4.0	15-23
RB C 1	13	83.7	6.1	0-25
RB C 2	19	90.3	4.9	0-25
RB C 3	28	95.1	4.8	0-25

Table 6.1 Characteristics of red blocking filters designed for use on FIREBall spectrograph optics. **A** films are designed for angles of incidence to Schmidt mirrors in spectrograph, while **B** films are designed to be used on the folding flats. **C** films can be applied to any spectrograph optic. All films are made of HfO_2, Al_2O_3, and SiO_2. Mean reflectance in band is calculated from 197-212 nm, while mean reflectance out of band calculated from 280-800 nm.

accounted for in the manner describe in Chapter 5.3 for SiO_2. This work shows the promise in such coatings for use in the future. We plan on conducting additional tests with fused silica and other glass substrates.

6.3 Mask Guider System

As part of the spectrograph redesign, the guider system needed to be updated and modified. Additionally, the replacement of the fiber IFU with a slit mask meant several additional changes. These changes include a new way to direct light to the guider, updated guidance system, a slit mask with 125mm radius of curvature, a rotational stage to select from several slit masks, and red blocking filters/coatings to remove out of band light. The inclusion of an EMCCD, which is extremely light sensitive, requires the inclusion of a shutter. With these redesigns, a new calibration set-up is also required. Nearly all of these components are included in the Mask Guider System (MGS), which includes the guider and guider optics,

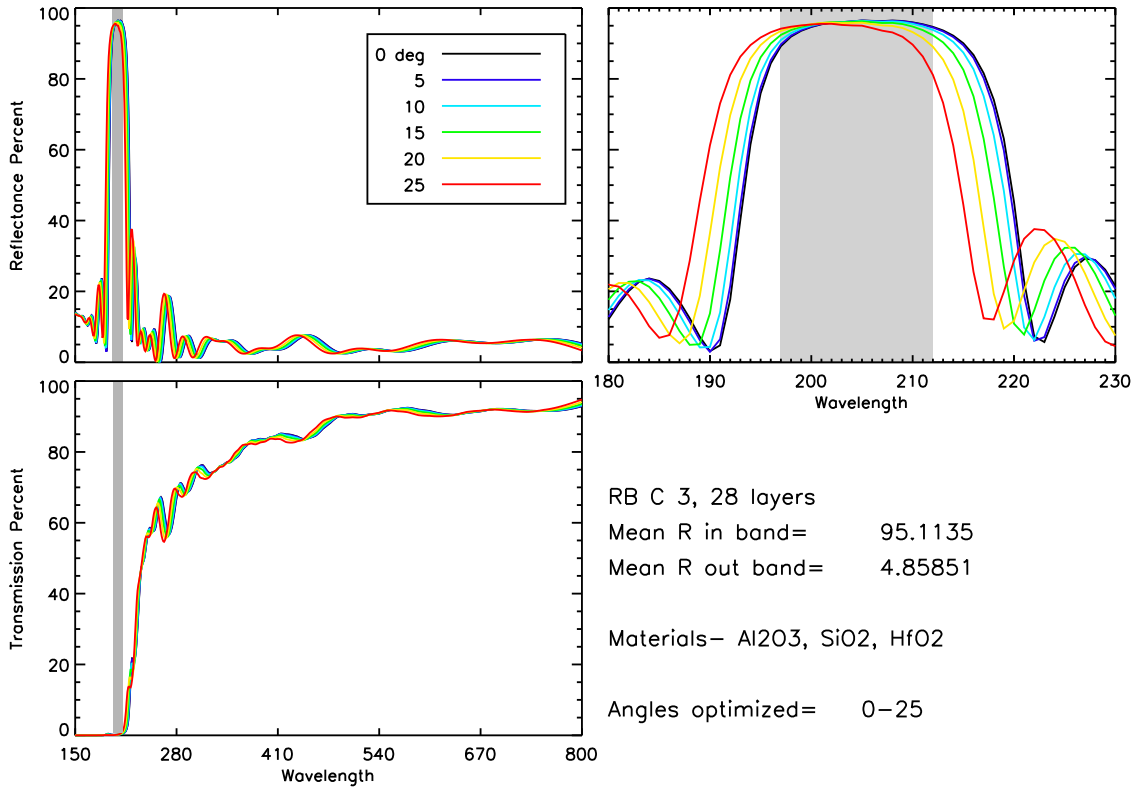

Figure 6.2 Example of most complex red blocking design for FIREBall-2. This design (RB-C-3)uses 28 layers of HfO_2, Al_2O_3, and SiO_2, and is designed for high reflectivity at all angles of incidence in the spectrograph. **Upper Left:** Reflectance vs. wavelength for a range of angles of incidence. The FIREBall band is indicated in gray. **Upper Right:** Close up of reflectance for the FIREBall bandpass. The change with angle of incidence is more clear in this case. **Lower Left:** Transmission vs. wavelength for a range of angles of incidence. The light transmitted through the optic will be absorbed by an optical black at the back of the optic.

reflective and science masks, rotational stage, shutter, and calibration sources.

6.3.1 Guider

In FIREBall-1, the guider was fed by a dichroic which directed visible light into the guider and UV light into the fiber IFU. Since the IFU is being replaced with a slit mask, light will be directed to the guider from a reflective mask placed just above the slit mask at a slight angle

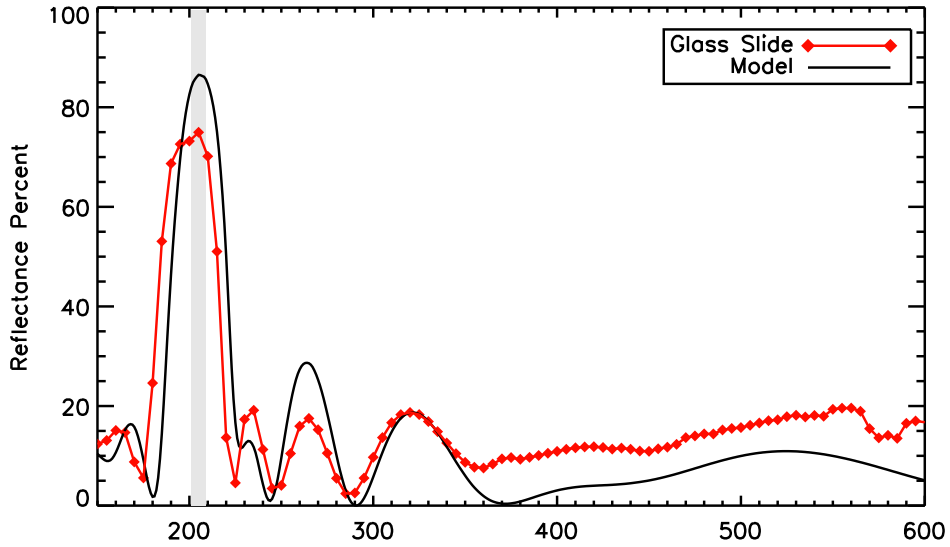

Figure 6.3 Reflectance measurement of red blocking coating RB-C-1 on a glass slide with a 5° angle of incidence. The FIREBall band is highlighted in gray. The differences in peak height are possibly due to two things. The first is that the model has a fused silica substrate while the actual coating was grown on a glass slide. The second is there may be growth rate discrepancies for HfO_2 on Al_2O_3 that we haven't fully explored.

to the optical path. This angle directs light into the guider optics. The guider optics consist of two Plossl-like lenses that focus light on the PCO-edge 5.5 CMOS camera. The PCO-edge has 2560x2160 pixels, with capability of 2x2 binning and selectable regions of interest. The pixels are 6.5 μm on a side, with <1.3 e^- read noise per pixel. The camera communicates with the frame grabber through 2 CameraLink cables. The PCO-edge has a max frame rate of 100 fps, although we will likely operate in a 30 fps or less mode. The PCO-edge will provide images of nearby stars (down to 15th magnitude) to provide real-time guidance for both x and y position, as well as longer term guidance on rotation (1-5 min baseline). The guidance software is adapted from the software used successfully on FIREBALL-1, written by Matt Matuszewski. The PCO-edge frame grabber software is adapted from code written for the Balloon Experimental Twin Telescope for Infrared Interferometry project (BETTI).

This software interfaces with the PCO-edge and the Silicon Software IV frame grabber to capture and save fits files at regular intervals. This work is ongoing.

The PCO-edge and some of its optics will need to be isolated from the rest of the spectrograph system. The PCO-edge is not designed for use at high vacuum (10^{-6} Torr) and so will be placed in its own vacuum box, kept near atmosphere, and thermally coupled with the spectrograph can. We plan to minimize leak into the spectrograph through the use of a double O-ring, with the intermediate section kept at 2.25 Torr, the ambient pressure at balloon altitudes.

6.3.2 Mask Carousel

The mask carousel consists of a set of small mask holders arranged around a circular carousel. The masks with science field of view of 12mm by 26mm, are made from pieces of 50 micron thick NiCoForm alloy grown on a spherical mandrel with ROC=125 mm. These masks will be laser cut at the University of Arizona, with 50 slits per mask. The curvature of the mask matches the curvature of the focal plane. Each mask will be designed for a different field of view, with additional masks to provide calibration fields. These masks are held by small holders, arranged on flat carousel. This carousel will be rotated to select each mask for observations. The mask holder and carousel are currently being designed and will be finalized in the coming weeks.

A calibration system for the spectrograph is currently in the design stage. This system will consist of a platinum/neon lamp fed by fibers to the MGS focal plane. The fibers will likely illuminate the area between the science slit mask and the reflective guider mask, with

access via an opening in the mask holder. This will illuminate the spectrograph and slit mask for calibration lamps and during auto-collimation.

Below the mask carousel, between the slit mask and the spectrograph optic directly below it, will be a vacuum compatible shutter. This shutter will be used to protect the EMCCD while FIREBall is looking for targets, and its position below the slit mask is chosen so the guider still has access to the full field of view of the telescope while the shutter is closed.

6.4 Overall Sensitivity

The set of coatings described in Section 6.2 and 5.2 includes a coating applied directly to the detector and a set of coatings applied to two optics in the spectrograph. Each coating has been designed to maximize throughput in the FIREBall band while rejecting redder wavelengths. Additional contributors to the overall throughput are the atmospheric transmission (which depends very strongly on altitude), other optics (telescope and field corrector), and finally the grating. With these factors in mind, we estimate overall throughput of FIREBall, shown in Figure 6.4.

We assume 90% reflectance at all wavelengths on optics without an optimized coating, and 50% efficiency in the grating. The average throughput is 13% from 200 to 210 nm, a large improvement over the 0.5% system efficiency from FIREBall-1 (Tuttle et al. 2008). The main contributors to the higher throughput of FIREBall-2 is the detector, improved grating, and replacement of the fiber bundle with a slit mask. Finally, worth noting is the change in the overall fill factor, given that the slit mask will decrease solid angle coverage.

The losses due to the slit mask blocking are offset by both the increased field of view and by the targeted nature of the CGM survey, yielding more useful targets per field.

6.4.1 Redleak

One benefit of using a microchannel plate as a detector is the very strong efficiency cutoff at longer wavelengths. MCPs have been described as "solar-blind" because of their comparatively low sensitivity at visible wavelengths. One concern in using CCD detectors is that they are quite good at detecting visible light, usually with higher QE in the visible than the UV. Even with our high efficiency AR coating, visible QE is greater than 50% at wavelengths

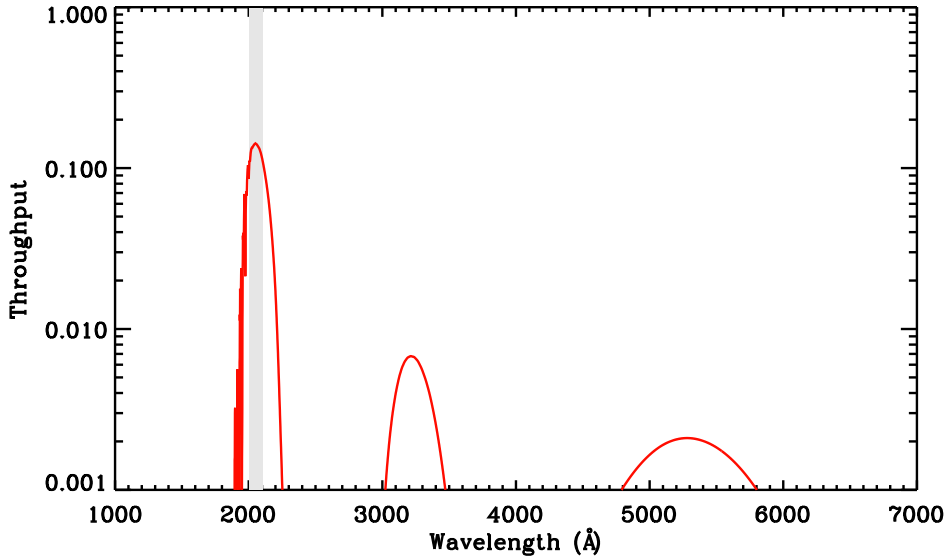

Figure 6.4 Theoretical estimate of overall FIREBall throughput, with a log scale. Includes atmospheric transmission, siderostat, primary mirror, two field corrector mirrors, two spectrograph optics with red blocking coating (RB C 1), grating with 50% efficiency, two spectrograph optics with aluminum plus MgF_2, detector with high efficiency AR coating. Throughput is above 10% between 200 and 210 nm, and nearly 14% at 205 nm. Out of band rejection is better than 1 in 20 between 300 and 350 nm, and better than 1 in 50 elsewhere. These ratios are low enough to ensure minimal contamination from redder wavelengths provided our grating meets the scattering requirement (less than 10^{-5} $Å^{-1}$).

longer than 300 nm. The design of our red blocking films, described in Section 6.2 is a first step in mitigating this issue. Two bounces off of the red blocking film suppresses the visible light to 0.3% of the initial value, averaged from 280 to 800 nm. Furthermore, since FIREBall is a spectrograph the wavelength dispersion of the grating also minimizes out of band light reaching the detector. With both of these red leak suppressing factors, out of band light should be reduced significantly.

The conventional wisdom regarding just how important red leak is for a UV telescope may be overstated. Commonly quoted calculations regarding the number of visible photons that must be rejected for every UV photon detected have not taken into account the type of objects commonly observed with a UV telescope. Observing a very red, cool object, such as in searching for planets around dwarf stars or observing elliptical galaxies, will naturally have an abundance of visible photons and a paucity of UV photons(O'Connell 1999; Joseph & Woodgate 2011). But many UV observations will not target these objects, instead focusing on things which are in fact bright in the UV. Such objects typically have a range in FUV/Vis ratio between 1 and .001 (1 to 1000 visible photons per FUV photons) (Bianchi et al. 2007). Furthermore, these calculations fail to take into account differences in sky background between the FUV and visible. Although the FUV has significantly lower zodiacal contamination than the visible and lower sky backgrounds overall than the visible; they are not negligible but are still within $\sim$1% of the visible background. The observations we are conducting will be background limited, and the 10^6-10^8 numbers don't take that difference into account.

Finally, the constraints on red leak for a spectrograph are quite different than for an

imager. A spectrograph with a single grating will reject out of band light by 10^{-3}, with the main concern being scattering off of the grating. With the addition of red blocking filters, like those described above, any contribution from out of band light is well below the expected sky background level.

6.5 Future for FIREBall

FIREBall-2 is scheduled to launch in the fall of 2015 from Fort Sumner, New Mexico. The primary science goal of FIREBall, observations of Lyman-α emission from the CGM of z$\sim$0.7 galaxies, drives many of the technology improvements and design choices discussed here. The CGM is quite faint, and thus requires high throughput optics and a high efficiency detector. My work on improving the detector efficiency through the use of anti-reflection coatings, combined with delta-doping of electron multiplying CCDs, is a key component to improving the overall detection limits for FIREBall-2 to below that of the expected CGM emission. Further design choices are driven by this consideration, especially the switch to a multi-object spectrograph with a slit mask instead of the FIREBall-1 fiber IFU. This also drove the redesign of the spectrograph to include a field corrector to increase the number of objects per field.

FIREBall-2 will observe between 2 and 3 fields, for several hours each. The exact fields that we observe will depend on the launch window. With this data, we expect to conduct analysis on individual fields of view and on all fields of view statistically stacked. The results of FIREBall-2, including the performance of new technology, will help guide the target selection and design considerations of future missions.

6.6 Acknowledgements

The research was carried out in part at the Jet Propulsion Laboratory, California Institute of Technology, under a contract with NASA. This work was partially supported by KISS, the W. M. Keck Institute for Space Studies, and by NASA Headquarters under the NASA Earth and Space Science Fellowship Program, NASA Grant NNX11AO07H, and NASA Grant NNX12AF29G. This research was supported in part through an appointment to the NASA Postdoctoral Program at the Jet Propulsion Lab, administered by Oak Ridge Associated Universities through a contract with NASA.

Chapter 7

Conclusion

This thesis has combined an interest in astronomy and instrumentation to both conduct observations of the diffuse universe with existing technology and instruments and to improve technology to make future detections of the diffuse universe possible. My work with existing FUV GALEX data, as described in Chapter 2, used all sky data to constrain dust properties in our own galaxy, and may be useful in future work for the subtraction of the stellar continuum component of FUV and NUV backgrounds. We investigate the dependence of the background on Galactic coordinates, finding that a standard cosecant model of intensity is not a valid fit. Furthermore, we compare our map to Galactic all sky maps of 100 μm emission, N_{HI} column, and Hα intensity. We measure a consistent low level FUV intensity at zero-points for other Galactic quantities, indicating a 300 CU non-scattered isotropic component to the diffuse FUV. There is also a linear relationship between FUV and 100 μm emission below 100 μm values of 8 MJy/sr. We find a similar linear relationship between FUV and N_{HI} below 10^{21} cm^{-2}. The relationship between FUV and Hα intensity has no such

constant cutoff and shows the weakest correlation of the three. For all Galactic quantities, the slope of the linear portion of the relationship decreases with Galactic latitude. A modified cosecant model, taking into account dust scattering asymmetry and albedo, is able to accurately fit the diffuse FUV at latitudes above 20°. The best fit model indicates an albedo, a, of 0.62 $\pm$ 0.04 and a scattering asymmetry function, g, of 0.78 $\pm$ 0.05. Deviations from the model fit may indicate regions of excess FUV emission from fluorescence or shock fronts, while low latitude regions with depressed FUV emission are likely the result of self-shielding dusty clouds. In the process of creating a map of the all sky Galactic FUV background, I made a catalogue of the GALEX NUV all sky. I hope to make similar Galactic all sky maps in the NUV and an FUV-NUV color map in the future. Additionally, there are a number of interesting FUV bright clouds that are worth further investigation into their dust properties and the potential presence of molecular hydrogen fluorescence.

My work on CHαS and proto-CHαS demonstrates the cutting edge work that can be done at low cost using small telescopes. Once CHαS is built, very deep Hα observations of nearby, low-z galaxies will reveal the motion of the bright CGM. CHαS has recently been funded by the NSF and will be built over the next few years at Columbia for installation at the MDM telescopes. Observations with CHαS should reveal Hα emission around low-z galaxies due to recent star formation or merger activity, as well as place limits on the intensity of the EUVB. I hope to finish analysis of the data taken from both runs of proto-CHαS to provide an initial view of bright Hα in the nearby universe. This work provides a complementary view of the CGM to that obtained by observing UV emission lines via FIREBall or other instruments.

My ongoing collaboration with JPL has produced ground breaking UV detectors which will be prime candidates for use on the next large UV space telescope. We describe progress in the development of a coated CCD detector with theoretical quantum efficiencies (QE) of greater than 60% at wavelengths from 120 to 300nm. This high efficiency may be reached by coating a backside illuminated, thinned, delta-doped CCD with a series of thin film anti-reflection coatings. The materials tested include MgF_2 (optimized for highest performance from 120-150nm), SiO_2 (150-180nm), Al_2O_3(180-240nm), and HfO_2 (240-300nm). A variety of deposition techniques were tested and a selection of coatings which minimized reflectance on a Si test wafer were applied to functional devices. We also discuss future uses and improvements, including graded coatings. We present new refinements of AR-coatings, which will improve performance in a narrower bandpass. Successful test films of a 5-layer and 11-layer coating have been made on both silicon and fused silica substrates and are presented here. The same film was also grown on a delta-doped CCD with preliminary testing discussed.

These devices were developed in part to improve sensitivity for FIREBall-2. A future mission such as ISTOS will require both photon-counting and high efficiency detectors in order to detect the CGM/IGM at low redshift. While MCPs have good noise characteristics and are photon-counting, EMCCDs with high QE AR-coatings should have even better noise properties, higher QE, larger dynamic range, and maintain photon-counting capability. FIREBall-2 will provide a test bed for these CCDs, to verify their reliability for future missions.

I plan to continue work on the projects described in this thesis in the future, and hope to see both CHαS and FIREBall-2 in fully functional form. Observations of the CGM, both

at low redshift via UV emission lines and Hα, or at higher redshift using other means, are still relatively new. I hope to be a part of some of the first groundbreaking observations of the CGM at high and low redshift. Through these new observations in the coming years, I will further our understanding of the diffuse universe.

Bibliography

Baggett, S. M., MacKenty, J. W., Kimble, R. A., Borders, T., Hilbert, B., Deustua, S., Kozhurina-Platais, V., Long, K. S., Riess, A., Gilliland, R., Hill, R. J., & Kalirai, J. 2010, in Society of Photo-Optical Instrumentation Engineers (SPIE) Conference Series, Vol. 7731, Society of Photo-Optical Instrumentation Engineers (SPIE) Conference Series

Becker, R. H., Fan, X., White, R. L., Strauss, M. A., Narayanan, V. K., Lupton, R. H., Gunn, J. E., Annis, J., Bahcall, N. A., Brinkmann, J., Connolly, A. J., Csabai, I., Czarapata, P. C., Doi, M., Heckman, T. M., Hennessy, G. S., Ivezić, Ž., Knapp, G. R., Lamb, D. Q., McKay, T. A., Munn, J. A., Nash, T., Nichol, R., Pier, J. R., Richards, G. T., Schneider, D. P., Stoughton, C., Szalay, A. S., Thakar, A. R., & York, D. G. 2001, AJ, 122, 2850

Berriman, G. B., Good, J. C., Curkendall, D. W., Jacob, J. C., Katz, D. S., Prince, T. A., & Williams, R. 2003, in Astronomical Society of the Pacific Conference Series, Vol. 295, Astronomical Data Analysis Software and Systems XII, ed. H. E. Payne, R. I. Jedrzejewski, & R. N. Hook, 343

Bershady, M. A. 2009, ArXiv e-prints

Bertone, S., Aguirre, A., & Schaye, J. 2013, MNRAS, 430, 3292

Bertone, S. & Schaye, J. 2012, MNRAS, 419, 780

Bianchi, L., Rodriguez-Merino, L., Viton, M., Laget, M., Efremova, B., Herald, J., Conti, A., Shiao, B., Gil de Paz, A., Salim, S., Thakar, A., Friedman, P. G., Rey, S.-C., Thilker, D., Barlow, T. A., Budavári, T., Donas, J., Forster, K., Heckman, T. M., Lee, Y.-W., Madore, B. F., Martin, D. C., Milliard, B., Morrissey, P., Neff, S. G., Rich, R. M., Schiminovich, D., Seibert, M., Small, T., Szalay, A. S., Wyder, T. K., Welsh, B. Y., & Yi, S. K. 2007, ApJS, 173, 659

Blacksberg, J. & Nikzad, S. 2006, in Optical Interference Coatings, Topical Meeting, Presented at the Optical Society of America

Bouwens, R. J., Illingworth, G. D., Franx, M., Chary, R.-R., Meurer, G. R., Conselice, C. J., Ford, H., Giavalisco, M., & van Dokkum, P. 2009, ApJ, 705, 936

Brandt, T. D. & Draine, B. T. 2012, ApJ, 744, 129

Bregman, J. N. 2007, ARA&A, 45, 221

Brewer, A. W. & Wilson, A. W. 1965, Quarterly Journal of the Royal Meteorological Society, 91, 452

Cen, R. & Ostriker, J. P. 1999, ApJ, 519, L109

Chen, H.-W. 2012, MNRAS, 419, 3039

Chen, H.-W., Helsby, J. E., Gauthier, J.-R., Shectman, S. A., Thompson, I. B., & Tinker, J. L. 2010, ApJ, 714, 1521

Chen, H.-W., Lanzetta, K. M., Webb, J. K., & Barcons, X. 2001, ApJ, 559, 654

Christlein, D., Zaritsky, D., & Bland-Hawthorn, J. 2010, MNRAS, 405, 2549

Clark, S. E., Peek, J. E. G., & Putman, M. E. 2014, ApJ, 789, 82

Collins, N. R., Boehm, N., Delo, G., Foltz, R. D., Hill, R. J., Kan, E., Kimble, R. A., Malumuth, E., Rosenberry, R., Waczynski, A., Wen, Y., Baggett, S., Bushouse, H., Deustua, S., Kim-Quijano, J., MacKenty, J., Martel, A., & Sabbi, E. 2009, in Society of Photo-Optical Instrumentation Engineers (SPIE) Conference Series, Vol. 7439, Society of Photo-Optical Instrumentation Engineers (SPIE) Conference Series

Crowell, M. H., Buck, T. M., Labuda, E. F., Dalton, J. V., & Walsh, E. J. 1967, Bell System Technical Journal, 46, 491

Dame, T. M., Hartmann, D., & Thaddeus, P. 2001, ApJ, 547, 792

Davé, R., Cen, R., Ostriker, J. P., Bryan, G. L., Hernquist, L., Katz, N., Weinberg, D. H., Norman, M. L., & O'Shea, B. 2001, The Astrophysical Journal, 552, 473

Dennison, B., Simonetti, J. H., & Topasna, G. A. 1998, Publications of the Astronomical Society of Australia, 15, 147

Dickey, J. M. & Lockman, F. J. 1990, ARA&A, 28, 215

Dingemans, G., Helvoirt, C. V., de Sanden, M. V., & Kessels, W. M. 2011, ECS Transactions, 35, 191

Doliber, D. L., Stock, J. M., Jelinsky, S. R., Malloy, J., Jelinsky, P. N., Siegmund, O. H., & Hull, J. S. 2000, in Society of Photo-Optical Instrumentation Engineers (SPIE) Conference Series, Vol. 4013, UV, Optical, and IR Space Telescopes and Instruments, ed. J. B. Breckinridge & P. Jakobsen, 402–410

Dong, R. & Draine, B. T. 2011, ApJ, 727, 35

Draine, B. T. 2003, ApJ, 598, 1017

—. 2011, Physics of the Interstellar and Intergalactic Medium

Edelstein, J., Min, K., Han, W., Korpela, E. J., Nishikida, K., Welsh, B. Y., Heiles, C., Adolfo, J., Bowen, M., Feuerstein, W. M., McKee, K., Lim, J., Ryu, K., Shinn, J., Nam, U., Park, J., Yuk, I., Jin, H., Seon, K., Lee, D., & Sim, E. 2006, ApJ, 644, L153

Fan, X., Carilli, C. L., & Keating, B. 2006, ARA&A, 44, 415

Finkbeiner, D. P. 2003, ApJS, 146, 407

Fix, J. D., Craven, J. D., & Frank, L. A. 1989, ApJ, 345, 203

Flint, B. K. 1982, Advances in Space Research, 2, 135

For, B.-Q., Staveley-Smith, L., & McClure-Griffiths, N. M. 2013, ApJ, 764, 74

Fowler, B., Liu, C., Mims, S., Balicki, J., Li, W., Do, H., Appelbaum, J., & Vu, P. 2010, in Society of Photo-Optical Instrumentation Engineers (SPIE) Conference Series, Vol. 7536, Society of Photo-Optical Instrumentation Engineers (SPIE) Conference Series

Freedman, W. L., Madore, B. F., Gibson, B. K., Ferrarese, L., Kelson, D. D., Sakai, S., Mould, J. R., Kennicutt, Jr., R. C., Ford, H. C., Graham, J. A., Huchra, J. P., Hughes, S. M. G., Illingworth, G. D., Macri, L. M., & Stetson, P. B. 2001, ApJ, 553, 47

Fukugita, M. & Peebles, P. J. E. 2004, ApJ, 616, 643

Gach, J., Guillaume, C., Boissin, O., & Cavadore, C. 2004, in Astrophysics and Space Science Library, Vol. 300, Scientific Detectors for Astronomy, The Beginning of a New Era, ed. P. Amico, J. W. Beletic, & J. E. Belectic, 611–614

Gladstone, G. R., Persyn, S., Eterno, J., Slater, D. C., Davis, M. W., Versteeg, M. H., Persson, K. B., Siegmund, O. H., Marquet, B., Gerard, J., & Grodent, D. C. 2008, AGU Fall Meeting Abstracts, B1678+

Goldstein, D. N., McCormick, J. A., & George, S. M. 2008, Journal of Physical Chemistry, 112, 19530

Górski, K. M., Hivon, E., Banday, A. J., Wandelt, B. D., Hansen, F. K., Reinecke, M., & Bartelmann, M. 2005, ApJ, 622, 759

Greer, F., Hamden, E., Jacquot, B. C., Hoenk, M. E., Jones, T. J., Dickie, M. R., Monacos, S. P., & Nikzad, S. 2013, Journal of Vacuum Science Technology A: Vacuum, Surfaces, and Films, 31, 01A103

Gunn, J. E. & Peterson, B. A. 1965, ApJ, 142, 1633

Haelbich, R. & Kunz, C. 1976, Optics Communications, 17, 287

Haffner, L. M., Dettmar, R.-J., Beckman, J. E., Wood, K., Slavin, J. D., Giammanco, C., Madsen, G. J., Zurita, A., & Reynolds, R. J. 2009, Reviews of Modern Physics, 81, 969

Haikala, L. K., Mattila, K., Bowyer, S., Sasseen, T. P., Lampton, M., & Knude, J. 1995, ApJ, 443, L33

Hamden, E. T., Greer, F., Hoenk, M. E., Blacksberg, J., Dickie, M. R., Nikzad, S., Martin, D. C., & Schiminovich, D. 2011, Applied Optics, 50, 4180

Hamden, E. T., Schiminovich, D., & Seibert, M. 2013, ApJ, 779, 180

Hartmann, D. & Burton, W. B. 1997, Atlas of Galactic Neutral Hydrogen

Hawley, S. A. & Miller, J. S. 1977, ApJ, 212, 94

Hennawi, J. F., Prochaska, J. X., Burles, S., Strauss, M. A., Richards, G. T., Schlegel, D. J., Fan, X., Schneider, D. P., Zakamska, N. L., Oguri, M., Gunn, J. E., Lupton, R. H., & Brinkmann, J. 2006, ApJ, 651, 61

Hoenk, M. E., Carver, A. G., Jones, T., Dickie, M., Cheng, P., Greer, F., Nikzad, S., Sgro, J., & Tsur, S. 2013, in 2013 International Image Sensor Workshop

Hoenk, M. E., Grunthaner, P. J., Grunthaner, F. J., Terhune, R. W., Fattahi, M., & Tseng, H.-F. 1992, Applied Physics Letters, 61, 1084

Hoenk, M. E., Jones, T. J., Dickie, M. R., Greer, F., Cunningham, T. J., Blazejewski, E. R., & Nikzad, S. 2009, in Presented at the Society of Photo-Optical Instrumentation Engineers (SPIE) Conference, Vol. 7419, Society of Photo-Optical Instrumentation Engineers (SPIE) Conference Series

Holtzman, J. A., Hester, J. J., Casertano, S., Trauger, J. T., Watson, A. M., Ballester, G. E., Burrows, C. J., Clarke, J. T., Crisp, D., Evans, R. W., Gallagher, III, J. S., Griffiths, R. E., Hoessel, J. G., Matthews, L. D., Mould, J. R., Scowen, P. A., Stapelfeldt, K. R., & Westphal, J. A. 1995, Publications of the Astronomical Society of the Pacific, 107, 156

Hopkins, A. M. & Beacom, J. F. 2006, ApJ, 651, 142

Hopkins, P. F., Quataert, E., & Murray, N. 2011, MNRAS, 417, 950

—. 2012, MNRAS, 421, 3522

Huffman, R. E., Leblanc, F. J., Larrabee, J. C., & Paulsen, D. E. 1980, Journal of Geophysical Research, 85, 2201

Hummels, C. B., Bryan, G. L., Smith, B. D., & Turk, M. J. 2013, MNRAS, 430, 1548

Hurwitz, M., Bowyer, S., & Martin, C. 1991, ApJ, 372, 167

Jacquot, B. C., Monacos, S. P., Hoenk, M. E., Greer, F., Jones, T. J., & Nikzad, S. 2011, Review of Scientific Instruments, 82, 043102

Jakobsen, P., Bowyer, S., Kimble, R., Jelinsky, P., Grewing, M., Kraemer, G., & Wulf-Mathies, C. 1984, A&A, 139, 481

Jakobsen, P., de Vries, J. S., & Paresce, F. 1987, A&A, 183, 335

Janesick, J., Elliott, T., Frasehetti, G., Collins, S., Blouke, M., & Corrie, B. 1989, Charge-Coupled Device Pinning Technologies

Janesick, J. R. 2001, Scientific charge-coupled devices, ed. J. R. Janesick

Jerram, P., Pool, P. J., Bell, R., Burt, D. J., Bowring, S., Spencer, S., Hazelwood, M., Moody, I., Catlett, N., & Heyes, P. S. 2001, in Society of Photo-Optical Instrumentation Engineers (SPIE) Conference Series, Vol. 4306, Society of Photo-Optical Instrumentation Engineers (SPIE) Conference Series, ed. M. M. Blouke, J. Canosa, & N. Sampat, 178–186

Jewell, A. D., Hennessy, J., Hoenk, M. E., & Nikzad, S. 2013, Wide band antireflection coatings deposited by atomic layer deposition

Jo, Y.-S., Min, K.-W., Seon, K.-I., Edelstein, J., & Han, W. 2011, ApJ, 738, 91

Joseph, C. L. & Woodgate, B. E. 2011, in Bulletin of the American Astronomical Society, Vol. 43, American Astronomical Society Meeting Abstracts 217, 305.02

Joung, M. R., Putman, M. E., Bryan, G. L., Fernández, X., & Peek, J. E. G. 2012, ApJ, 759, 137

Jura, M. 1979, ApJ, 227, 798

Kereš, D., Katz, N., Fardal, M., Davé, R., & Weinberg, D. H. 2009, MNRAS, 395, 160

Kereš, D., Katz, N., Weinberg, D. H., & Davé, R. 2005, MNRAS, 363, 2

Kregenow, J., Edelstein, J., Korpela, E. J., Welsh, B. Y., Heiles, C., Ryu, K., Min, K.-W., Lim, Y., Yuk, I.-S., Jin, H., & Seon, K.-I. 2006, ApJ, 644, L167

Kurt, V. G. & Sunyaev, R. A. 1970, in IAU Symposium, Vol. 36, Ultraviolet Stellar Spectra and Related Ground-Based Observations, ed. R. Muller, L. Houziaux, & H. E. Butler, 341

Laity, A. C., Anagnostou, N., Berriman, G. B., Good, J. C., Jacob, J. C., Katz, D. S., & Prince, T. 2005, in Astronomical Society of the Pacific Conference Series, Vol. 347, Astronomical Data Analysis Software and Systems XIV, ed. P. Shopbell, M. Britton, & R. Ebert, 34–+

Lallement, R., Welsh, B. Y., Vergely, J. L., Crifo, F., & Sfeir, D. 2003, A&A, 411, 447

Le Floc'h, E., Charmandaris, V., Forrest, W. J., Mirabel, I. F., Armus, L., & Devost, D. 2006, ApJ, 642, 636

Lee, D., Seon, K., Min, K. W., Park, Y. S., Yuk, I. S., Edelstein, J., Korpela, E. J., Sankrit, R., Park, S. J., & Ryu, K. S. 2008, ApJ, 686, 1155

Lee, D.-H., Yuk, I.-S., Jin, H., Seon, K.-I., Edelstein, J., Korpela, E. J., Adolfo, J., Min, K.-W., Ryu, K.-S., Shinn, J.-H., & van Dishoeck, E. F. 2006, ApJ, 644, L181

Leinert, C., Bowyer, S., Haikala, L. K., Hanner, M. S., Hauser, M. G., Levasseur-Regourd, A., Mann, I., Mattila, K., Reach, W. T., Schlosser, W., Staude, H. J., Toller, G. N., Weiland, J. L., Weinberg, J. L., & Witt, A. N. 1998, A&AS, 127, 1

Leroy, A. K., Walter, F., Sandstrom, K., Schruba, A., Munoz-Mateos, J.-C., Bigiel, F., Bolatto, A., Brinks, E., de Blok, W. J. G., Meidt, S., Rix, H.-W., Rosolowsky, E., Schinnerer, E., Schuster, K.-F., & Usero, A. 2013, AJ, 146, 19

Lim, T.-H., Min, K.-W., & Seon, K.-I. 2013, ApJ, 765, 107

Liu, X., Ramanathan, S., Longdergan, A., Srivastava, A., Lee, E., Seidel, T., Barton, J. T., Pang, D., & Gordon, R. G. 2005, Journal of the Electrochemical Society, 152, G213

Lynds, R. 1971, ApJ, 164, L73

Mackay, C. D., Tubbs, R. N., Bell, R., Burt, D. J., Jerram, P., & Moody, I. 2001, in Presented at the Society of Photo-Optical Instrumentation Engineers (SPIE) Conference, Vol. 4306, Society of Photo-Optical Instrumentation Engineers (SPIE) Conference Series, ed. M. M. Blouke, J. Canosa, & N. Sampat, 289–298

MacLeod, H. A. 1986, Thin-Film Optical Filters (London, GB: Institute of Physics Publishing)

Madsen, G. J., Reynolds, R. J., Haffner, L. M., Tufte, S. L., & Maloney, P. R. 2001, ApJ, 560, L135

Magnelli, B., Elbaz, D., Chary, R. R., Dickinson, M., Le Borgne, D., Frayer, D. T., & Willmer, C. N. A. 2009, A&A, 496, 57

Martin, C., Barlow, T., Barnhart, W., Bianchi, L., Blakkolb, B. K., Bruno, D., Bushman, J., Byun, Y., Chiville, M., Conrow, T., Cooke, B., Donas, J., Fanson, J. L., Forster, K., Friedman, P. G., Grange, R., Griffiths, D., Heckman, T., Lee, J., Jelinsky, P. N., Kim, S., Lee, S., Lee, Y., Liu, D., Madore, B. F., Malina, R., Mazer, A., McLean, R., Milliard, B., Mitchell, W., Morais, M., Morrissey, P. F., Neff, S. G., Raison, F., Randall, D., Rich, M., Schiminovich, D., Schmitigal, W., Sen, A., Siegmund, O. H. W., Small, T., Stock, J. M., Surber, F., Szalay, A., Vaughan, A. H., Weigand, T., Welsh, B. Y., Wu, P., Wyder, T., Xu, C. K., & Zsoldas, J. 2003, in Presented at the Society of Photo-Optical Instrumentation Engineers (SPIE) Conference, Vol. 4854, Society of Photo-Optical Instrumentation Engineers (SPIE) Conference Series, ed. J. C. Blades & O. H. W. Siegmund, 336–350

Martin, C. & GALEX Science Team. 2003, in Bulletin of the American Astronomical Society, Vol. 35, Bulletin of the American Astronomical Society, 1363–+

Martin, C., Hurwitz, M., & Bowyer, S. 1990, ApJ, 354, 220

—. 1991, ApJ, 379, 549

Martin, D. C., Chang, D., Matuszewski, M., Morrissey, P., Rahman, S., Moore, A., & Steidel, C. C. 2014, ApJ, 786, 106

Martin, D. C., Fanson, J., Schiminovich, D., Morrissey, P., Friedman, P. G., Barlow, T. A., Conrow, T., Grange, R., Jelinsky, P. N., Milliard, B., Siegmund, O. H. W., Bianchi, L., Byun, Y., Donas, J., Forster, K., Heckman, T. M., Lee, Y., Madore, B. F., Malina, R. F., Neff, S. G., Rich, R. M., Small, T., Surber, F., Szalay, A. S., Welsh, B., & Wyder, T. K. 2005, ApJ, 619, L1

McClure-Griffiths, N. M., Staveley-Smith, L., Lockman, F. J., Calabretta, M. R., Ford, H. A., Kalberla, P. M. W., Murphy, T., Nakanishi, H., & Pisano, D. J. 2008, ApJ, 673, L143

McKee, C. F. & Ostriker, J. P. 1977, ApJ, 218, 148

Milliard, B., Martin, D. C., Schiminovich, D., Evrard, J., Matuszewski, M., Rahman, S., Tuttle, S., McLean, R., Deharveng, J.-M., Mirc, F., Grange, R., & Chave, R. 2010, in Society of Photo-Optical Instrumentation Engineers (SPIE) Conference Series, Vol. 7732, Society of Photo-Optical Instrumentation Engineers (SPIE) Conference Series

Milne, D. K. & Aller, L. H. 1980, AJ, 85, 17

Moos, H. W., Cash, W. C., Cowie, L. L., Davidsen, A. F., Dupree, A. K., Feldman, P. D., Friedman, S. D., Green, J. C., Green, R. F., Gry, C., Hutchings, J. B., Jenkins, E. B., Linsky, J. L., Malina, R. F., Michalitsianos, A. G., Savage, B. D., Shull, J. M., Siegmund, O. H. W., Snow, T. P., Sonneborn, G., Vidal-Madjar, A., Willis, A. J., Woodgate, B. E., York, D. G., Ake, T. B., Andersson, B., Andrews, J. P., Barkhouser, R. H., Bianchi, L., Blair, W. P., Brownsberger, K. R., Cha, A. N., Chayer, P., Conard, S. J., Fullerton, A. W., Gaines, G. A., Grange, R., Gummin, M. A., Hebrard, G., Kriss, G. A., Kruk, J. W., Mark, D., McCarthy, D. K., Morbey, C. L., Murowinski, R., Murphy, E. M., Oegerle, W. R., Ohl, R. G., Oliveira, C., Osterman, S. N., Sahnow, D. J., Saisse, M., Sembach, K. R., Weaver, H. A., Welsh, B. Y., Wilkinson, E., & Zheng, W. 2000, The Astrophysical Journal Letters, 538, L1

Morgan, D. H., Nandy, K., & Thompson, G. I. 1976, MNRAS, 177, 531

Morrissey, P., Conrow, T., Barlow, T. A., Small, T., Seibert, M., Wyder, T. K., Budavári, T., Arnouts, S., Friedman, P. G., Forster, K., Martin, D. C., Neff, S. G., Schiminovich,

D., Bianchi, L., Donas, J., Heckman, T. M., Lee, Y., Madore, B. F., Milliard, B., Rich, R. M., Szalay, A. S., Welsh, B. Y., & Yi, S. K. 2007, ApJS, 173, 682

Morrissey, P., Schiminovich, D., Barlow, T. A., Martin, D. C., Blakkolb, B., Conrow, T., Cooke, B., Erickson, K., Fanson, J., Friedman, P. G., Grange, R., Jelinsky, P. N., Lee, S.-C., Liu, D., Mazer, A., McLean, R., Milliard, B., Randall, D., Schmitigal, W., Sen, A., Siegmund, O. H. W., Surber, F., Vaughan, A., Viton, M., Welsh, B. Y., Bianchi, L., Byun, Y.-I., Donas, J., Forster, K., Heckman, T. M., Lee, Y.-W., Madore, B. F., Malina, R. F., Neff, S. G., Rich, R. M., Small, T., Szalay, A. S., & Wyder, T. K. 2005, The Astrophysical Journal Letters, 619, L7

Murthy, J. 2014, Ap&SS, 349, 165

Murthy, J. & Conn Henry, R. 2011, ApJ, 734, 13

Murthy, J., Hall, D., Earl, M., Henry, R. C., & Holberg, J. B. 1999, ApJ, 522, 904

Murthy, J., Henry, R. C., & Sujatha, N. V. 2010, Astrophysical Journal, 724, 1389

Murthy, J. & Sahnow, D. J. 2004, ApJ, 615, 315

Nikzad, S., Hoenk, M. E., Greer, F., Jacquot, B., Monacos, S., Jones, T. J., Blacksberg, J., Hamden, E., Schiminovich, D., Martin, C., & Morrissey, P. 2012, Appl. Opt., 51, 365

Nikzad, S., Hoenk, M. E., Grunthaner, P. J., Terhune, R. W., Grunthaner, F. J., Winzenread, R., Fattahi, M. M., Tseng, H.-F., & Lesser, M. P. 1994, in Society of Photo-Optical Instrumentation Engineers (SPIE) Conference Series, Vol. 2198, Society of Photo-Optical Instrumentation Engineers (SPIE) Conference Series, ed. D. L. Crawford & E. R. Craine, 907–915

O'Connell, R. W. 1999, ARA&A, 37, 603

Palik, E. D. 1985, Handbook of optical constants of solids, ed. E. D. Palik

—. 1991, Handbook of optical constants of solids II, ed. E. D. Palik

Parenago, P. P. 1940, Astron. Zh., 17, 3

Paresce, F. 1990, in IAU Symposium, Vol. 139, The Galactic and Extragalactic Background Radiation, ed. S. Bowyer & C. Leinert, 307–316

Paresce, F., McKee, C. F., & Bowyer, S. 1980, ApJ, 240, 387

Park, S.-J., Min, K.-W., Seon, K.-I., Han, W., Lee, D.-H., & Edelstein, J. 2012, ApJ, 754, 10

Perault, M., Lequeux, J., Hanus, M., & Joubert, M. 1991, A&A, 246, 243

Perryman, M. A. C., Lindegren, L., Kovalevsky, J., Hoeg, E., Bastian, U., Bernacca, P. L., Crézé, M., Donati, F., Grenon, M., Grewing, M., van Leeuwen, F., van der Marel, H., Mignard, F., Murray, C. A., Le Poole, R. S., Schrijver, H., Turon, C., Arenou, F., Froeschlé, M., & Petersen, C. S. 1997, A&A, 323, L49

Philipp, H. R. & Taft, E. A. 1960, Physical Review, 120, 37

Planck Collaboration, Ade, P. A. R., Aghanim, N., Armitage-Caplan, C., Arnaud, M., Ashdown, M., Atrio-Barandela, F., Aumont, J., Baccigalupi, C., Banday, A. J., & et al. 2013, ArXiv e-prints

Porco, C. C., West, R. A., Squyres, S., McEwen, A., Thomas, P., Murray, C. D., Del Genio, A., Ingersoll, A. P., Johnson, T. V., Neukum, G., Veverka, J., Dones, L., Brahic, A., Burns, J. A., Haemmerle, V., Knowles, B., Dawson, D., Roatsch, T., Beurle, K., & Owen, W. 2004, Space Science Reviews, 115, 363

Prochaska, J. X., Weiner, B., Chen, H.-W., Mulchaey, J., & Cooksey, K. 2011, ApJ, 740, 91

Putman, M. E., Peek, J. E. G., & Joung, M. R. 2012, ARA&A, 50, 491

Reddy, N. A. & Steidel, C. C. 2009, ApJ, 692, 778

Reynolds, R. J., Haffner, L. M., & Madsen, G. J. 2002, in Astronomical Society of the Pacific Conference Series, Vol. 282, Galaxies: the Third Dimension, ed. M. Rosada, L. Binette, & L. Arias, 31

Reynolds, R. J., Tufte, S. L., Kung, D. T., McCullough, P. R., & Heiles, C. 1995, ApJ, 448, 715

Ribaudo, J., Lehner, N., Howk, J. C., Werk, J. K., Tripp, T. M., Prochaska, J. X., Meiring, J. D., & Tumlinson, J. 2011, ApJ, 743, 207

Rudie, G. C., Steidel, C. C., Trainor, R. F., Rakic, O., Bogosavljević, M., Pettini, M., Reddy, N., Shapley, A. E., Erb, D. K., & Law, D. R. 2012, ApJ, 750, 67

Ryu, K., Min, K.-W., Park, J.-W., Lee, D.-H., Han, W., Nam, U.-W., Park, J.-H., Edelstein, J., Korpela, E. J., Nishikida, K., & van Dishoeck, E. F. 2006, ApJ, 644, L185

Ryu, K., Min, K. W., Seon, K.-I., Nonesa, J., Edelstein, J., Korpela, E., Sankrit, R., Han, W., Park, J.-H., & Park, Y. S. 2008, ApJ, 678, L29

Salim, S., Rich, R. M., Charlot, S., Brinchmann, J., Johnson, B. D., Schiminovich, D., Seibert, M., Mallery, R., Heckman, T. M., Forster, K., Friedman, P. G., Martin, D. C., Morrissey, P., Neff, S. G., Small, T., Wyder, T. K., Bianchi, L., Donas, J., Lee, Y.-W., Madore, B. F., Milliard, B., Szalay, A. S., Welsh, B. Y., & Yi, S. K. 2007, ApJS, 173, 267

Sasseen, T. P. & Deharveng, J.-M. 1996, ApJ, 469, 691

Schiminovich, D., Friedman, P. G., Martin, C., & Morrissey, P. F. 2001, ApJ, 563, L161

Schiminovich, D., Ilbert, O., Arnouts, S., Milliard, B., Tresse, L., Le Fèvre, O., Treyer, M., Wyder, T. K., Budavári, T., Zucca, E., Zamorani, G., Martin, D. C., Adami, C., Arnaboldi, M., Bardelli, S., Barlow, T., Bianchi, L., Bolzonella, M., Bottini, D., Byun, Y.-I., Cappi, A., Contini, T., Charlot, S., Donas, J., Forster, K., Foucaud, S., Franzetti, P., Friedman, P. G., Garilli, B., Gavignaud, I., Guzzo, L., Heckman, T. M., Hoopes, C., Iovino, A., Jelinsky, P., Le Brun, V., Lee, Y.-W., Maccagni, D., Madore, B. F., Malina, R., Marano, B., Marinoni, C., McCracken, H. J., Mazure, A., Meneux, B., Morrissey, P., Neff, S., Paltani, S., Pellò, R., Picat, J. P., Pollo, A., Pozzetti, L., Radovich, M., Rich, R. M., Scaramella, R., Scodeggio, M., Seibert, M., Siegmund, O., Small, T., Szalay, A. S., Vettolani, G., Welsh, B., Xu, C. K., & Zanichelli, A. 2005, ApJ, 619, L47

Schlegel, D. J., Finkbeiner, D. P., & Davis, M. 1998, ApJ, 500, 525

Schruba, A., Leroy, A. K., Walter, F., Sandstrom, K., & Rosolowsky, E. 2010, ApJ, 722, 1699

Seon, K.-I., Edelstein, J., Korpela, E., Witt, A., Min, K.-W., Han, W., Shinn, J., Kim, I.-J., & Park, J.-W. 2011a, ApJS, 196, 15

Seon, K.-I., Witt, A., Kim, I.-J., Shinn, J.-H., Edelstein, J., Min, K.-W., & Han, W. 2011b, ApJ, 743, 188

Shen, S., Madau, P., Guedes, J., Mayer, L., Prochaska, J. X., & Wadsley, J. 2013, ApJ, 765, 89

Spiller, E. 1972, Applied Physics Letters, 20, 365

Spitzer, Jr., L. 1956, ApJ, 124, 20

Steidel, C. C., Bogosavljević, M., Shapley, A. E., Kollmeier, J. A., Reddy, N. A., Erb, D. K., & Pettini, M. 2011, ApJ, 736, 160

Stern, S. A., Slater, D. C., Scherrer, J., Stone, J., Dirks, G., Versteeg, M., Davis, M., Gladstone, G. R., Parker, J. W., Young, L. A., & Siegmund, O. H. W. 2008, Space Science Reviews, 140, 155

Sturch, C. 1966, ApJ, 143, 774

Sujatha, N. V., Murthy, J., Suresh, R., Conn Henry, R., & Bianchi, L. 2010, ApJ, 723, 1549

Thilker, D. A., Boissier, S., Bianchi, L., Calzetti, D., Boselli, A., Dale, D. A., Seibert, M., Braun, R., Burgarella, D., Gil de Paz, A., Helou, G., Walter, F., Kennicutt, Jr., R. C., Madore, B. F., Martin, D. C., Barlow, T. A., Forster, K., Friedman, P. G., Morrissey, P., Neff, S. G., Schiminovich, D., Small, T., Wyder, T. K., Donas, J., Heckman, T. M., Lee, Y.-W., Milliard, B., Rich, R. M., Szalay, A. S., Welsh, B. Y., & Yi, S. K. 2007, ApJS, 173, 572

Thom, C., Tumlinson, J., Werk, J. K., Prochaska, J. X., Oppenheimer, B. D., Peeples, M. S., Tripp, T. M., Katz, N. S., O'Meara, J. M., Ford, A. B., Davé, R., Sembach, K. R., & Weinberg, D. H. 2012, ApJ, 758, L41

Tumlinson, J., Thom, C., Werk, J. K., Prochaska, J. X., Tripp, T. M., Katz, N., Davé, R., Oppenheimer, B. D., Meiring, J. D., Ford, A. B., O'Meara, J. M., Peeples, M. S., Sembach, K. R., & Weinberg, D. H. 2013, ApJ, 777, 59

Tumlinson, J., Thom, C., Werk, J. K., Prochaska, J. X., Tripp, T. M., Weinberg, D. H., Peeples, M. S., O'Meara, J. M., Oppenheimer, B. D., Meiring, J. D., Katz, N. S., Davé, R., Ford, A. B., & Sembach, K. R. 2011, Science, 334, 948

Tuttle, S. E., Schiminovich, D., Grange, R., Rahman, S., Matuszewski, M., Milliard, B., Deharveng, J.-M., & Martin, D. C. 2010, in Society of Photo-Optical Instrumentation Engineers (SPIE) Conference Series, Vol. 7732, Society of Photo-Optical Instrumentation Engineers (SPIE) Conference Series

Tuttle, S. E., Schiminovich, D., Milliard, B., Grange, R., Martin, D. C., Rahman, S., Deharveng, J., McLean, R., Tajiri, G., & Matuszewski, M. 2008, in Presented at the Society of Photo-Optical Instrumentation Engineers (SPIE) Conference, Vol. 7014, Society of Photo-Optical Instrumentation Engineers (SPIE) Conference Series

van de Voort, F. & Schaye, J. 2013, MNRAS, 430, 2688

van der Kruit, P. C. & Freeman, K. C. 2011, ARA&A, 49, 301

van Driel, W., Combes, F., Casoli, F., Gerin, M., Nakai, N., Miyaji, T., Hamabe, M., Sofue, Y., Ichikawa, T., Yoshida, S., Kobayashi, Y., Geng, F., Minezaki, T., Arimoto, N., Kodama, T., Goudfrooij, P., Mulder, P. S., Wakamatsu, K., & Yanagisawa, K. 1995, AJ, 109, 942

van Leeuwen, F. 2008, VizieR Online Data Catalog, 1311, 0

Voyer, E. N., Gardner, J. P., Teplitz, H. I., Siana, B. D., & de Mello, D. F. 2011, ApJ, 736, 80

Weingartner, J. C. & Draine, B. T. 2001, ApJ, 548, 296

Werk, J. K., Prochaska, J. X., Thom, C., Tumlinson, J., Tripp, T. M., O'Meara, J. M., & Peeples, M. S. 2013, ApJS, 204, 17

Werk, J. K., Putman, M. E., Meurer, G. R., Ryan-Weber, E. V., Kehrig, C., Thilker, D. A., Bland-Hawthorn, J., Drinkwater, M. J., Kennicutt, Jr., R. C., Wong, O. I., Freeman, K. C., Oey, M. S., Dopita, M. A., Doyle, M. T., Ferguson, H. C., Hanish, D. J., Heckman, T. M., Kilborn, V. A., Kim, J. H., Knezek, P. M., Koribalski, B., Meyer, M., Smith, R. C., & Zwaan, M. A. 2010, AJ, 139, 279

White, R. L., Becker, R. H., Fan, X., & Strauss, M. A. 2003, AJ, 126, 1

Witt, A. N., Gold, B., Barnes, III, F. S., DeRoo, C. T., Vijh, U. P., & Madsen, G. J. 2010, ApJ, 724, 1551

Witt, A. N., Mandel, S., Sell, P. H., Dixon, T., & Vijh, U. P. 2008, ApJ, 679, 497

Witt, A. N. & Petersohn, J. K. 1994, in Astronomical Society of the Pacific Conference Series, Vol. 58, The First Symposium on the Infrared Cirrus and Diffuse Interstellar Clouds, ed. R. M. Cutri & W. B. Latter, 91

Woermann, B., Gaylard, M. J., & Otrupcek, R. 2001, MNRAS, 325, 1213

Wood, K. & Reynolds, R. J. 1999, ApJ, 525, 799

Wright, E. L. 1992, ApJ, 391, 34

Xu, C. K., Donas, J., Arnouts, S., Wyder, T. K., Seibert, M., Iglesias-Páramo, J., Blaizot, J., Small, T., Milliard, B., Schiminovich, D., Martin, D. C., Barlow, T. A., Bianchi, L., Byun, Y.-I., Forster, K., Friedman, P. G., Heckman, T. M., Jelinsky, P. N., Lee, Y.-W., Madore, B. F., Malina, R. F., Morrissey, P., Neff, S. G., Rich, R. M., Siegmund, O. H. W., Szalay, A. S., & Welsh, B. Y. 2005, ApJ, 619, L11

Yao, Y., Nowak, M. A., Wang, Q. D., Schulz, N. S., & Canizares, C. R. 2008, ApJ, 672, L21

Zukic, M., Torr, D. G., Spann, J. F., & Torr, M. R. 1990, Appl. Opt., 29, 4284

Appendix A

Optical Constants of HfO_2 and delta-doped Silicon

Table A.1: Optical Constants of Delta Doped Silicon

λ (nm)	n	k	λ (nm)	n	k	λ (nm)	n	k
140.	0.50	1.40	440.	4.32	0.22	740.	3.38	0.03
145.	0.51	1.48	445.	4.27	0.21	745.	3.37	0.03
150.	0.52	1.57	450.	4.22	0.20	750.	3.37	0.03
155.	0.52	1.65	455.	4.18	0.19	755.	3.37	0.03
160.	0.53	1.74	460.	4.14	0.18	760.	3.36	0.03
165.	0.54	1.84	465.	4.10	0.17	765.	3.36	0.03
170.	0.56	1.95	470.	4.07	0.16	770.	3.35	0.03
175.	0.58	2.05	475.	4.04	0.15	775.	3.35	0.03
180.	0.62	2.16	480.	4.01	0.14	780.	3.35	0.03
185.	0.67	2.27	485.	3.98	0.14	785.	3.34	0.03
190.	0.73	2.37	490.	3.95	0.13	790.	3.34	0.03
195.	0.79	2.47	495.	3.92	0.12	795.	3.33	0.03
200.	0.86	2.56	500.	3.90	0.12	800.	3.33	0.03

Continued on next page

Table A.1 – continued from previous page

λ (nm)	n	k	λ (nm)	n	k	λ (nm)	n	k
205.	0.94	2.65	505.	3.87	0.11	805.	3.33	0.03
210.	1.01	2.73	510.	3.85	0.11	810.	3.32	0.03
215.	1.09	2.80	515.	3.83	0.11	815.	3.32	0.03
220.	1.16	2.87	520.	3.81	0.10	820.	3.32	0.03
225.	1.22	2.94	525.	3.79	0.10	825.	3.31	0.03
230.	1.29	3.01	530.	3.77	0.09	830.	3.31	0.03
235.	1.34	3.09	535.	3.75	0.09	835.	3.31	0.03
240.	1.39	3.18	540.	3.74	0.09	840.	3.31	0.03
245.	1.45	3.28	545.	3.72	0.08	845.	3.30	0.03
250.	1.50	3.41	550.	3.70	0.08	850.	3.30	0.03
255.	1.56	3.56	555.	3.69	0.08	855.	3.30	0.03
260.	1.65	3.75	560.	3.67	0.08	860.	3.29	0.03
265.	1.78	3.97	565.	3.66	0.07	865.	3.29	0.03
270.	1.98	4.23	570.	3.65	0.07	870.	3.29	0.02
275.	2.28	4.49	575.	3.63	0.07	875.	3.29	0.02
280.	2.73	4.70	580.	3.62	0.07	880.	3.28	0.02
285.	3.29	4.74	585.	3.61	0.07	885.	3.28	0.02
290.	3.84	4.55	590.	3.60	0.06	890.	3.28	0.02
295.	4.22	4.17	595.	3.59	0.06	895.	3.28	0.02
300.	4.37	3.81	600.	3.58	0.06	900.	3.27	0.02
305.	4.42	3.55	605.	3.57	0.06	905.	3.27	0.02
310.	4.46	3.37	610.	3.56	0.06	910.	3.27	0.02
315.	4.51	3.24	615.	3.55	0.06	915.	3.27	0.02
320.	4.57	3.12	620.	3.54	0.05	920.	3.27	0.02
325.	4.63	3.01	625.	3.53	0.05	925.	3.26	0.02
330.	4.67	2.91	630.	3.52	0.05	930.	3.26	0.02
335.	4.71	2.86	635.	3.51	0.05	935.	3.26	0.02
340.	4.78	2.86	640.	3.50	0.05	940.	3.26	0.02
345.	4.94	2.90	645.	3.49	0.05	945.	3.25	0.02
350.	5.25	2.89	650.	3.49	0.05	950.	3.25	0.02
355.	5.64	2.68	655.	3.48	0.05	955.	3.25	0.02
360.	5.92	2.25	660.	3.47	0.05	960.	3.25	0.02
365.	5.97	1.77	665.	3.47	0.04	965.	3.25	0.02

Continued on next page

Table A.1 – continued from previous page

λ (nm)	n	k	λ (nm)	n	k	λ (nm)	n	k
370.	5.87	1.37	670.	3.46	0.04	970.	3.25	0.02
375.	5.70	1.07	675.	3.45	0.04	975.	3.24	0.02
380.	5.53	0.86	680.	3.44	0.04	980.	3.24	0.02
385.	5.36	0.71	685.	3.44	0.04	985.	3.24	0.02
390.	5.20	0.60	690.	3.43	0.04	990.	3.24	0.02
395.	5.06	0.51	695.	3.43	0.04	995.	3.24	0.02
400.	4.94	0.45	700.	3.42	0.04	1000.	3.24	0.02
405.	4.83	0.40	705.	3.41	0.04			
410.	4.73	0.36	710.	3.41	0.04			
415.	4.65	0.33	715.	3.40	0.04			
420.	4.57	0.30	720.	3.40	0.04			
425.	4.50	0.28	725.	3.39	0.04			
430.	4.43	0.26	730.	3.39	0.03			
435.	4.37	0.24	735.	3.38	0.03			

Table A.2: Optical Constants of Hafnium Oxide

λ (nm)	n	k	λ (nm)	n	k	λ (nm)	n	k
136.	2.01	1.23	203.	2.60	0.18	400.	2.03	0.02
137.	2.04	1.22	205.	2.58	0.16	407.	2.03	0.02
138.	2.06	1.20	207.	2.56	0.15	413.	2.03	0.02
139.	2.07	1.18	208.	2.54	0.13	420.	2.02	0.02
139.	2.08	1.17	210.	2.52	0.12	428.	2.02	0.02
140.	2.09	1.16	212.	2.50	0.11	435.	2.02	0.02
141.	2.09	1.15	214.	2.48	0.10	443.	2.02	0.02
142.	2.10	1.15	216.	2.46	0.09	451.	2.01	0.02
142.	2.11	1.15	218.	2.44	0.08	459.	2.01	0.02
143.	2.12	1.15	220.	2.42	0.07	468.	2.01	0.01
144.	2.13	1.15	221.	2.40	0.07	477.	2.00	0.01
145.	2.14	1.15	223.	2.38	0.06	486.	2.00	0.01
146.	2.15	1.15	226.	2.37	0.06	496.	2.00	0.01

Continued on next page

Table A.2 – continued from previous page

λ (nm)	n	k	λ (nm)	n	k	λ (nm)	n	k
147.	2.17	1.15	228.	2.35	0.05	506.	2.00	0.01
148.	2.19	1.15	230.	2.34	0.05	517.	2.00	0.01
148.	2.20	1.14	232.	2.32	0.05	528.	1.99	0.01
149.	2.22	1.14	234.	2.31	0.04	539.	1.99	0.01
150.	2.23	1.13	236.	2.30	0.04	551.	1.99	0.01
151.	2.25	1.13	238.	2.28	0.04	564.	1.99	0.01
152.	2.26	1.12	241.	2.27	0.04	577.	1.98	0.01
153.	2.28	1.12	243.	2.26	0.04	590.	1.98	0.01
154.	2.29	1.11	246.	2.25	0.04	605.	1.98	0.01
155.	2.31	1.11	248.	2.24	0.04	620.	1.98	0.01
156.	2.33	1.10	250.	2.23	0.04	636.	1.98	0.01
157.	2.34	1.09	253.	2.22	0.04	653.	1.97	0.01
158.	2.36	1.09	256.	2.21	0.04	670.	1.97	0.01
159.	2.38	1.08	258.	2.20	0.03	689.	1.97	0.01
160.	2.40	1.07	261.	2.19	0.03	709.	1.97	0.01
161.	2.42	1.07	264.	2.19	0.03	729.	1.97	0.01
162.	2.44	1.06	267.	2.18	0.03	752.	1.97	0.01
163.	2.46	1.05	270.	2.17	0.03	775.	1.97	0.01
164.	2.48	1.04	272.	2.16	0.03	800.	1.96	0.01
165.	2.50	1.02	276.	2.16	0.03	827.	1.96	0.01
166.	2.53	1.01	279.	2.15	0.03	855.	1.96	0.01
168.	2.55	0.99	282.	2.14	0.03	886.	1.96	0.01
169.	2.58	0.98	285.	2.14	0.03	918.	1.96	0.01
170.	2.60	0.96	288.	2.13	0.03	954.	1.96	0.00
171.	2.62	0.93	292.	2.13	0.03	992.	1.96	0.00
172.	2.65	0.91	295.	2.12	0.03	1033.	1.95	0.00
173.	2.67	0.88	299.	2.12	0.03	1078.	1.95	0.00
175.	2.69	0.85	302.	2.11	0.03	1127.	1.95	0.00
176.	2.71	0.82	306.	2.10	0.03	1181.	1.95	0.00
177.	2.72	0.79	310.	2.10	0.03	1240.	1.95	0.00
178.	2.74	0.75	314.	2.10	0.03	1305.	1.95	0.00
180.	2.75	0.71	318.	2.09	0.03	1378.	1.95	0.00
181.	2.76	0.68	322.	2.09	0.03	1459.	1.95	0.00

Continued on next page

Table A.2 – continued from previous page

λ (nm)	n	k	λ (nm)	n	k	λ (nm)	n	k
182.	2.77	0.64	326.	2.08	0.03	1550.	1.95	0.00
184.	2.77	0.60	331.	2.08	0.03	1653.	1.95	0.00
185.	2.77	0.56	335.	2.07	0.03	1771.	1.95	0.00
186.	2.77	0.52	340.	2.07	0.03	1908.	1.94	0.00
188.	2.76	0.48	344.	2.07	0.03	2067.	1.94	0.00
189.	2.76	0.45	349.	2.06	0.03	2254.	1.94	0.00
191.	2.75	0.41	354.	2.06	0.02	2480.	1.94	0.00
192.	2.73	0.37	359.	2.06	0.02			
194.	2.72	0.34	365.	2.05	0.02			
195.	2.70	0.31	370.	2.05	0.02			
197.	2.69	0.28	376.	2.04	0.02			
198.	2.67	0.25	382.	2.04	0.02			
200.	2.65	0.23	388.	2.04	0.02			
202.	2.63	0.20	394.	2.04	0.02			
203.	2.60	0.18	400.	2.03	0.02			

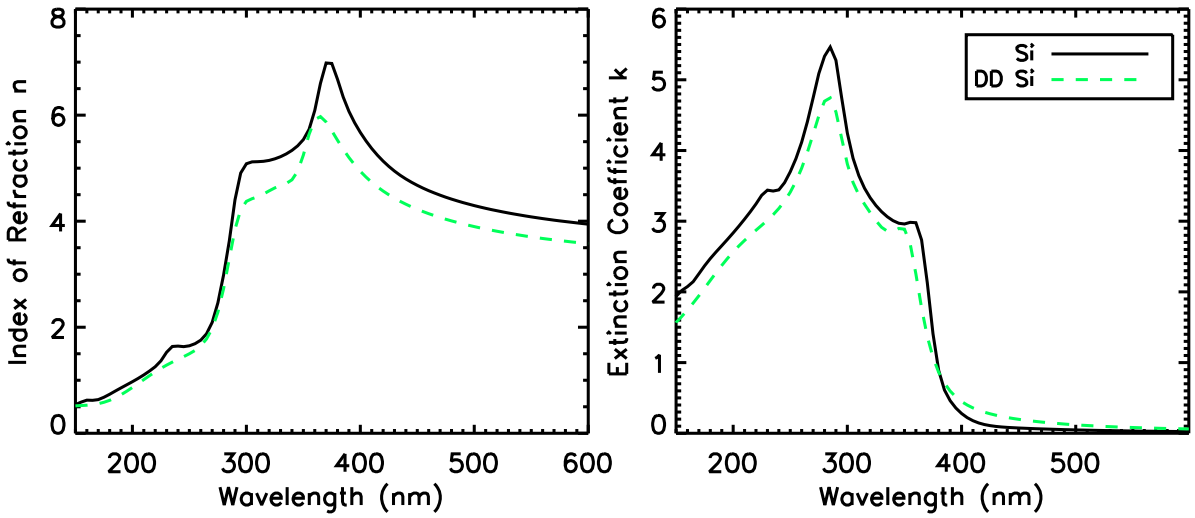

Figure A.1 Delta doped silicon optical constants

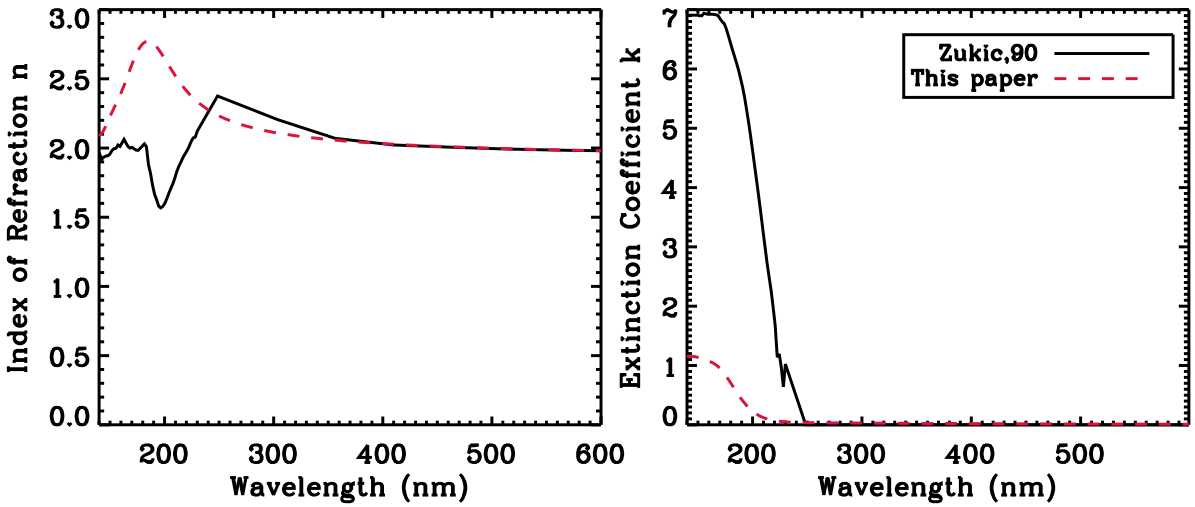

Figure A.2 Hafnium Oxide optical constants